AD-A171 169 COMPUTATIONAL FLUID DYNAMIC STUDIES OF CERTAIN DUCTED BLUFF-BODY FLOWFIEL (U) DAYTON UNIV OH RESEARCH INST M S RAJU ET AL JUL 86 UDR-TR-5-83-VOL-2 1/2

UNCLASSIFIED AFWAL-TR-86-2004-VOL-2 F33615-84-C-2411 F/G 21/2 NL

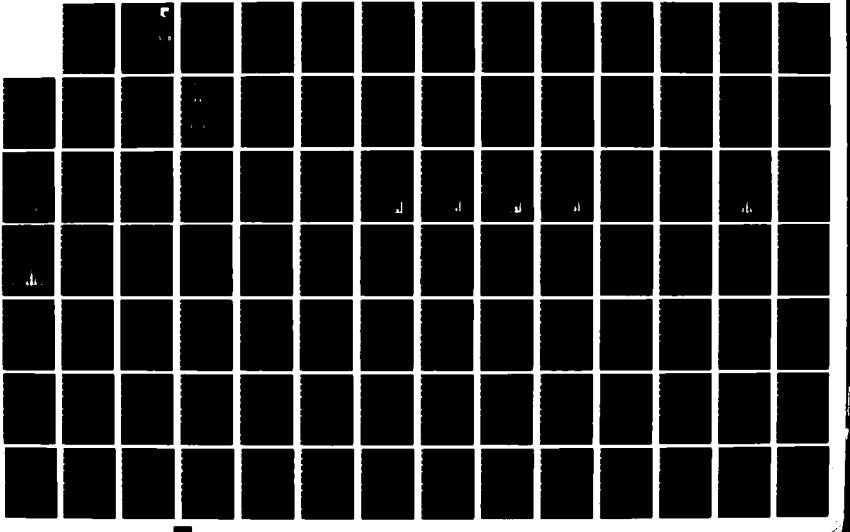

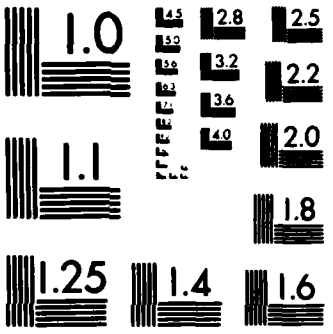

'CROCOPY RESOLUTION TEST CHART
NATIONAL BUREAU OF STANDARDS-1963-A

AD-A171 169

AFWAL-TR-86-2004
Volume II

COMPUTATIONAL FLUID DYNAMIC STUDIES OF CERTAIN DUCTED BLUFF-BODY FLOWFIELDS RELEVANT TO TURBOJET COMBUSTORS

VOLUME II - Time-Averaged Flowfield Predictions for a Proposed Centerbody Combustor

M. S. Raju and L. Krishnamurthy
University of Dayton
Research Institute
Dayton, Ohio 45469-0001

DTIC
ELECTE
AUG 26 1986
S D
D

July 1986

FINAL REPORT FOR PERIOD 16 AUGUST 1984 - 30 SEPTEMBER 1985

DTIC FILE COPY

Approved for Public Release, Distribution Unlimited

AERO PROPULSION LABORATORY
AIR FORCE WRIGHT AERONAUTICAL LABORATORIES
AIR FORCE SYSTEMS COMMAND
WRIGHT-PATTERSON AIR FORCE BASE, OH 45433-6563

86 8 25 031

NOTICE

"When Government drawings, specifications, or other data are used for any purpose other than in connection with a definitely related government procurement operation, the United States Government thereby incurs no responsibility nor any obligation whatsoever; and the fact that the Government may have formulated, furnished, or in any other way supplied the said drawings, specifications, or other data, is not to be regarded by implication or otherwise as in any manner licensing the holder or any other person or corporation, or conveying any rights or permission to manufacture, use or sell any patented invention that may in any way be related thereto."

This report has been reviewed by the Office of Public Affairs (ASD/PA) and is releasable to the National Technical Information Service (NTIS). At NTIS, it will be available to the general public, including foreign nations.

This technical report has been reviewed and is approved for publication.

W.M. Roquemore

W.M. ROQUEMORE
Fuels Branch
Fuels and Lubrication Division
Aero Propulsion Laboratory

Arthur V. Churchill

ARTHUR V. CHURCHILL,
Chief, Fuels Branch
Fuels and Lubrication Division
Aero Propulsion Laboratory

FOR THE COMMANDER

Robert D. Sherrill

ROBERT D. SHERRILL, Chief
Fuels and Lubrication Division
Aero Propulsion Laboratory

"If your address has changed, if you wish to be removed from our mailing list, or if the addressee is no longer employed by your organization, please notify AFWAL/POSF, W-PAFB, OH 45433-6563 to help us maintain a current mailing list.

Copies of this report should not be returned unless return is required by security considerations, contractual obligations, or notice of a specific document.

REPORT DOCUMENTATION PAGE

1a. REPORT SECURITY CLASSIFICATION Unclassified	1b. RESTRICTIVE MARKINGS N/A
2a. SECURITY CLASSIFICATION AUTHORITY N/A	3. DISTRIBUTION/AVAILABILITY OF REPORT Approved for Public Release, Distribution Unlimited
2b. DECLASSIFICATION/DOWNGRADING SCHEDULE N/A	
4. PERFORMING ORGANIZATION REPORT NUMBER(S) UDR-TR-85-83	5. MONITORING ORGANIZATION REPORT NUMBER(S) AFWAL-TR-86-2004, Volume II
6a. NAME OF PERFORMING ORGANIZATION University of Dayton Research Institute 6b. OFFICE SYMBOL (If applicable)	7a. NAME OF MONITORING ORGANIZATION Aero Propulsion Laboratory (AFSC) Air Force Wright Aeronautical Laboratory
6c. ADDRESS (City, State and ZIP Code) Dayton, OH 45469-0001	7b. ADDRESS (City, State and ZIP Code) AFWAL/POSF Wright-Patterson Air Force Base, OH 45433-6563
8a. NAME OF FUNDING/SPONSORING ORGANIZATION 8b. OFFICE SYMBOL (If applicable) AFWAL/POSF	9. PROCUREMENT INSTRUMENT IDENTIFICATION NUMBER F33615-84-C-2411, Task 02
8c. ADDRESS (City, State and ZIP Code)	10. SOURCE OF FUNDING NOS. PROGRAM ELEMENT NO. 62203F; PROJECT NO. 3048; TASK NO. 05; WORK UNIT NO. 43
11. TITLE (Include Security Classification) (See Reverse Side)	
12. PERSONAL AUTHOR(S) M. S. Raju and L. Krishnamurthy	
13a. TYPE OF REPORT Final Report	13b. TIME COVERED FROM 8/16/84 TO 9/30/85
14. DATE OF REPORT (Yr., Mo., Day) July 1986	15. PAGE COUNT 125
16. SUPPLEMENTARY NOTATION Work performed under the Scholarly Research Program (was investigated)	

17. COSATI CODES		
FIELD	GROUP	SUB. GR.
2102	2104	2105

18. SUBJECT TERMS (Continue on reverse if necessary and identify by block number)
Bluff-Body Near Wake
Confined Turbulent Flows
Nonreacting Flows
Reacting Flows
(See Reverse Side)

19. ABSTRACT (Continue on reverse if necessary and identify by block number)

A numerical investigation of the near-wake region in a ducted bluff-body combustor by finite-difference computations is reported. The numerical predictions are based upon the time-independent, Reynolds-averaged Navier-Stokes equations and the k-ε turbulence model. The steady-state calculations address both nonreacting and reacting flowfields in a novel configuration which is under development by the Air Force to more realistically simulate some of the essential features of the primary zone of a gas turbine combustion chamber. This configuration is characterized by turbulent mixing and combustion in the recirculating near-wake region downstream of an axisymmetric bluff body due to two annular air streams--an outer swirl-free flow and an inner swirling flow and a central fuel jet. The latter contains propane for reacting flows and carbon dioxide for nonreacting flows. (See Reverse Side)

20. DISTRIBUTION/AVAILABILITY OF ABSTRACT UNCLASSIFIED/UNLIMITED ☒ SAME AS RPT. ☐ DTIC USERS ☐	21. ABSTRACT SECURITY CLASSIFICATION Unclassified
22a. NAME OF RESPONSIBLE INDIVIDUAL W. M. Roquemore	22b. TELEPHONE NUMBER (Include Area Code) (513) 255-6813 22c. OFFICE SYMBOL AFWAL/POSF

BLOCK 11 (Continued)

Computational Fluid Dynamic Studies of Certain Ducted Bluff-Body Flowfields Relevant to Turbojet Combustors (U)

Volume II
Time-Averaged Flowfield Predictions for a Proposed Centerbody Combustor

BLOCK 18 (Continued)

Recirculating Flows
Swirling Flows

BLOCK 19 (Continued)

In view of the large number of geometrical and flow parameters involved here, the reported results are concerned with only a limited parametric examination with the major emphasis being on nonreacting flows. The questions addressed for a particular set of geometric parameters include the effects of variation of mass flow rates in all three streams and the influence of swirl in the middle stream. The reacting computations investigate the influence of swirl on combustion, as well as that of combustion on the flowfield. A careful consideration of the computed results of selected flow variables in terms of the global flowfield features, axial variations along the axis of symmetry, and radial profiles at different axial stations examines the implications of the present predictions and thereby provides possible directions for ascertaining the validity of these predictions through experimental diagnostic measurements in the future.

The computational fluid dynamic examination of the steady-state calculations in this report and of the time-dependent calculations in Volume I has provided a limited assessment of the numerical predictions of gas turbine combustor-like flowfields and suggests directions for future predictive and experimental research in the proposed Air Force research combustor configuration.

PREFACE

This final report was submitted by the University of Dayton, under Contract No. F33615-84-C-2411, Task 02. The research task, entitled "Assessment of Time-Dependent Calculations for Gas Turbine Combustor-Type Flows," was sponsored by the Scholarly Research Program of the Air Force Wright Aeronautical Laboratories, Aero Propulsion Laboratory, Wright-Patterson Air Force Base, Ohio, under Project No. 3048, Task 05, Work Unit 43. Dr. William M. Roquemore, AFWAL/POSF, was Project Engineer. The research work dealing with the time-dependent calculations reported in Volume I was initiated in August 1984 and completed in February 1985. The work describing the time-averaged calculations reported in Volume II was initiated, under an Extension of Task 02, in April 1985 and completed in August 1985. The numerical calculations were performed by Dr. M. S. Raju, Associate Research Engineer, and the report was written by Dr. L. Krishnamurthy, Senior Research Engineer. The authors express their appreciation to Dr. Roquemore for his interest and to Mr. J. S. Stutrud, AFWAL/POSF, for his help with their MODCOMP computer in the time-averaged calculations. The time-dependent computations were carried out on the CRAY-1S computer at the NASA Lewis Research Center and the authors express their appreciation to Dr. E. J. Mularz and Mr. R. W. Claus for their support of this computing activity. The authors also acknowledge the assistance of Ms. Ellen Bordewisch, Ms. Maria Carroll, Ms. Teresa Harding, and Ms. Marlene Haas, UDRI, in preparing this report, and Ms. Anita Cochran, UDRI in technical editing thereof.

Accesion For
NTIS CRA&I
DTIC TAB
Unannounced
Justification
By
Distribution /
Availability Codes
Dist | Avail and / or Special
A-1

TABLE OF CONTENTS

SECTION		PAGE NO.
I.	INTRODUCTION	1
	1. Background	1
	2. Scope of Present Work	3
	3. Outline of Report	4
II.	NUMERICAL COMPUTATIONS	5
	1. POSF Configuration	5
	2. Governing Equations	5
	3. Boundary Conditions	10
	4. Computational Details	14
	a. Swirl Characteristics	14
	b. Computational Domain	16
	c. Computational Parameters and Test Cases	16
III.	RESULTS AND DISCUSSION	21
	1. Nonreacting Flowfields	21
	a. Velocity-Vector Plots	21
	(1) Variations in Swirling and Central Streams	22
	(2) Variations in Swirl and Outer Annular Stream	28
	b. Centerline Variations	32
	(1) Axial Velocity Fields	33
	(2) Temperature and Concentration Fields	43
	(3) Implications of Present Predictions	52
	(a) Aspects of Conformity	53
	(b) Area of Disagreement	55
	(c) Rationale	56
	(4) Swirl Velocity Fields	58
	c. Radial Distributions	66
	(1) Profiles of Turbulent Kinetic Energy	66
	(2) Temperature Profiles	76
	(3) Profiles of CO_2 Mass Fraction and Swirl Velocity	76
	2. Reacting Flowfields	92
	a. Shortcomings of Computational Procedure	92
	b. Swirl-Free Flowfield	93
	(1) Overview of Flowfield Structure	93
	(2) Centerline Variations	98
	(3) Radial Profiles	101

TABLE OF CONTENTS
(Concluded)

SECTION		PAGE NO.
	c. Flowfield with Swirl	104
	(1) Overall Flowfield Features	104
	(2) Centerline Variations	108
	(3) Radial Profiles	114
IV.	CONCLUSIONS AND RECOMMENDATIONS	120
	1. Conclusions	120
	2. Recommendations	122
	REFERENCES	124

LIST OF ILLUSTRATIONS

FIGURE	TITLE	PAGE NO.
1.	Schematic of the Proposed Combustor.	6
2.	Finite-Difference Computational Grid.	17
3(a)-(d).	Velocity-Vector Plots.	23-26
4a.	Velocity-Vector Plots (Top: Case 6, Bottom: Case 5).	29
4b.	Velocity-Vector Plots (Top: Case 8, Bottom: Case 7).	31
5(a)-(h).	Centerline Profiles of Mean and rms Axial Velocity Components.	34-41
6(a)-(h).	Centerline Profiles of CO_2 Mass Fraction and Temperature.	44-51
7(a)-(f).	Variation of Mean Swirl Velocity.	59-64
8(a)-(h).	Radial Profiles of Turbulent Kinetic Energy.	67-74
9(a)-(h).	Radial Profiles of Temperature.	77-84
10(a)-(f).	Radial Profiles of CO_2 Mass Fraction and Swirl Velocity.	85-90
11a.	Velocity-Vector Plot for Swirl-Free Reacting Flow.	94
11b.	Temperature Contours for Swirl-Free Reacting Flow.	95
11c.	Density Contours for Swirl-Free Reacting Flow.	96
12a.	Centerline Profiles of Mean and rms Axial Velocity Components.	99
12b.	Centerline Profiles of Propane Mass Fraction and Temperature.	100
13a.	Radial Profiles of Turbulent Kinetic Energy.	102

LIST OF ILLUSTRATIONS
(Concluded)

FIGURE	TITLE	PAGE NO.
13b.	Radial Profiles of Temperature.	103
14a.	Velocity-Vector Plot for Reacting Flow with Swirl.	105
14b.	Temperature Contours for Reacting Flow with Swirl.	106
14c.	Density Contours for Reacting Flow with Swirl.	107
15a.	Centerline Profiles of Mean and rms Axial Velocity Components.	109
15b.	Centerline Profiles of Propane Mass Fraction and Temperature.	110
15c.	Variation of Mean Swirl Velocity.	111
16a.	Radial Profiles of Turbulent Kinetic Energy.	115
16b.	Radial Profiles of Temperature.	116
16c.	Radial Profiles of Propane Mass Fraction and Swirl Velocity	117

LIST OF TABLES

TABLE	TITLE	PAGE NO.
1.	Governing Equations.	8
2.	Boundary Conditions.	12
3.	Inlet Flow Conditions for Different Cases Examined.	19
4.	Swirl Numbers and Flux Ratios for Different Cases Run.	20

SECTION I
INTRODUCTION

This final report (in two volumes) documents the results of the computational fluid dynamic (CFD) research performed by the University of Dayton for the Air Force Wright Aeronautical Laboratories, Aero Propulsion Laboratory (AFWAL/PO). The focus of this CFD research is the confined, turbulent recirculating flowfield behind a bluff body in the AFWAL/POSF research combustor.

In an existing version of the POSF combustor, a centerbody configuration, involving the turbulent mixing and combustion of an annular air stream and a central fuel jet in the near wake region of an axisymmetric bluff body, has been the subject of extensive diagnostic and predictive research. The results of computations of this configuration for the nonreacting flow due to the annular air alone, obtained with the time-dependent Navier-Stokes equations incorporating a realistic turbulence model, are presented in Volume I of this report. The time-averaged predictions based upon a solution of the Reynolds-averaged Navier-Stokes equations for a proposed POSF combustor configuration, involving two annular air streams--a swirl-free outer stream and a swirling inner stream, a central fuel jet, and a centerbody imbedding the swirler and the fuel nozzle, are reported here, in Volume II.

1. BACKGROUND

Research in gas turbine combustor-type flows is motivated by the continuing interest in enhancing our understanding of the turbulent mixing and combustion processes in turbojet-combustion chambers. Thus, the POSF research combustor (Reference 1) has been the focus of extensive, ongoing, experimental diagnostic and computational fluid dynamic research activities. These activities

have been directed at a ducted bluff-body configuration involving the turbulent flow and combustion of an annular air stream and a central fuel jet. Of particular interest to an assessment of time-dependent calculations for combustor-type flows is the CFD research completed at the University of Dayton Research Institute (UDRI) which addressed the solution of time-averaged and time-dependent Navier-Stokes equations for the nonreacting flowfields in the POSF centerbody combustor (References 2-3). A further continuation of such an assessment encompassing time-dependent, turbulent flow computations for the existing centerbody configuration formed part of the present Scholarly Research program. The results of this CFD research are documented in Volume I of this report.

The experimental diagnostic and computational predictive research of the recent past on the existing centerbody configuration has given rise to several fundamental and practical implications of relevance to flowfields in gas-turbine combustors. A practical consequence of these implications is an interesting POSF configuration under consideration for extensive development and testing. The new POSF configuration is expected to simulate more closely some of the essential flowfield features of the primary zone of a gas-turbine combustor than did the previous centerbody configuration.

Although the proposed POSF combustor continues to represent a ducted bluff-body configuration, it is distinguished from its predecessor in several respects. A particularly salient feature is the presence of a swirler imbedded in the bluff-body flame holder (which also carries the central fuel nozzle as before). This gives rise to the turbulent mixing of two annular air streams--a swirl-free outer stream and a swirling inner stream. The introduction of swirl and two outer streams in a configuration already characterized by the confining outer duct, bluff-body recirculating near wake, and central fuel jet renders the new combustor extremely complex. Nevertheless, it imparts certain realism to the POSF research combustor.

Accordingly, a CFD examination of the proposed configuration was considered worthwhile as part of the present assessment studies. Indeed, such an investigation conducted prior to and during the POSF development program could provide some guidelines in the selection of optimum conditions for further development. Furthermore, testing of CFD methods against a flowfield that did not exist and had not been measured before makes it possible to ascertain (when new measurements become available for comparison) whether these methods could really serve as predictions rather than mere "postdictions" or correlations.

2. SCOPE OF PRESENT WORK

As part of an assessment of time-dependent calculations for gas turbine combustor-type flows, a proper CFD examination of the proposed POSF combustor must entail both unsteady and steady-state flow computations. However, within the limited scope of the present research program and in view of the inadequate capability of the time-dependent formulation (e.g., see Volume I) to address the full complexity of the new configuration, only steady-state calculations were carried out. Such an approach is of interest nonetheless for this configuration, since the numerical solution of time-averaged equations appears to provide reasonable predictions of the overall trends in gas turbine combustor-type flows and represents an accepted design tool in the industry (Reference 4). Moreover, this afforded the means for a computational assessment of a recent time-averaged calculation procedure made available to UDRI by the Air Force. A newer version of the TEACH procedure which seeks to solve the Reynolds-averaged Navier-Stokes equations, this computer program (Reference 5) was not expected to involve major program development effort. Also, this version appeared to possess some physical and numerical modeling refinements which could lead to improved flowfield predictions in comparison to the earlier results (e.g., see References 2 and 3).

Thus, the present CFD research involves the modification and adaptation of the time-averaged formulation of Reference 5 for the analysis of subsonic, swirling, and reacting turbulent flowfields of the proposed POSF research combustor. The plethora of geometric and fluid dynamic parameters characterizing this complex configuration has necessitated a somewhat limited parametric investigation. As will be seen subsequently, selected test cases were considered with an intent to emphasize the role of the inner annular stream (with or without swirl) in the turbulent mixing and combustion characteristics of the POSF configuration.

3. OUTLINE OF REPORT

The governing equations and the boundary conditions are discussed briefly in Section II. That section also highlights the computational case studies and the parametric values thereof. The results of the CFD investigation are presented and discussed in Section III, where some of the deficiencies of the calculation procedure noted in the present investigation are also indicated. Section IV outlines the conclusions from the present study and offers our recommendations for future research.

SECTION II
NUMERICAL COMPUTATIONS

This section deals with the numerical modeling of nonreacting and reacting turbulent flowfields in the proposed POSF combustor through the framework of Reynolds-averaged Navier-Stokes equations. Following is a brief discussion of the theoretical and computational aspects of the solution procedure. Further details are available in Reference 5.

1. POSF CONFIGURATION

The flowfield of interest to the present CFD research is the axisymmetric combustor, a schematic of which is seen in Figure 1. This combustor is under development at AFWAL/POSF as a research tool for gas-turbine combustor modeling and diagnostic instrumentation development. In contrast with the centerbody combustor configuration of earlier studies (References 1-3), the configuration of Figure 1 involves an additional swirling inner air stream which is bounded between the nonswirling outer air stream and the central fuel jet. With the introduction of swirling stream, this configuration more closely resembles some essential aspects of gas-turbine combustor flowfields. The present study is directed at an evaluation of the influence of the swirling stream on the turbulent mixing and combustion characteristics of the bluff-body near-wake region.

2. GOVERNING EQUATIONS

The domain of the present CFD investigation is the open-ended, cylindrical chamber downstream of the base of the bluff body. Because of the recirculating nature of the flow in the immediate vicinity of the bluff body, the mathematical formulation of the steady-state, Reynolds-averaged Navier-Stokes equations entails a fully elliptic system of equations. For the axisymmetric configuration of interest here, the governing

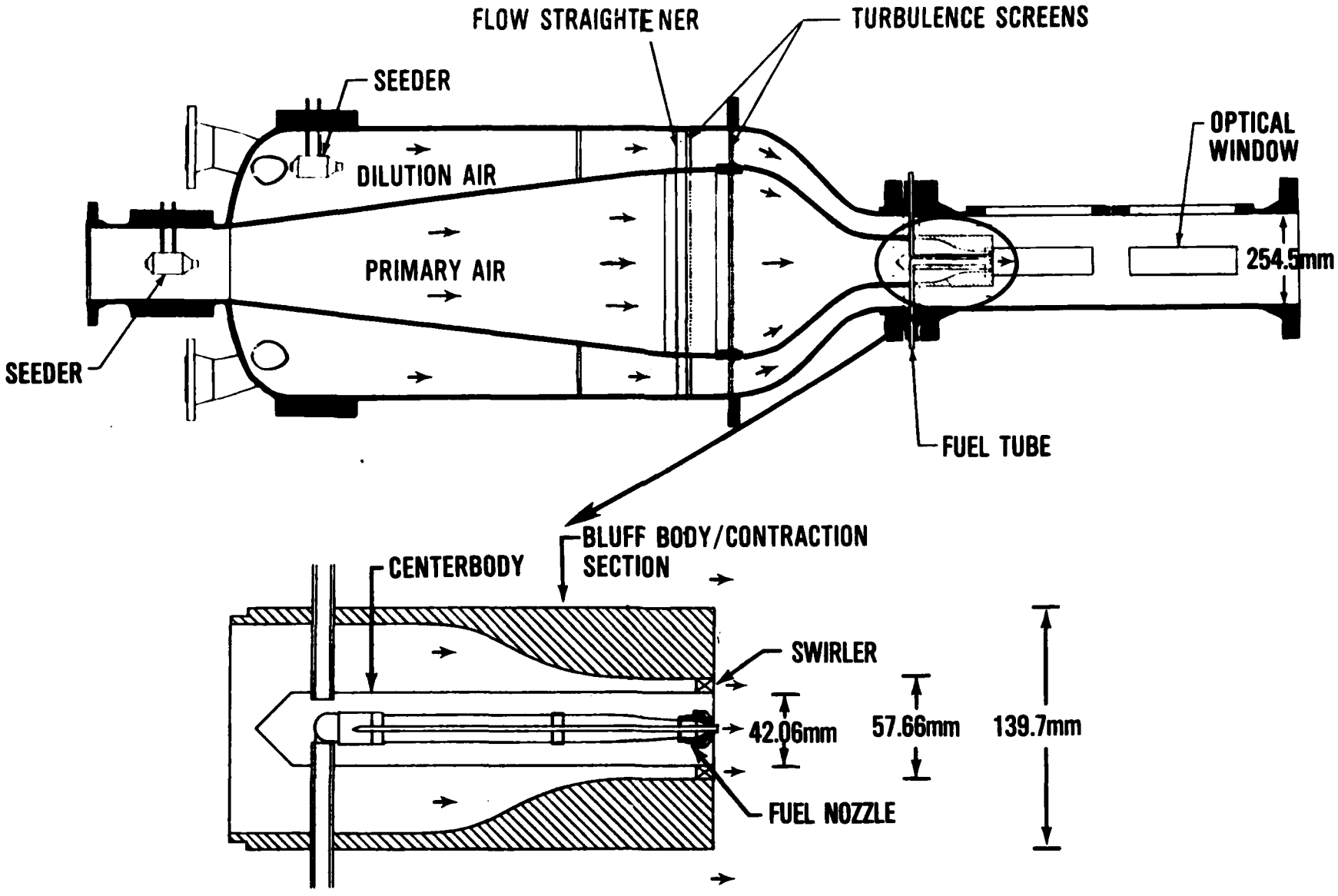

Figure 1. Schematic of the Proposed Combustor.

equations are written in the cylindrical polar coordinates in the following general form for all the dependent variables:

$$\frac{1}{r}\left[\frac{\partial}{\partial x}(\rho r U\phi) + \frac{\partial}{\partial r}(\rho r V\phi) - \frac{\partial}{\partial x}(r\Gamma_\phi \frac{\partial \phi}{\partial x}) - \frac{\partial}{\partial r}(r\Gamma_\phi \frac{\partial \phi}{\partial r})\right] = S_\phi \quad .(1)$$

Here, ϕ denotes the time-mean value of any dependent variable. U, V, and W are the respective time-mean velocity components in the axial (x), radial (r), and azimuthal (θ) directions. Because of the assumption of axisymmetry (in the mean), Equation (1) exhibits no explicit dependence on θ for all the flow variables ϕ (even for the case of nonzero swirl velocity W). ρ is the density, Γ_ϕ the effective exchange coefficient for the transport of the variable ϕ, and S_ϕ the source term for ϕ. The latter includes true source terms (such as those arising from chemical reactions), as well as the terms not covered by the four convective and diffusive terms inside the square brackets of Equation (1). The dependent variable ϕ denotes U, V, W, the turbulent kinetic energy k, its dissipation rate ϵ, fuel mass fraction m_f, mixture fraction f, and enthalpy h. Table 1 shows all the relevant information for these dependent variables. σ_ϕ in Table 1 denotes the appropriate value of the effective Prandtl/Schmidt number for each ϕ.

Turbulence closure is obtained from the two-equation model of Launder and Spalding (Reference 6) for prescribing the eddy viscosity μ_t from the two scalars k and ϵ (See Table 1). In the computer code of Reference 5 the equations for m_f and f describe the combustion of gaseous propane with air. The mixture fraction is defined by the sum of the unburned and burned propane as

$$f = m_f + (1/3)\, m_{CO_2}, \qquad (2)$$

TABLE 1
GOVERNING EQUATIONS

Equation	ϕ	Γ_ϕ	σ_{ϕ_ℓ}	σ_{ϕ_t}	S_ϕ
Continuity	1	0	-	-	0
Axial Momentum	U	μ_{eff}	-	-	$-\frac{\partial p}{\partial x}+\frac{\partial}{\partial x}\left(\mu_{eff}\frac{\partial U}{\partial x}\right)+\frac{1}{r}\frac{\partial}{\partial r}\left(r\mu_{eff}\frac{\partial V}{\partial x}\right)$
Radial Momentum	V	μ_{eff}	-	-	S_V
Tangential Momentum	W	μ_{eff}	-	-	$-\frac{2}{r}\frac{\partial}{\partial r}\left(r\mu_{eff}\right)$
Turbulent Kinetic Energy	k	Γ_{eff}	0.7	1.0	$\mu_t G - C_\mu \rho^2 k^2/\mu_t$
Turbulence Energy Dissipation	ϵ	Γ_{eff}	0.7	$\frac{\kappa^2}{((C_2-C_1)C_\mu^{0.5})}$	$C_1 G C_\mu \rho k - C_2 \rho \epsilon^2/k$
Fuel Mass Fraction	m_f	Γ_{eff}	0.7	0.5	$-\rho\frac{\epsilon}{k}\min\left[Am_f, Am_{O_2}/i, ABm_{pr}/(i+1)\right]$
Mixture Fraction	f	Γ_{eff}	0.7	0.5	0
Enthalpy	h	Γ_{eff}	0.7	0.5	0

C_1	C_2	C_μ	κ	A	B	i
1.44	1.92	0.09	0.4187	4	0.5	3.635

$$S_V = -\frac{\partial p}{\partial r}+\frac{\partial}{\partial x}\left(\mu_{eff}\frac{\partial U}{\partial x}\right)+\frac{1}{r}\frac{\partial}{\partial r}\left(r\mu_{eff}\frac{\partial V}{\partial r}\right)-2\mu_{eff}\frac{V}{r^2}-\frac{2}{3}\frac{\partial}{\partial r}\left[\rho k+\mu_{eff}\left(\frac{\partial U}{\partial x}+\frac{\partial V}{\partial r}\right)\right]+\frac{\rho W^2}{r}$$

$$\mu_{eff}=\mu_\ell+\mu_t,\ \Gamma_{eff}=\frac{\mu_\ell}{\sigma_{\phi_\ell}}+\frac{\mu_t}{\sigma_{\phi_t}},\ \mu_t=C_\mu\rho\frac{k^2}{\epsilon},\ G=2\left[\left(\frac{\partial U}{\partial x}\right)^2+\left(\frac{\partial V}{\partial r}\right)^2+\left(\frac{V}{r}\right)^2\right]+\left(\frac{\partial U}{\partial x}+\frac{\partial V}{\partial r}\right)^2$$

where the replacement of the mass fraction of burned propane by one-third of the mass fraction of CO_2 follows from the stoichiometric combustion reaction of propane and oxygen and the assumption of equal molecular weights for propane and carbon dioxide. The enthalpy is defined by

$$h = m_f H_R + c_{p,m} T, \tag{3}$$

where H_R is the heat of reaction, T the temperature, and $c_{p,m}$ the mean specific heat of mixture. The latter is obtained from

$$c_{p,m} = \sum_j m_j c_{p,j}, \tag{4}$$

with the summation being over all species. The specific heats $c_{p,j}$ of the individual species are obtained from polynomial fits of the form

$$c_{p,j} = (C_{1j} + C_{2j} T + C_{3j} T^2 + C_{4j} T^3 + C_{5j} T^4) R/M_j, \tag{5}$$

where R is the universal gas constant, M_j is the molecular weights of species, and the polynomial constants C_{1j} through C_{5j} can be obtained from standard thermochemical tables (see Reference 5 for the tabulated values for the species C_3H_8, O_2, N_2, H_2O and CO_2).

The source terms S_ϕ for all ϕ are seen in Table 1. The source terms S_u and S_v contain respectively the axial and radial gradients of time-mean pressure p which is one remaining unknown variable. The evaluation of p requires a special procedure in the solution scheme which is discussed in Paragraph II.4. The source terms S_k and S_ϵ correspond to the standard k-ε model and do not include the additional contributions from the large streamline curvature and the preferential influence of normal stresses (which were incorporated in References 2-3 previously).

The source term S_{mf} for fuel mass fraction is obtained from the Magnussen-Hjertager combustion model (Reference 7). This model relates the rate of combustion of the fuel to the rate of dissipation of turbulent eddies. The source terms S_f and S_h for mixture fraction and enthalpy vanish identically (because of their definitions).

Finally in Table 1, the subscripts ℓ and t in μ and σ_ϕ denote the laminar and turbulent counterparts respectively. Table 1 also lists the constants appearing in the turbulence model, as well as the term G representing the rate of production of turbulent kinetic energy by the mean motion. Also, note that once m_f and f are determined by the solution of the corresponding transport equations (for $\phi = m_f$ and f) in Equation (1), the mass fractions of other species like O_2, N_2, CO_2 and H_2O can be easily obtained from the algebraic relationships available in Reference 5.

3. BOUNDARY CONDITIONS

The solution of Equation (1) requires the specification of appropriate boundary conditions for each of the dependent variables. Since the governing formulation is elliptic, the boundary conditions are prescribed on all the boundaries of the computational domain. With symmetry, only the top half of the combustor configuration of Figure 1 needs to be represented by the computational domain. Thus, the top boundary is the duct wall and the bottom boundary is the axis of symmetry. The left boundary denotes the inflow boundary and consists of the outer annular air inlet, bluff-body face, the inner annular (swirling) air inlet, bluff-body face, and the central fuel inlet. The right boundary is the outflow boundary, the location of which is unknown a priori. Its specification is arbitrary and it is essential to ensure that the sensitivity of the computed solutions to the specification of this boundary location is not significant.

The boundary conditions employed in the present CFD investigation are shown in Table 2. Except for the additional azimuthal velocity component W, the present boundary conditions are identical to those used in our previous study (Reference 2). Before proceeding further, some general observations concerning the conditions in Table 2 can be made. Along the bottom boundary, $\partial\phi/\partial r = 0$ for all ϕ and $v = 0$ due to the symmetry requirement. Along the top boundary and bluff-body face (both representing a rigid impermeable wall), the normal velocity components and the normal gradients vanish, the tangential velocity components employ the law of the wall, and the wall-function formulations also apply to k and ϵ. Thus, along duct wall V and $\partial m_i/\partial r$ vanish and U, W, k, and ϵ utilize wall functions. Along the centerbody face U and $\partial m_i/\partial x$ vanish and V, W, K, and ϵ utilize wall functions. At the outflow boundary, consideration of overall mass conservation governs U, while $\partial\phi/\partial x = 0$ for all other variables. This condition for the vanishing axial derivatives at the exit boundary is invariably used in time-averaged computations of subsonic internal flows (e.g., see References 2-4). It is strictly valid only for fully developed turbulent flows and its application to a location where the flow is unlikely to be fully developed has always been a source of concern to the practitioners in CFD. The unfavorable impact of this application on the interior flowfield development remains to be addressed. For a discussion concerning this and other exit-boundary conditions for the time-dependent formulation, see Reference 3.

At the three inlets, all the variables are specified. Thus, the specification of U_{in} follows from the desired mass flow, provided the radial velocity V is zero. Note that V is typically close to zero for well-designed inlets. The swirl velocity is given by

$$W_{in} = S_R \, U_{in}, \tag{6}$$

TABLE 2
BOUNDARY CONDITIONS

ϕ	TOP BOUNDARY (Duct Wall)	BOTTOM BOUNDARY (Axis of symmetry)	LEFT BOUNDARY		RIGHT BOUNDARY (Outflow)
			INLETS	CENTERBODY FACE	
U	Law of the Wall to Relate the Wall Shear Stress τ_w	$\frac{\partial U}{\partial r} = 0$	U specified $= U_{in}$	U = 0	Overall Mass Conservation
V	V = 0	V = 0	V = 0	Law of the Wall to Relate the Wall Shear Stress τ_w	$\frac{\partial V}{\partial x} = 0$
W	Law of the Wall to Relate the Wall Shear Stress τ_w	$\frac{\partial W}{\partial r} = 0$	W specified $= S_R U_{in}$	Law of the Wall to Relate the Wall Shear Stress τ_w	$\frac{\partial W}{\partial r} = 0$
m_i	$\frac{\partial m_i}{\partial r} = 0$	$\frac{\partial m_i}{\partial r} = 0$	m_i specified (1 for Central and 0 for Other Inlets)	$\frac{\partial m_i}{\partial x} = 0$	$\frac{\partial m_i}{\partial x} = 0$
k	Given by Wall Functions	$\frac{\partial k}{\partial r} = 0$	k specified	Given by Wall Functions	$\frac{\partial k}{\partial x} = 0$
ϵ		$\frac{\partial \epsilon}{\partial r} = 0$	ϵ specified		$\frac{\partial \epsilon}{\partial x} = 0$

where S_R is the swirl ratio which is presumed known. The inlet value of k is prescribed as a given fraction of the inlet mean kinetic energy. Note that in the absence of data for turbulence intensity in all three orthogonal coordinate directions, the assumption of isotropy is necessarily invoked in specifying k as a fraction of U_{in}. The design of inlet, therefore, becomes all the more critical to ensure that extreme anisotropy is not present there. The inlet specification of ϵ follows from

$$\epsilon = k_{in}^{1.5} C_{\mu}^{0.75} / (0.09\Delta), \tag{7}$$

where Δ is the specified boundary-layer thickness and C_{μ} is a constant of the turbulence model (see Table 1). Note that this specification differs from those of References 2-4 which use an inlet turbulence-length scale related to the radius for the central inlet and to the difference of radii for the annular inlet.

Finally, in Table 2, m_i includes m_f, f and h. Since no CO_2 is present in the inlet stream, according to Equation (2), f assumes the same inlet value as m_f (i.e., 1 at the central inlet and 0 at both the annular air inlets). The specification of inlet values of T satisfies the corresponding requirement on h [see Equation (3)]. The vanishing (axial and radial) derivative conditions at other boundaries require no explanation, except for the fact that the use of the Neumann condition on h at the duct wall and centerbody face implies the assumption of an adiabatic wall. For cooled walls, the specification of constant wall temperature should be used as the boundary condition on h at the solid surface. Thus, Table 2 must be interpreted appropriately for the variable h.

4. COMPUTATIONAL DETAILS

The application of the TEACH procedure in the numerical treatment of the Reynolds-averaged Navier-Stokes equations described in Paragraph II.2 is well known. The details concerning the underlying theory and the computational procedure are available in Reference 2 (for the standard version) and Reference 5 (for the refinements), as well as in the bibliography cited therein. For the present discussion, it is sufficient to note that the solution procedure (Reference 5) involves the Bounded Skew-Upwind Differencing (BSUD) method of Raithby (Reference 8) in place of the hybrid upwind differencing scheme used previously. The calculation of the pressure field which required the SIMPLE algorithm in Reference 2 is based upon the Pressure-Implicit Split Operation (PISO) in Reference 5. PISO involves an iterative predictor-corrector scheme in which the velocity is first calculated for a guessed pressure distribution from the momentum equations; then the pressure field is corrected so as to have the velocity field satisfy the overall continuity equation, and the cycle is repeated. Reference 5 must be consulted for the details of the finite-difference procedure.

a. Swirl Characteristics

Since the highlight of the present study is the inclusion of swirl in the inflow and the computation of the azimuthal velocity field in an otherwise axisymmetric geometry, we will discuss briefly some aspects of the swirling flows relevant to our calculations.

The key requirement of a gas-turbine combustor is that the flame remain lighted over a wide range of operating conditions. This is usually satisfied by the introduction of swirl which causes recirculation in the core region and thereby produces strong shear, high turbulence, and rapid mixing. Moreover, swirling flows provide increased residence time for the fuel in

a combustor of given length. The improvements in the flame-holding characteristics of the recirculation zone with swirl are, of course, accompanied by increased pressure drop. Also, the swirling flows are known to lead to instability in the frequency range of 100-500 Hz range.

Beer and Chigier (Reference 9) define the swirl number as a measure to characterize the amount of rotation imparted to the axial flow. Thus, the swirl number

$$S_N = 2\, G_m/(D_s G_t), \tag{8}$$

where D_s is the outer diameter of the swirling jet and G_m and G_t denote respectively the integrated axial flux of the angular momentum and the axial momentum flux. These can be written as

$$G_m = \int_0^{D_s/2} 2\pi r W \rho U dr \tag{9}$$

and

$$G_t = \int_0^{D_s/2} 2\pi r \rho U^2 dr \quad . \tag{10}$$

The nature of the flowfield is determined by the magnitude of the swirl number. Thus, for $S_N < 0{\cdot}4$, there is no recirculation in the potential core of the jet and the swirl is said to be weak. For $0{\cdot}4 \leq S_N \leq 0{\cdot}6$, the swirl is moderate and there is considerable divergence of the streamlines but without recirculation. $S_N >> 0{\cdot}6$ denotes strong swirl, a condition characteristic of swirlers of practical interest. Note that in Equation (8) the axial momentum of both the central and annular streams is taken into account.

In the combustor configuration of Figure 1 much of the axial momentum is contained in the annular streams, especially the outer nonswirling flow. The main purpose of the latter is to create a toroidal recirculation zone behind the bluff body.

The strength of the recirculation zone depends not only on the axial momentum of the outer annular stream, but also on the blockage ratio D_c/D_d, where D_c and D_d are the diameters of the centerbody and the confining duct respectively. The flow reversal of the central jet is generally affected by both the recirculation zone of the outer annular stream and the swirl of the inner stream. Unfortunately, no correlation is available for the relationship between the flow-reversal characteristics of the central jet and the axial momentum of the annular stream, as well as the blockage ratio. Therefore, the present computational experiment makes use of a parameter called the Flux Ratio F_R, defined as the ratio of the axial momentum of the outer annular stream to the combined momentum of both the central jet and the inner annular stream.

b. Computational Domain

The finite-difference grid employed for the computational experiment on the proposed combustor is shown in Figure 2. In the construction of this grid with 37 axial nodes and 36 radial nodes, an exponential stretching was used in the axial direction to yield a denser grid near the face of the bluff body. In the radial direction, an arbitrary choice of 6, 5, and 11 mesh points corresponds to the central jet radius and the inlets of the inner and outer annular streams. We believe that the computational mesh of Figure 2 should be adequate to resolve the initial development of the flowfield with reasonable accuracy. A comprehensive experiment, however, is required to investigate the grid sensitivity of the computed solutions.

c. Computational Parameters and Test Cases

Some of the constants needed by the governing equations and by the turbulence and combustion models therein are shown in Table 1. The other constants used in the present computations are: $\mu_\ell = 1{\cdot}88\text{x}10^{-3}\text{Ns/m}^2$, $\rho_{air} = 1{\cdot}1609\ \text{kg/m}^3$, $T_{wall} = 293°\text{K}$ and

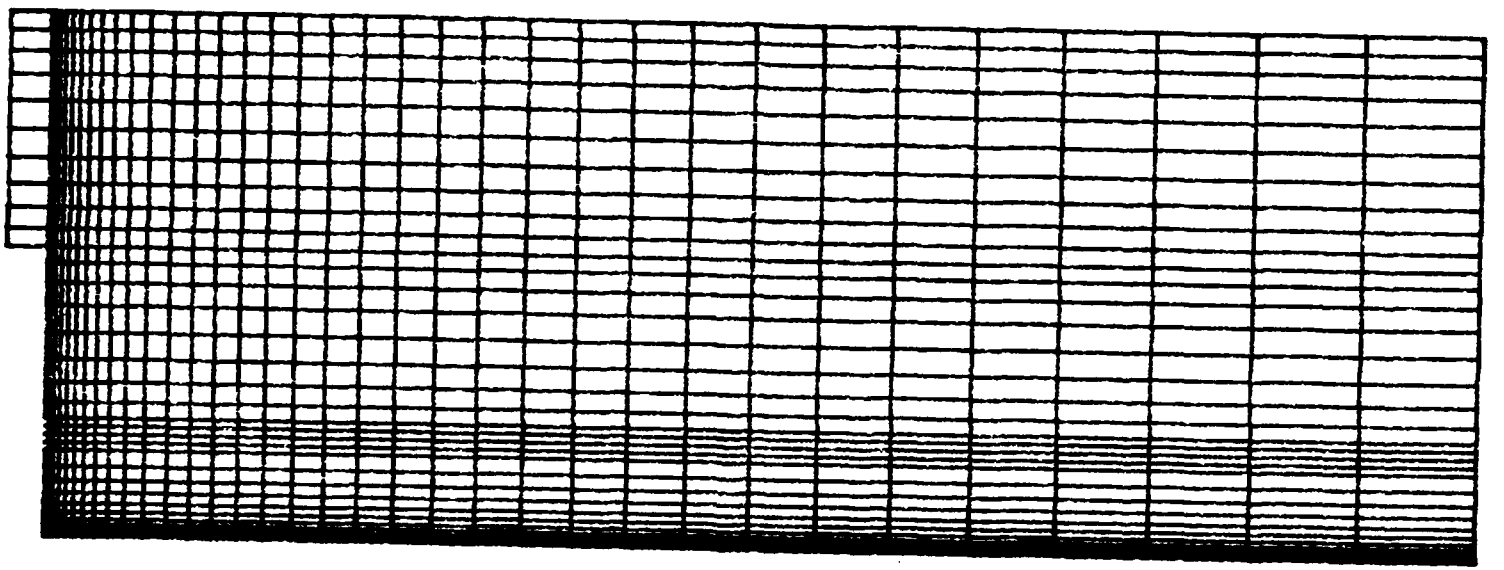

Figure 2. Finite-Difference Computational Grid.

(for the combustion of propane) $H_R = 5{\cdot}008 \times 10^7 J/kg$. The various parameters used in the different test cases are presented in Table 3. Unless stated otherwise in this table, the inflow conditions used are the following: Pressure p = 98,000 Pa, boundary-layer thickness $\Delta = 0{\cdot}01$ m, $k/U_{in} = 0{\cdot}005$, temperature of the central jet = 400°K, and the temperature of the outer and inner annular streams = 293°K. Note that in Table 3 the outer and inner air streams are referred to as the annular and middle flows.

The different test cases we examined are characterized by different values of the axial velocities of the three streams and by the different ratios of swirl-to-axial velocities. Of course, only the middle stream has nonzero swirl velocity. The central jet consists of CO_2 or propane, depending on whether nonreactive or reactive flow is considered. Cases 1-8 of Table 3 correspond to the former and cases 9-10 correspond to the latter.

The parameters describing the swirl characteristics are presented in Table 4. Thus, the swirl numbers S_N considered in the present study varied from 0·0 to 0·85. Also seen in Table 4 are the values of the flux ratio F_R [discussed in Paragraph II.4.a] used for the different cases. F_R varies from 3·76 to 142·63. Thus, the values of F_R for cases 7-10 (corresponding to an outer annular mass flow of 2 kg/s) are an order of magnitude larger than the values for cases 1-6 (corresponding to a mass flow $\leq$ 1 kg/s). This distinction gives rise to the annular-stream dominant flowfield and the interactions therein with swirl and combustion which are discussed in Section III. From Tables 3 and 4 it is easy to recognize the very large parametric variation possible in the computational experiment. The limited subset of 10 cases we have investigated merely provides the flavor in analyzing the effect of swirl on the flowfield in the proposed combustor.

TABLE 3
INLET FLOW CONDITIONS FOR DIFFERENT CASES EXAMINED

CASE	1	2	3	4	5	6	7	8	9	10
ANNULAR FLOW										
AXIAL VELOCITY, m/s	24.42	24.42	24.42	24.42	8	8	49.3	49.3	49.3	49.3
SWIRL/AXIAL VELOCITY	0.0	0.0	0.0	0.0	0.0	0.0	0.0	0.0	0.0	0.0
TURBULENT KINETIC ENERGY/ (AXIAL VELOCITY)^2	0.005	0.005	0.005	0.005	0.0001	0.0001	0.005	0.005	0.005	0.005
BOUNDARY LAYER THICKNESS, m	0.01	0.01	0.01	0.01	0.1	0.1	0.01	0.01	0.01	0.01
MIDDLE FLOW										
AXIAL VELOCITY, m/s	19.8	19.8	39.6	39.6	19.8	19.8	19.8	19.8	19.8	19.8
SWIRL/AXIAL VELOCITY	1.0	1.0	1.0	1.0	0.0	1.0	0.0	1.0	0.0	1.0
CENTRAL FLOW										
AXIAL VELOCITY, m/s	71.64	143.3	71.65	143.3	69.6	69.6	69.6	69.6	69.6	69.6
SWIRL/AXIAL VELOCITY	0.0	0.0	0.0	0.0	0.0	0.0	0.0	0.0	0.0	0.0

TABLE 4
SWIRL NUMBERS AND FLUX RATIOS FOR DIFFERENT CASES RUN

CASE	S_N	F_R
1	0.7191	34.59
2	0.4449	21.40
3	0.8500	10.22
4	0.7191	8.65
5	0.0	3.76
6	0.7275	3.76
7	0.0	142.63
8	0.7275	142.63
9	0.0	142.63
10	0.7275	142.63

SECTION III
RESULTS AND DISCUSSION

The CFD results for the proposed combustor (see Figure 1) obtained from calculations outlined in the previous section are discussed in the following paragraphs. The predictions for the nonreacting flowfields are presented first and those for the reacting flowfields next. The results for both flowfields are presented and discussed in terms of velocity-vector plots (and temperature- and density-contour plots for reacting flows), centerline (axial) distributions of selected flowfield variables, and radial distributions (at different axial stations) of these variables.

1. NONREACTING FLOWFIELDS

Cases 1 through 8 (see Table 3) are concerned with the nonreacting flowfields. The complex nature of the flowfield interactions in the near-wake region is clearly indicated by the computed velocity field. The following discussion of the overall flow structure discerned from the velocity-vector plots sets the stage for the subsequent examination of the axial and radial profiles.

a. Velocity-Vector Plots

The eight cases of the computed velocity field considered here correspond to only a limited parametric variation of several items of interest. To discern quickly the flowfield interactions when several variables are present, the computational strategy adopted in these eight cases is to keep some parameters constant and vary others. In the first four cases the outer annular mass flow rate (m_a) was kept constant at 1 kg/s, thereby facilitating a comparison of the effects of variation in the mass flow rates of the swirling stream and the central stream. In the next four cases, the effects of variation in the outer annular mass flow and in swirl were examined by keeping the mass flow rates of the other two streams constant.

(1) Variations in Swirling and Central Streams

Cases 1 through 4 consider a value of unity for the swirl ratio S_R (which is defined as the ratio of the tangential to the axial velocity at the inlet) of the inner annular stream. The velocity-vector plots for these four cases are seen in Figure 3. Comparisons of cases 1 and 2 (Figures 3a and 3b), and of cases 3 and 4 (Figures 3c and 3d) show the effect of increasing the central-jet mass flow rate (m_c) at two different swirling-stream mass flow rates (m_s). Comparisons of cases 1 and 3, and of cases 2 and 4 reveal the effect of increasing m_s at two different values of m_c.

Figure 3a shows that the wake is essentially characterized by four vortices. The primary vortex, oriented in the clockwise direction, is centered at the normalized axial and radial coordinates of 0·45 and 0·325 respectively (the normalization being with respect to the centerbody diameter). Two smaller vortices of opposite sense are located in the wake region which is bounded by the centerbody face and the primary vortex in the axial direction and by the centerbody edge and the periphery of the swirling jet in the radial direction. The clockwise rotation of the outer vortex and the counterclockwise rotation of the inner vortex are consistent with the requirements of the overall flowfield kinematics. The swirling jet is drawn in the clockwise direction by the primary vortex. Finally, a complete flow reversal of the central jet occurs with an offcenterline counterclockwise vortex. This gives rise to a forward stagnation point on the centerline. A rear stagnation point, of course, signifies the end of the recirculation zone. The normalized centerline locations of the forward and rear stagnation points are 0·6 and 1·1 respectively.

The swirl number S_N for this case is 0·7191. In view of this large a value ($S_N > 0·6$), we anticipate that

CASE 1
MASS FLOW RATES: ANNULAR= 1.000KG/S, MID= 0.020KG/S, CENTRAL= 6.000KG/HR

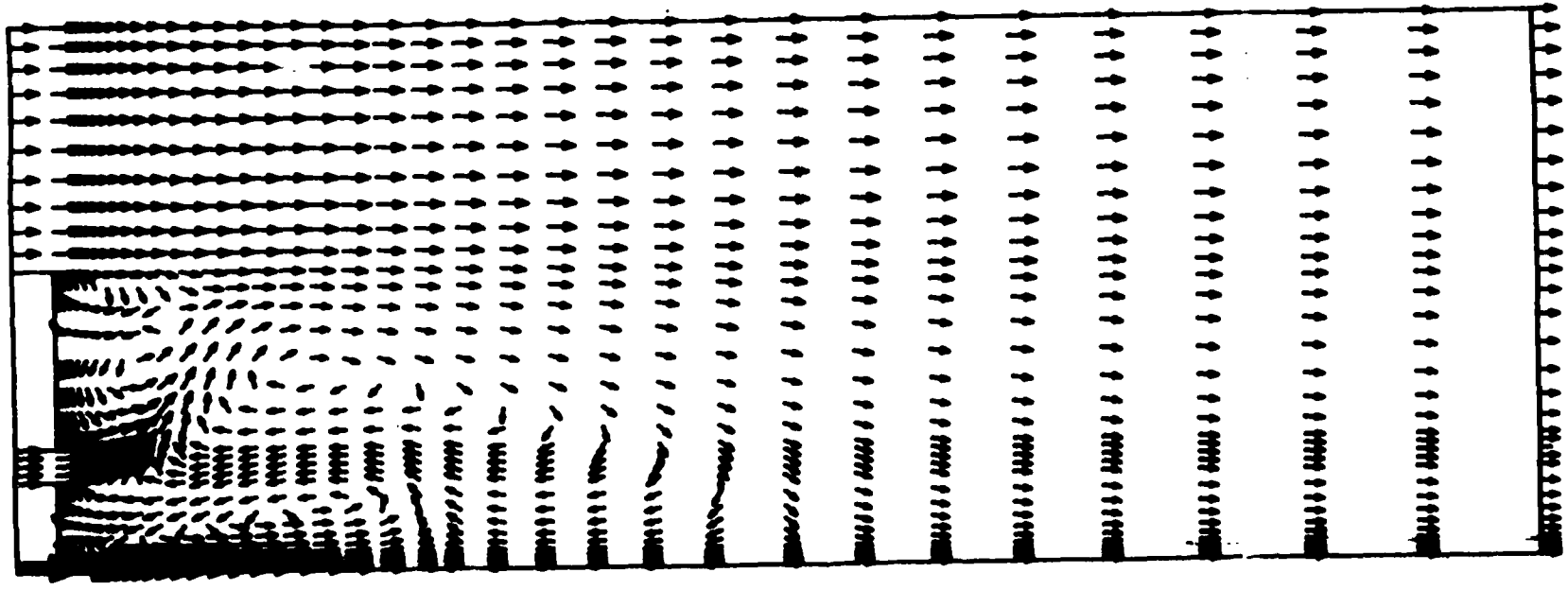

Figure 3(a). Velocity-Vector Plots.

CASE 2

MASS FLOW RATES: ANNULAR= 1.000KG/S, MID= 0.020KG/S, CENTRAL= 12.000KG/HR

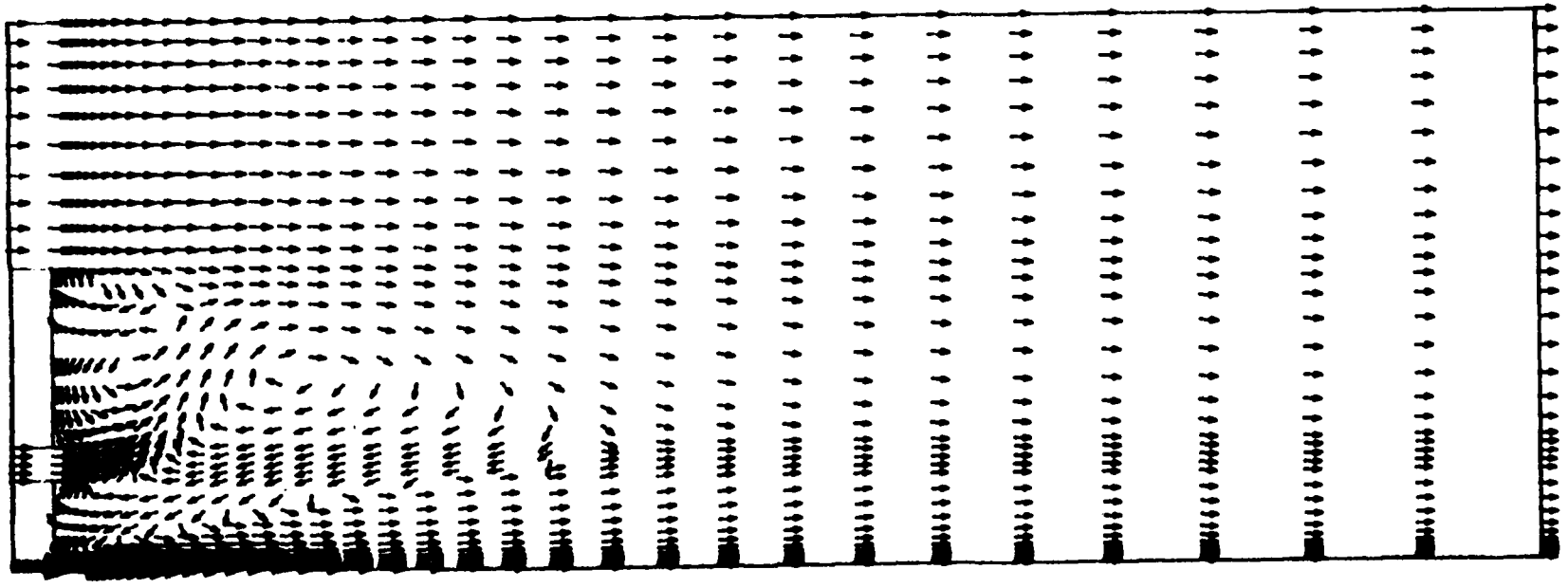

Figure 3(b). Velocity-Vector Plots.

CASE 3

MASS FLOW RATES: ANNULAR= 1.000KG/S, MID= 0.050KG/S, CENTRAL= 0.000KG/HR

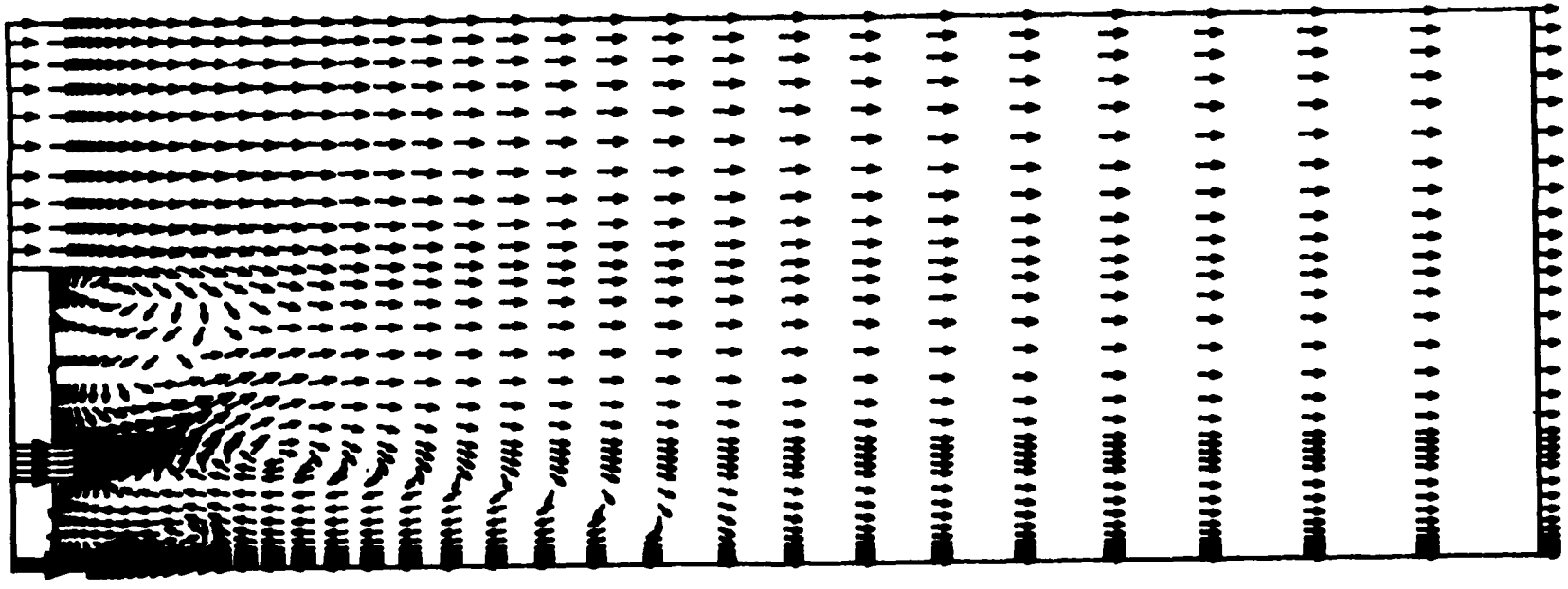

Figure 3(c). Velocity-Vector Plots.

CASE 4

MASS FLOW RATES: ANNULAR= 1.000KG/S, MID= 0.056KG/S, CENTRAL= 12.000KG/HR

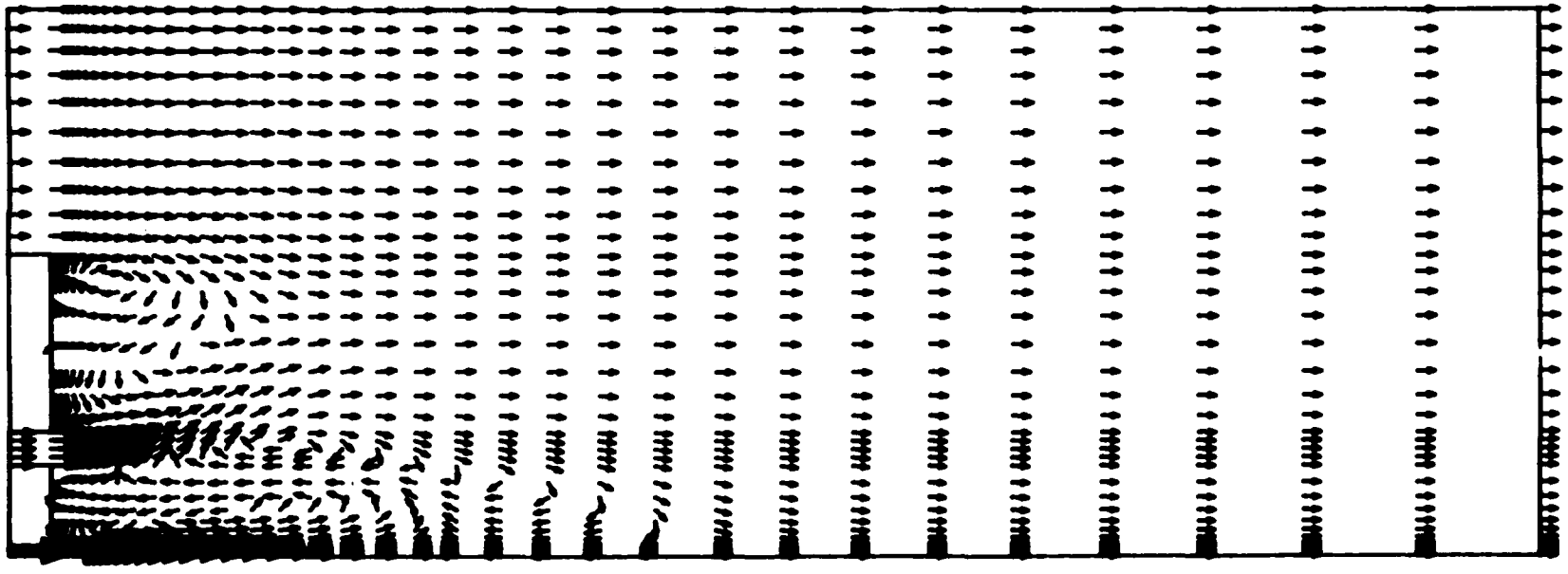

Figure 3(d). Velocity-Vector Plots.

the central-jet flow reversal may arise from the swirling stream alone. This is so because with sufficiently strong swirl, a low-pressure region is created, thereby resulting in a recirculation of the core region. The overall effect of the swirling stream would then appear to be the creation of better mixing characteristics in the wake region, with relatively much smaller mass flow in the outer stream.

A comparison of Figures 3a and 3b shows that by increasing the central-jet mass flow rate from 6 to 12 kg/hr, the primary recirculation region is penetrated by the central jet. Although the centerline flow reversal has disappeared in Figure 3b, the location of the primary vortex center remains relatively unchanged from that of the previous case. The swirl number here is 0·44. This suggests that a relatively moderate swirl combined with the moderate outer annular mass flow (1 kg/s) is not sufficiently strong to cause the centerline-flow reversal. Farther downstream, the central jet does grow in size since it entrains fluid from the surrounding region.

Doubling the mass flow rate of the swirling stream (as compared to Figure 3a of case 1) results in a flowfield which is dominated by the swirling stream, as seen in Figure 3c. Table 4 indicates that the swirl number for this is 0·85. The primary vortex is seen to collapse radially inwards, with the vortex center lying within the swirling stream at a normalized distance of approximately 0·355 from the centerbody face. The normalized locations of the forward and rear stagnation points are now 0·30 and 1·105 respectively, indicating thereby that the increase in S_N from 0·7191 to 0·85 halves the distance of the centerline forward stagnation point.

In case 4 the central-jet mass flow increases to 12 kg/hr (as compared to 6 in case 3) and S_N decreases to 0·7191. Figure 3d shows that the forward stagnation point has moved farther downstream to 0·68. It appears that the swirl is very

effective in causing the central-jet flow reversal and in enhancing the mixing thereof. Furthermore, despite the higher value of central-jet mass flow, flow reversal in the present case has been achieved by increasing the swirling mass flow from 0·028 to 0·056 kg/s and the swirl number from 0·44 to 0·7191 (as compared to case 2).

(2) Variations in Swirl and Outer Annular Stream

Cases 5 through 8 consider constant values of m_c (= 5·76 kg/hr) and m_s (= 0·028 kg/s). A comparison of cases 5 and 6 reveals the effect of swirl on the central-jet flow reversal at a low value of outer annular mass flow (m_a = 0·328 kg/s). Cases 7 and 8 provide this comparison at the much higher value of m_a (= 2 kg/s). Note that cases 5 and 7 are swirl-free (S_R = 0), while cases 6 and 8 have a nonzero swirl (S_R = 1).

The presentation of the velocity fields for cases 5 and 6 as a composite plot in Figure 4a facilitates the examination of the effect of swirl on the central-jet flow reversal. The bottom half of the plot corresponds to case 5 and the top half to case 6. The swirl-free flowfield in case 5 shows that there is no centerline-flow reversal at all. The flowfield is seen to be characterized by the presence of two weak counter-clockwise (it should be kept in mind that this is so only below the centerline) vortices in the wake. The outer one, of course, is the primary vortex due to the (outer) annular flow past the centerbody. The inner vortex is located very close to the centerbody face between the middle and central streams. The incipient tendency for entrainment by both the middle and central streams is also noticeable in the velocity plot. The absence therein of two additional vortices of clockwise direction (again, only below the centerline) necessitated by kinematic grounds, however, may be due to an inadequate spatial resolution in the near-wall regions.

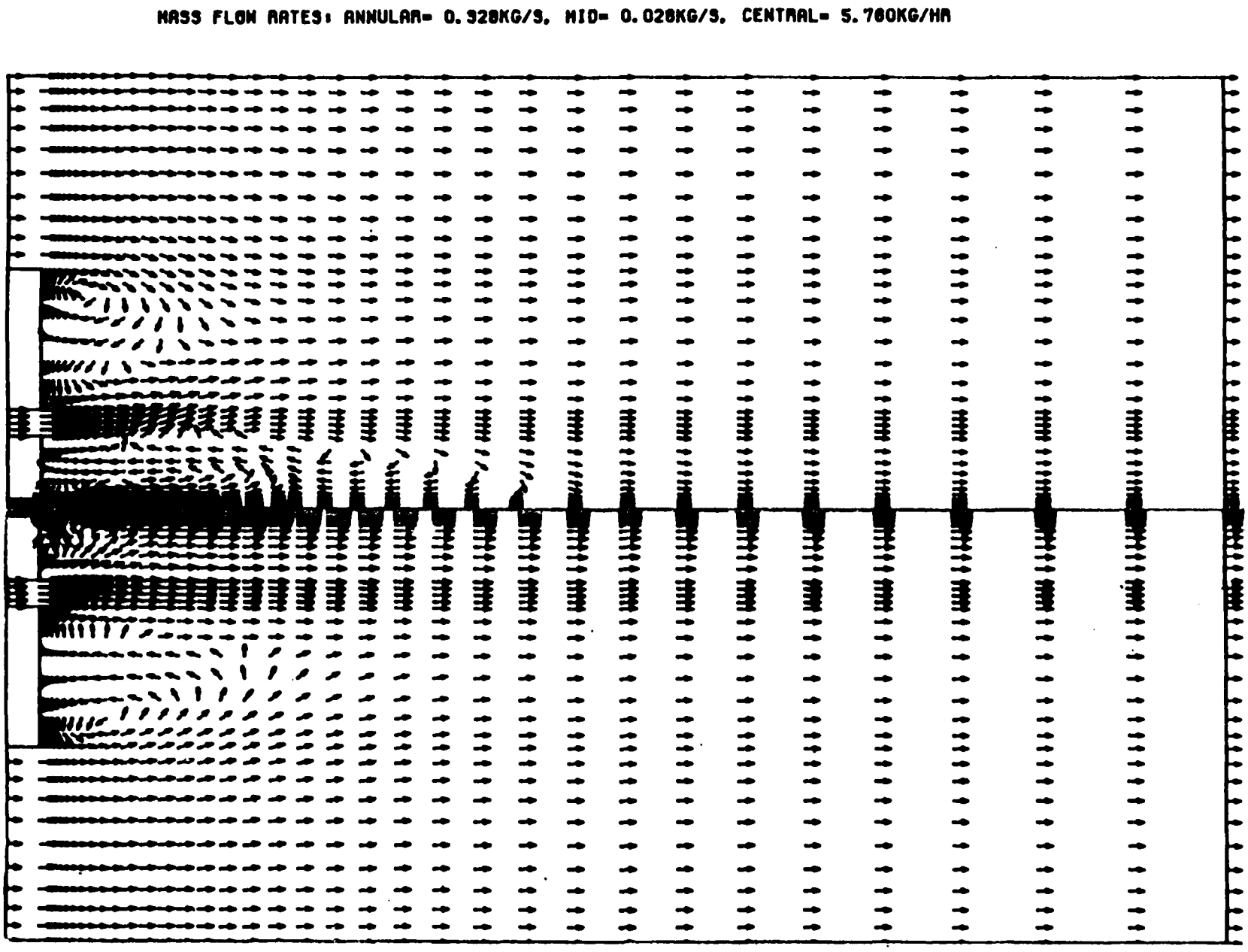

Figure 4(a). Velocity-Vector Plots (Top: Case 6, Bottom: Case 5).

The introduction of swirl in the middle stream dramatically changes the flowfield, as seen in the top half of Figure 4a. The central jet proceeds downstream only about one radius of the centerbody before encountering a complete flow reversal. Thus, centerline forward and rear stagnation points occur at the normalized distances of 0•512 and 1•03 respectively. Furthermore, a comparison of the top and bottom halves in Figure 4a reveals that the flowfield structure near the outer vortex (i.e., radially outside the swirling stream) remains essentially unaffected by the introduction of swirl, whereas rather dramatic changes are noted in the region between the central and swirling streams. Thus, the predominant effect of swirl is felt on the central jet and its vicinity, as we had anticipated (see the discussion in Paragraph II.4.a).

The computed velocity fields for cases 7 and 8 are seen in the composite plot of Figure 4b. The bottom half corresponds to the swirl-free case 7 and the top half to the swirling case 8. Because of the much higher mass flow in the outer annulus, the near wake is dominated by the large primary vortex and characterized by the centerline-flow reversal, irrespective of the presence of swirl or the lack thereof. Indeed, the outer annular flow is sufficiently strong to cause the reversal of both the central and swirling streams. Thus, the comparison of cases 7 and 8 reveals <u>not</u> the effect of swirl in producing the centerline-flow reversal (as was noted in the comparison of cases 5 and 6), but the subtler effect of the degree to which the presence of swirl modifies the outer-annular-stream dominance. This observation becomes clear from an inspection of the locations of the vortex centers and the centerline stagnation points.

In the absence of swirl, the centerline forward and rear stagnation points are located at normalized distances of 0•465 and 1•455 respectively. With the introduction of swirl, the forward stagnation point has moved closer to the bluff body

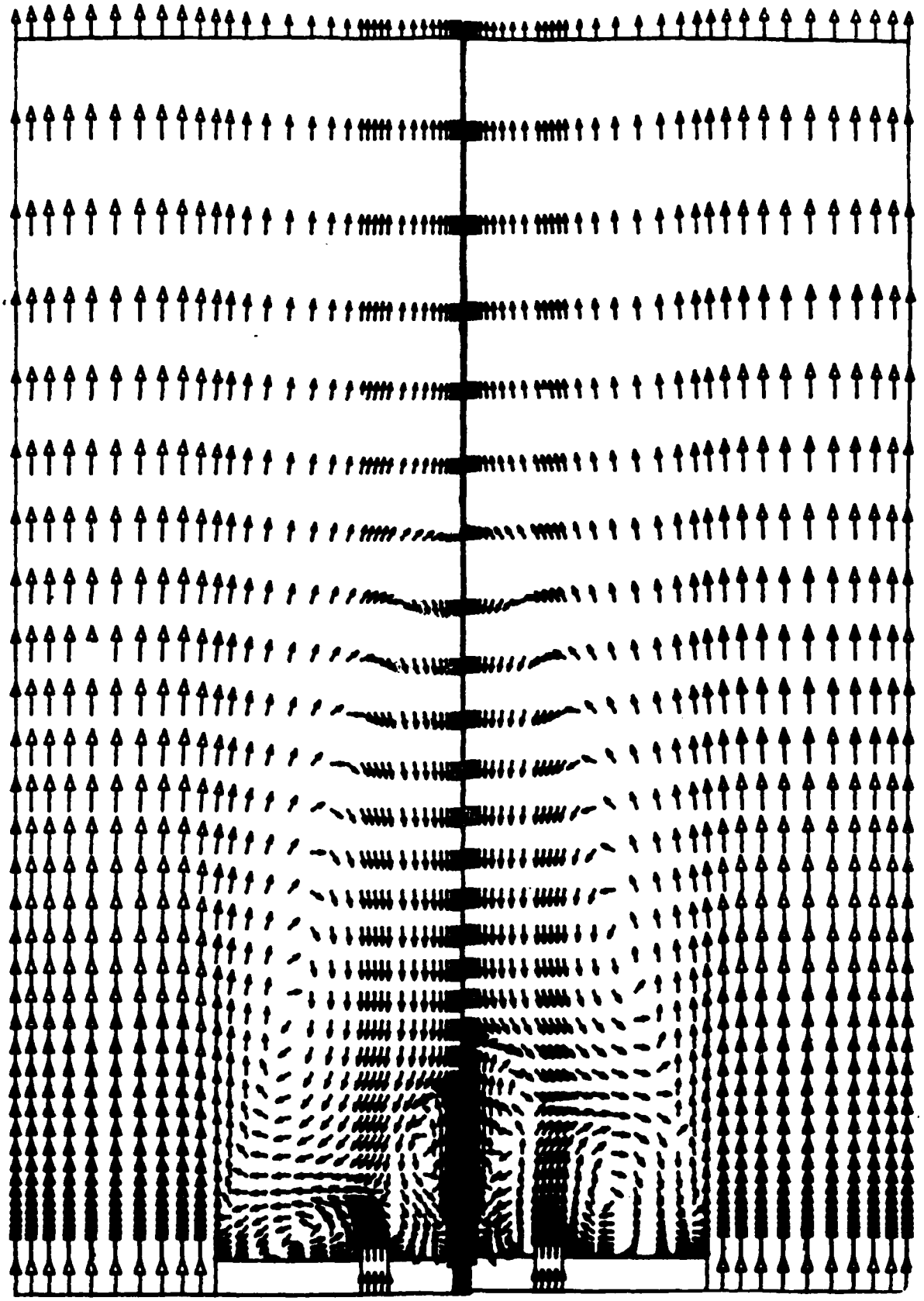

Figure 8. Bottom: Case 7).

and is at the normalized distance of 0·375. Note that the location of the rear stagnation point has remained essentially unaffected. That the predominant effect of swirl is felt only in the near field becomes apparent from some other observations as well. Consider one of the secondary vortices located closer to the bluff body and between the outer and inner annular streams. This is a clockwise vortex in the bottom half and a counter-clockwise one in the top half. The introduction of swirl pushes this vortex even closer to the bluff body, as evidenced by the near halving of both the axial coordinate of the vortex center and the overall size of this vortex (defined, for example, by the region between the bluff-body face and the nearly radially outward velocity vectors). Note that the axial locations of the radially outward turning of the middle stream and a corresponding stagnation point thereof are also more than halved by the presence of swirl in the middle stream. Similar observations hold for the other secondary vortex occurring between the central and middle streams and close to the centerline forward stagnation point. Finally, the introduction of swirl even affects the primary vortex (albeit to a marginal extent). The normalized axial and radial coordinates of the vortex center are 0·575 and 0·295 without swirl and 0·485 and 0·36 with swirl respectively. In other words, with the introduction of swirl the primary vortex is also pushed upstream towards the bluff body and its vortex center moves radially outwards and axially inwards. Thus, the overall effect of swirl is to reduce the spatial extent of the mixing region and thereby enhance the rate of mixing therein.

b. Centerline Variations

Having seen the overall structure of the POSF combustor flowfield in the eight cases, we turn our attention to the axial variation of selected flow variables along the centerline. Present discussion is brief and the prospective reader is encouraged to interpret the noted flowfield behavior in this discussion from an integrated perspective derived from the

overall flowfield description presented earlier and the radial distributions discussed subsequently.

(1) Axial Velocity Fields

The predicted centerline variation of the mean and root mean square (rms) axial velocity components for the eight cases is seen in Figures 5a through 5h. Both the mean (U) and the rms (u) components are normalized by the mean inlet axial velocity (U_a) of the outer annular stream. Note that the assumption of isotropy is invoked in deriving u as given by $(2/3k)^{1/2}$. The abscissa in the plots denotes the axial distance (x) normalized by the centerbody diameter (D).

In all eight cases, the mean axial velocity remains constant for approximately two diameters of the central jet before it shows a linear decay. This linear dependence is observed for $2 \leq x/D_c \leq 6$ to 7·5, where D_c is the initial diameter of the central jet.

For a jet issuing from a nozzle into the ambient atmosphere, the initial distance over which the mean axial velocity component and other scalar variables remain invariant is the potential core. For the present configuration, the predicted potential core of the central jet extends to about 2 jet diameters when both the outer and inner annular streams are present and there is swirl in the middle stream (this is also true of the zero-swirl cases 5 and 7). In the previous ducted centerbody configuration laser Doppler anemometry (LDA) measurements (Reference 10) showed that the potential core of the central jet (in the presence of very low annular air flow which existed merely to carry the seed particles) extended to 6·9-7·5 jet diameters in the mass flow range of 6 to 12 kg/hr. Clearly, in the new POSF configuration the addition of two outer streams and swirl has significantly altered the entrainment characteristics and reduced the length of the potential core.

CASE 1

MASS FLOW RATES: ANNULAR= 1.000KG/S, MID= 0.028KG/S, CENTRAL= 6.000KG/HR

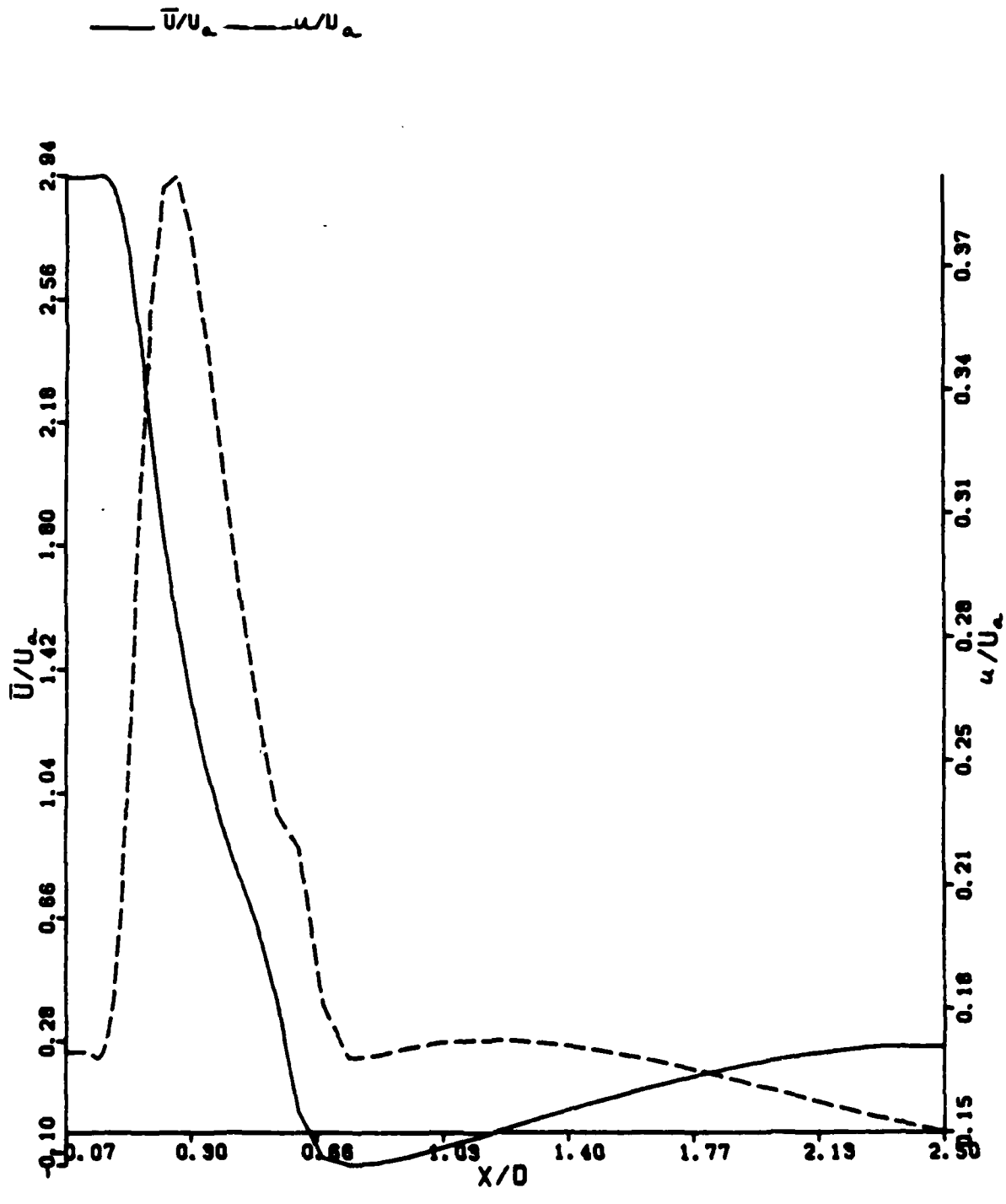

Figure 5(a). Centerline Profiles of Mean and rms Axial Velocity Components.

CASE 2

MASS FLOW RATES: ANNULAR= 1.000KG/S, MID= 0.028KG/S, CENTRAL= 12.000KG/HR

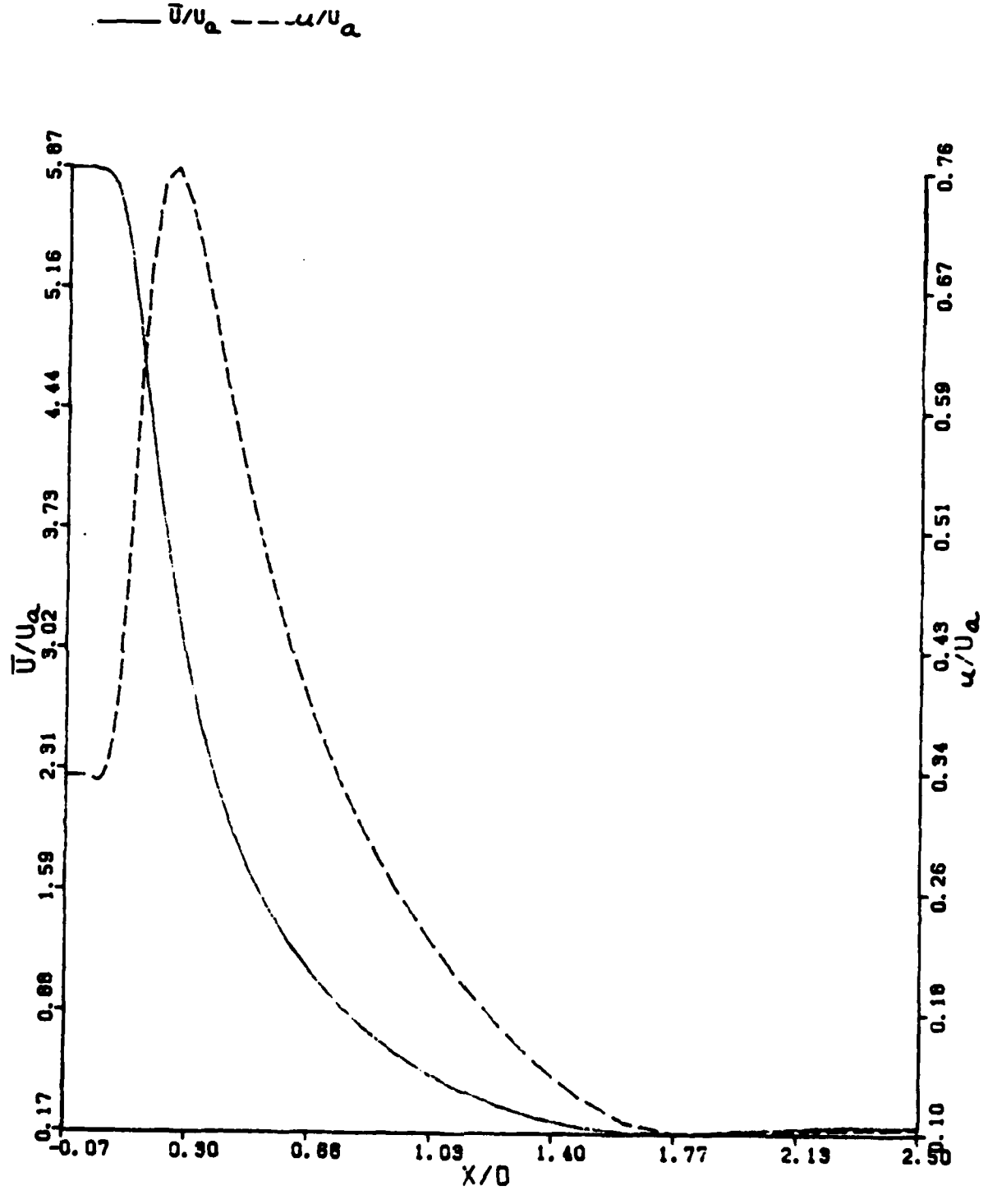

Figure 5(b). Centerline Profiles of Mean and rms Axial Velocity Components.

CASE 3

MASS FLOW RATES: ANNULAR= 1.000KG/S, MID= 0.050KG/S, CENTRAL= 0.000KG/HR

——— $\bar{U}/U_a$ - - - - u/U_a

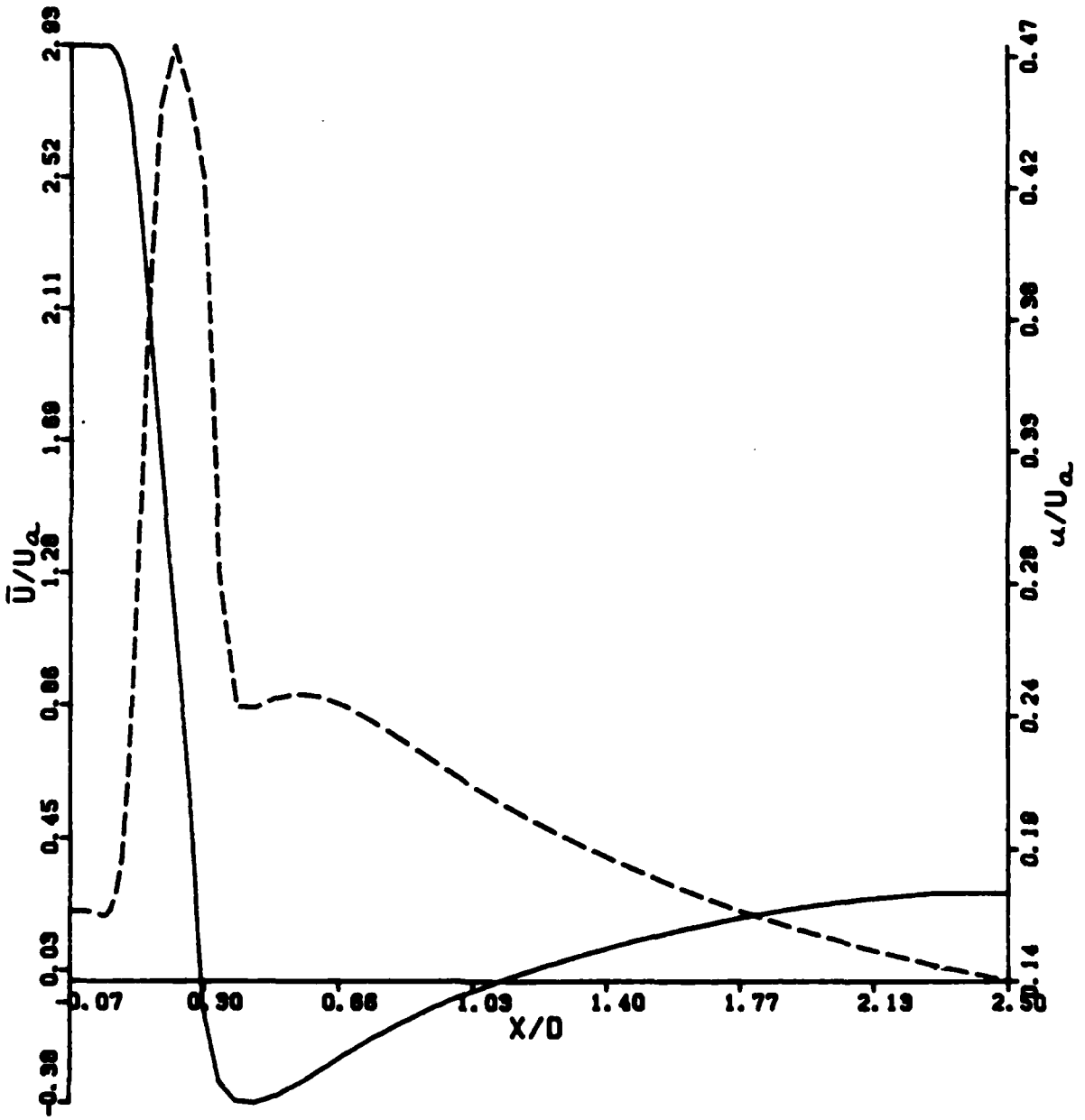

Figure 5(c). Centerline Profiles of Mean and rms Axial Velocity Components.

CASE 4

MASS FLOW RATES: ANNULAR= 1.000KG/S, MID= 0.058KG/S, CENTRAL= 12.000KG/HR

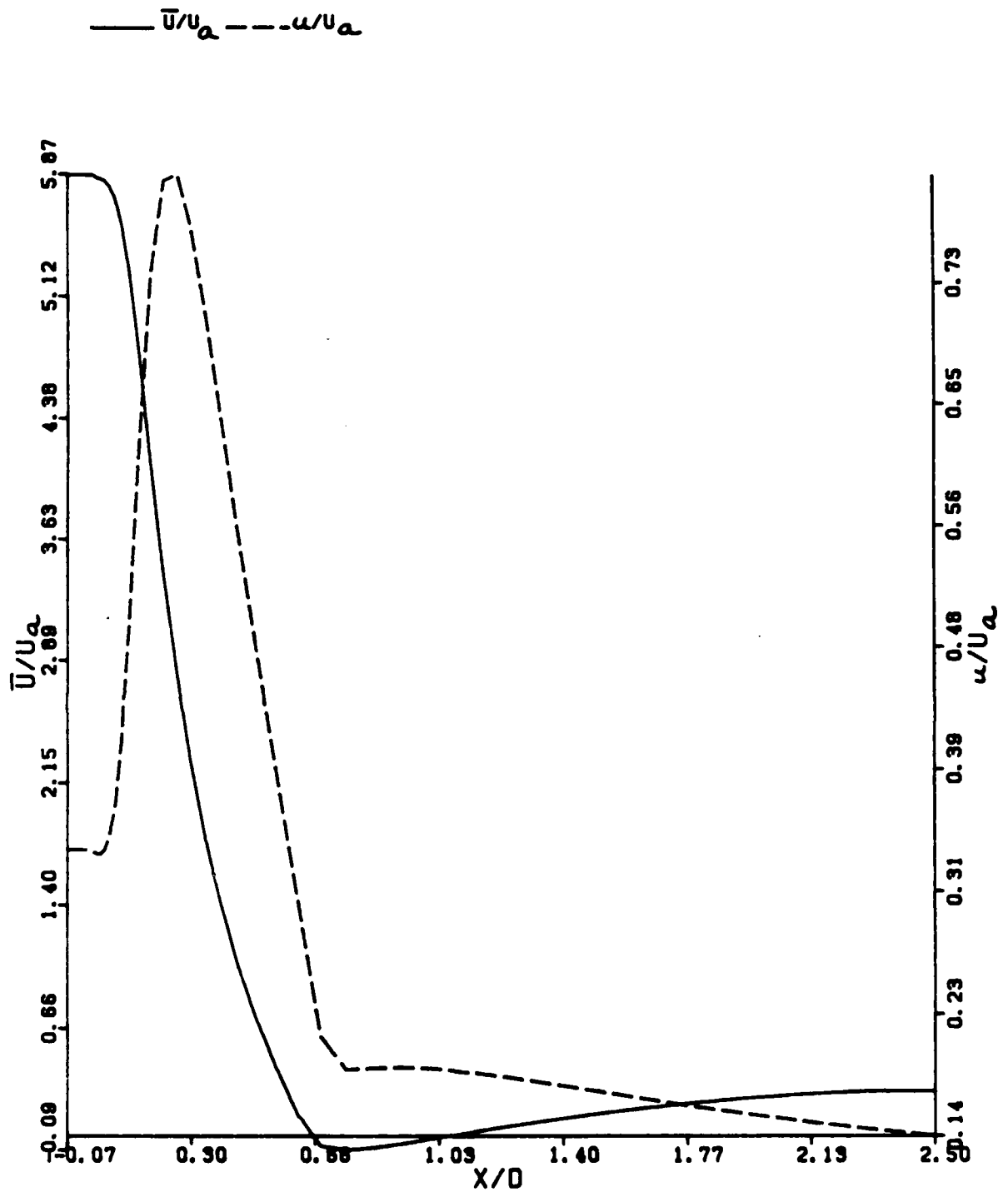

Figure 5(d). Centerline Profiles of Mean and rms Axial Velocity Components.

CASE 5

MASS FLOW RATES: ANNULAR= 0.328KG/S, MID= 0.028KG/S, CENTRAL= 5.780KG/HR

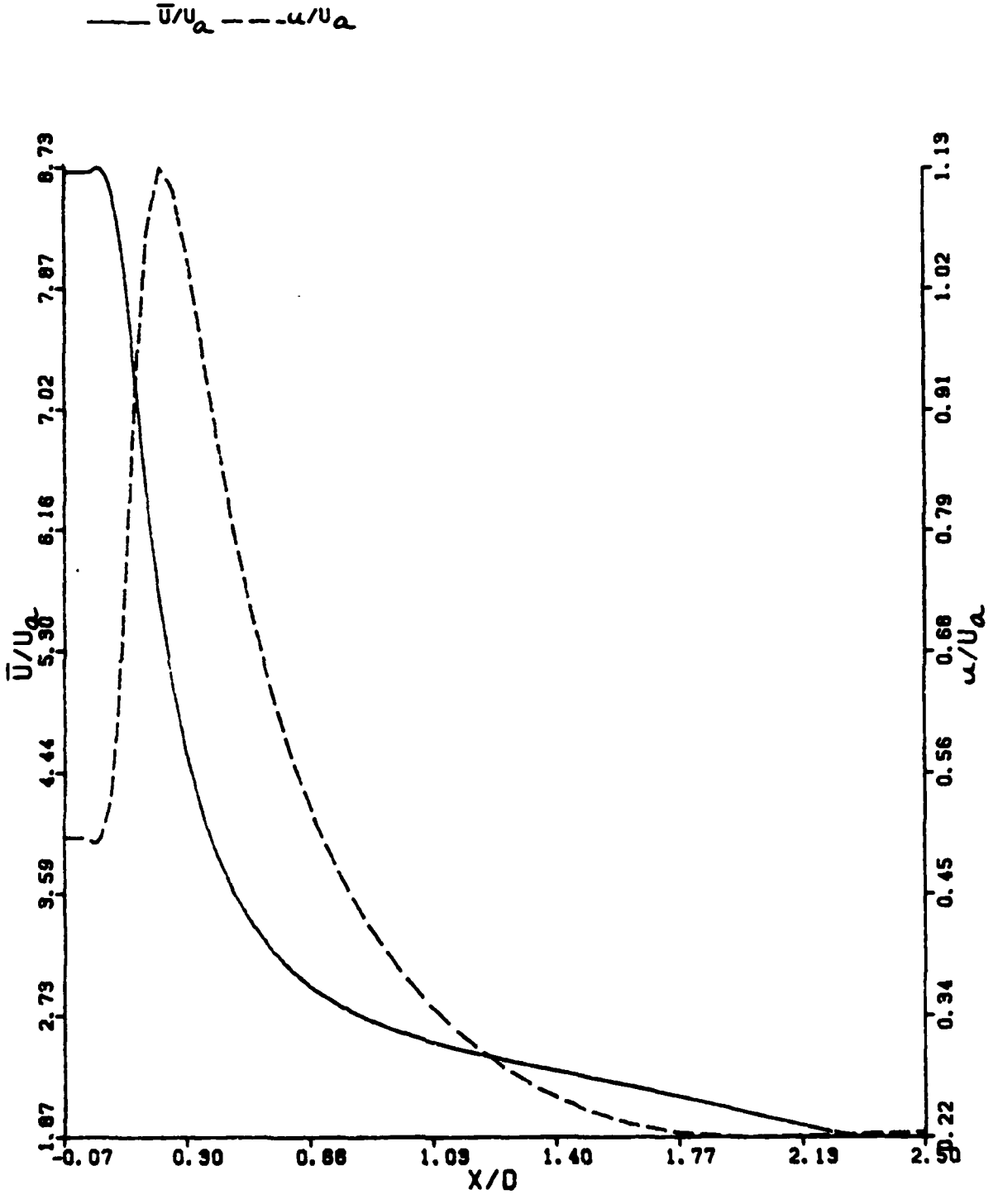

Figure 5(e). Centerline Profiles of Mean and rms Axial Velocity Components.

CASE 6

MASS FLOW RATES: ANNULAR= 0.328KG/S, MID= 0.028KG/S, CENTRAL= 5.780KG/HR

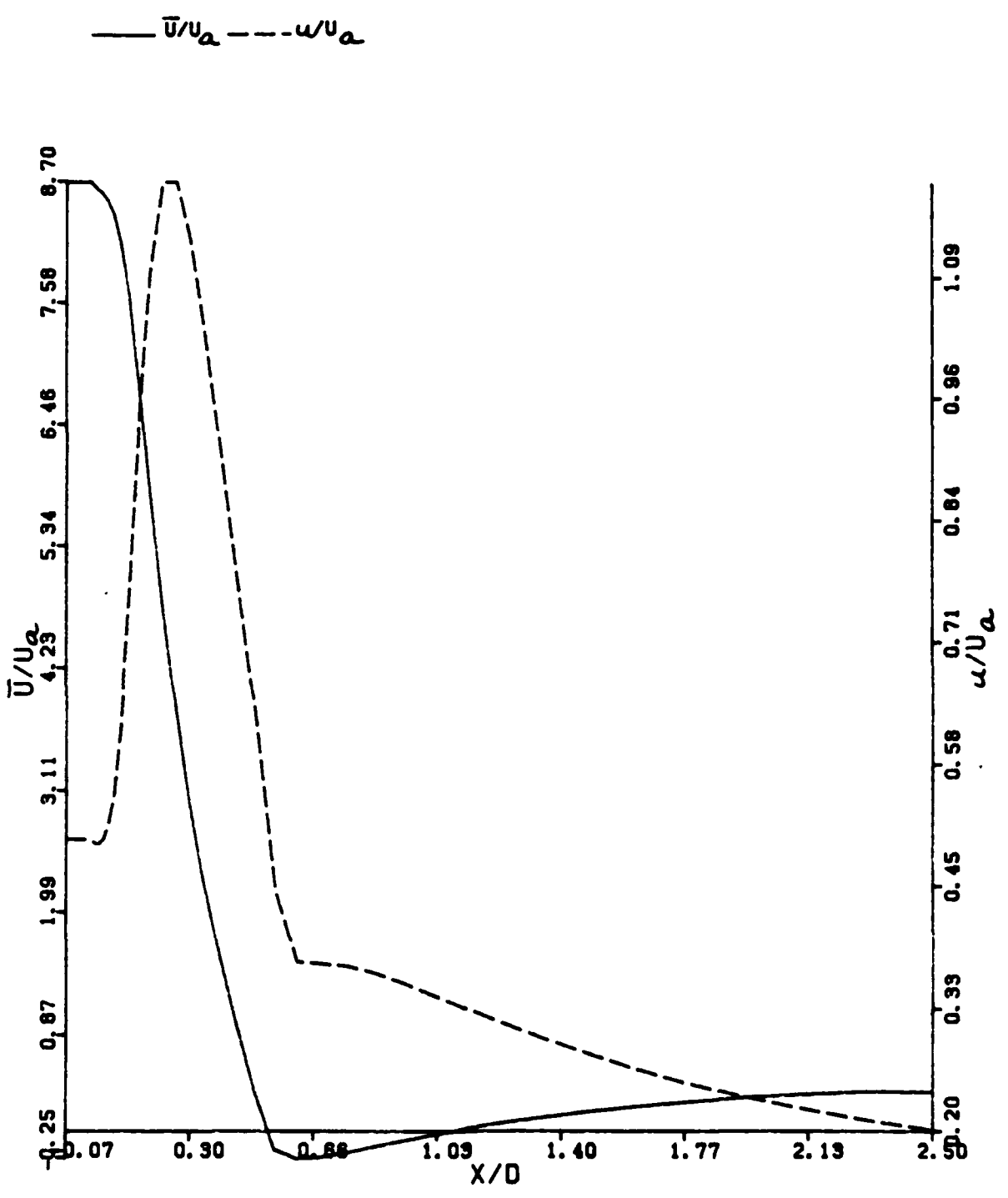

Figure 5(f). Centerline Profiles of Mean and rms Axial Velocity Components.

CASE 7

MASS FLOW RATES: ANNULAR= 2.010KG/S, MID= 0.028KG/S, CENTRAL= 5.760KG/HR

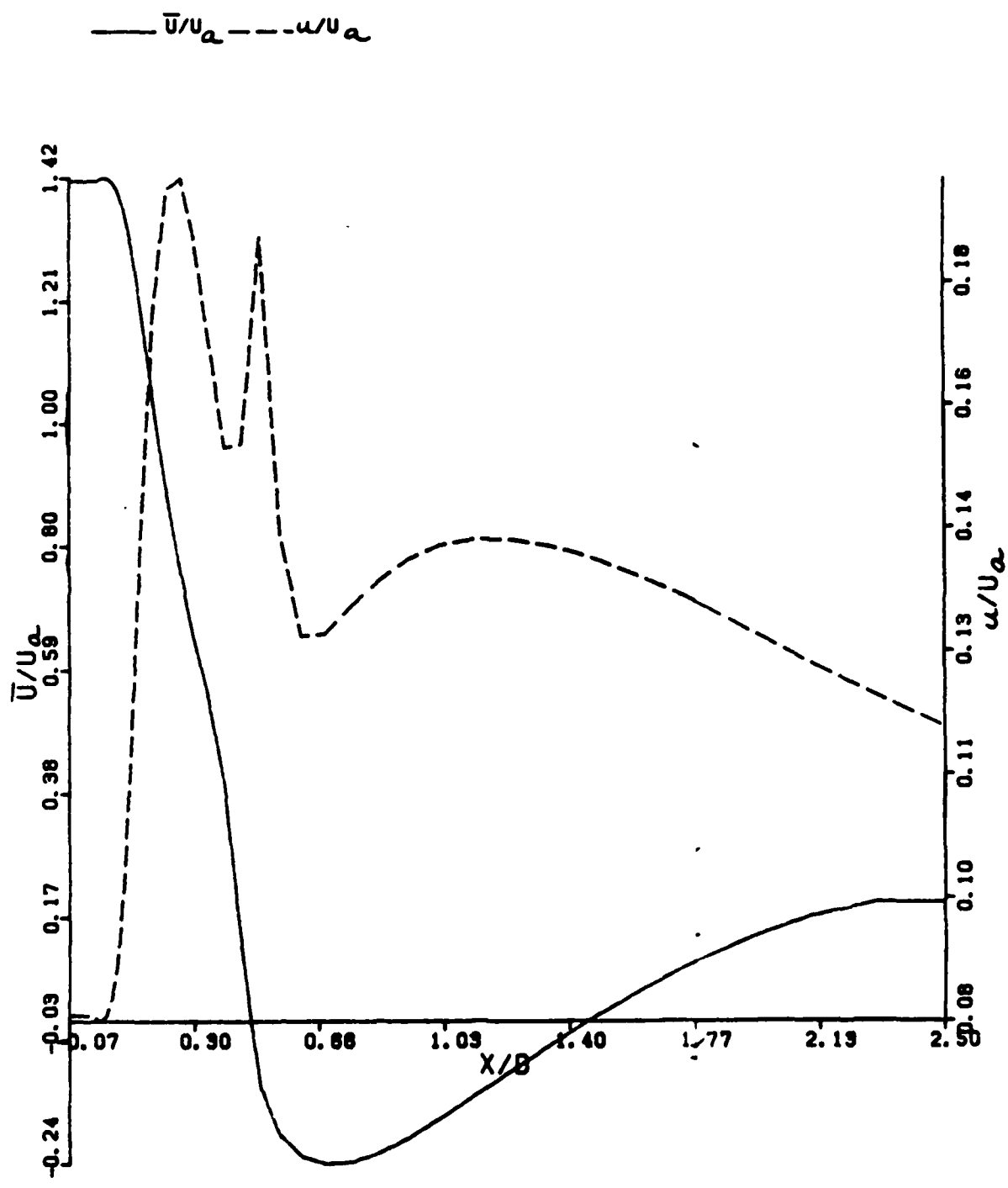

Figure 5(g). Centerline Profiles of Mean and rms Axial Velocity Components.

CASE 8

MASS FLOW RATES: ANNULAR= 2.010KG/S, MID= 0.028KG/S, CENTRAL= 5.760KG/HR

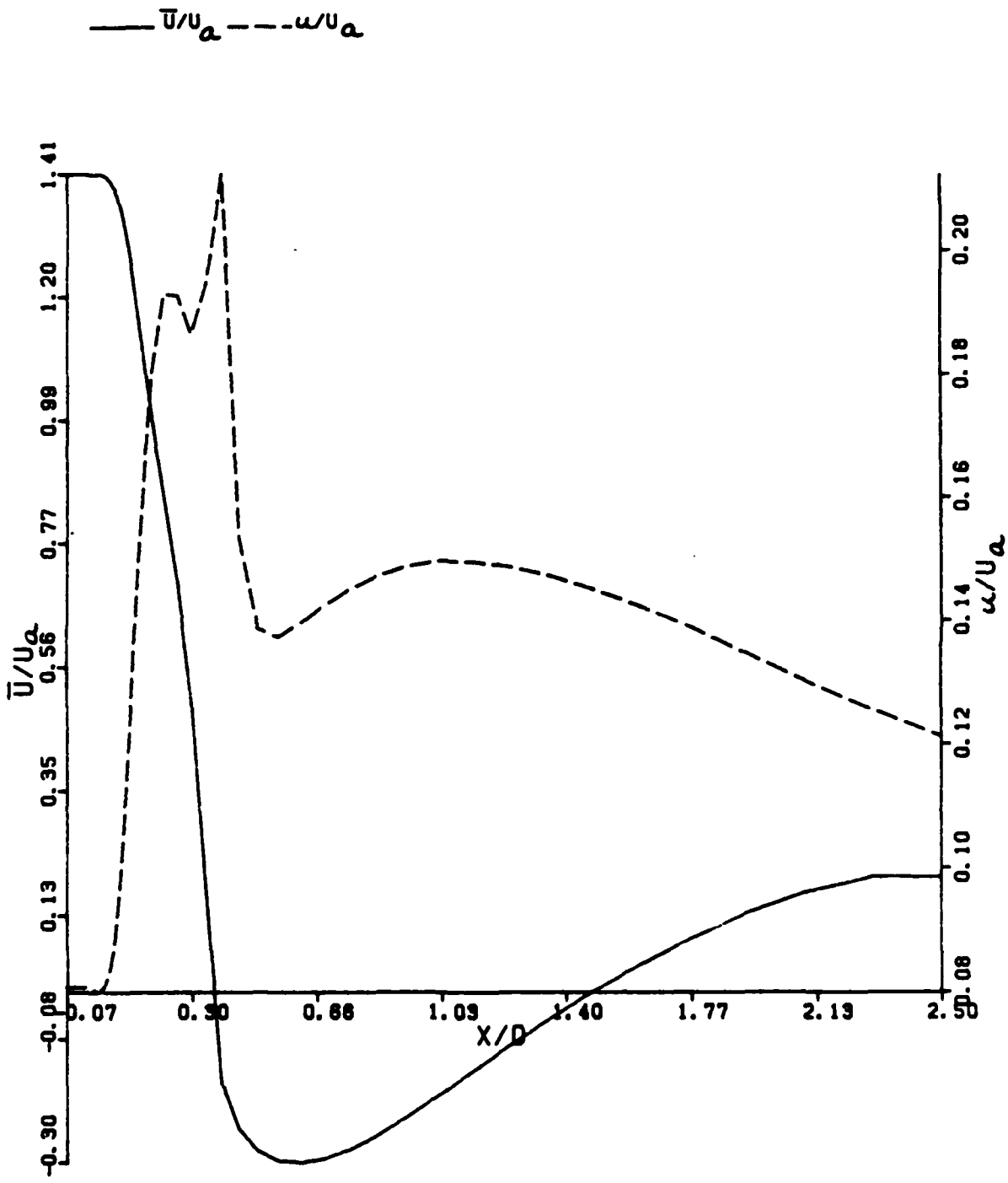

Figure 5(h). Centerline Profiles of Mean and rms Axial Velocity Components.

To the extent that earlier measurements (Reference 10) confirmed that the development of the central jet issuing from a vertical wall (i.e., the bluff-body face) in a confined situation initially resembled free-jet behavior, the present predictions indicate the strong influence of the annular streams on the initial development of the central jet. Let us denote the present potential-core length by L and the previous free-jetlike potential-core length by L_f. What is interesting to note in the present predictions is that L_f is very close to the sum of L and the present distance of linear decay. The reason for this coincidence is not clear.

Figures 5a through 5h further show that the centerline location signifying the end of the linear decay of the mean velocity appears to coincide with the location of the peak rms velocity (or of the first peak in cases with more than one peak). Farther downstream of this peak, the rms velocity starts to fall until the centerline location of the peak negative mean velocity is reached. Beyond this minimum, the rms velocity increases slightly before it tapers off gradually towards the exit boundary. For the two cases (viz., 2 and 5) where the central-jet penetration has eliminated the centerline-flow reversal, the rms velocity falls gradually towards the exit boundary after its peak at L_f (see Figures 5b and 5e).

The two cases where the centerline profile of rms velocity exhibits two sharp peaks correspond to cases 7 and 8 of higher mass flow (2 kg/s) in the outer annular stream (see Figures 5g and 5h). While the first peak occurs at L_f, the second peak occurs very slightly downstream of the forward stagnation point. The latter occurrence is certainly reminiscent of the behavior noted in both predictions (References 2-3) and measurements (Reference 10) of the previous POSF centerbody configuration. The second peak in the present predictions is clearly due to the higher momentum flux of the outer annular stream. However, only experimental data in the new configuration can quantitatively validate the present predicted behavior.

For cases with centerline-flow reversal (see Figures 5a, 5c, 5d, 5f, 5g, and 5h), the mean axial velocity increases downstream of the location of the peak negative velocity and past the rear stagnation point. The quantitative accuracy of the predicted rate of recovery beyond the rear stagnation point, however, remains to be verified by measurements.

(2) Temperature and Concentration Fields

Figures 6a through 6h show the centerline variations of CO_2 mass fraction and temperature. Here, the temperature is the normalized variable given by $(T - T_{min})/(T_{max} - T_{min})$, T_{max} being the maximum value of temperature in the flowfield. For the present results, T_{max} is 400°K, corresponding to the inflow temperature of CO_2.

The one thing readily apparent in Figures 6a through 6h is that with the above normalization of the temperature, the centerline profiles of both temperature and CO_2 mass fraction are nearly identical. Of course, this behavior is a direct consequence of the assumption of unity Lewis numbers for both laminar and turbulent transport coefficients of the scalar fields in the numerical computation of these nonreacting cases.

An interesting aspect of the present predictions that is less readily apparent relates to the similarity of the mean axial velocity profiles of Figure 5 and the corresponding scalar profiles of Figure 6. Had the mean velocity in Figure 5 been normalized with respect to the central-jet inlet velocity U_c [instead of the annular velocity U_a as was done in Paragraph III.1.b(1)], we would readily see that the mean axial velocity profile also is nearly identical with the scalar profiles for $x/D_c \leq L_f$. Thus, the profiles of CO_2 mass fraction, normalized temperature, and U/U_c would remain constant over a distance of about $2D_c$ from the centerbody face and then exhibit a linear decay for about 6 to 7·5 D_c. This linear dependence can be

CASE 1

MASS FLOW RATES: ANNULAR= 1.000KG/S. MID= 0.028KG/S, CENTRAL= 6.000KG/HR

——MASS FRACTION OF CO_2---TEMPERATURE

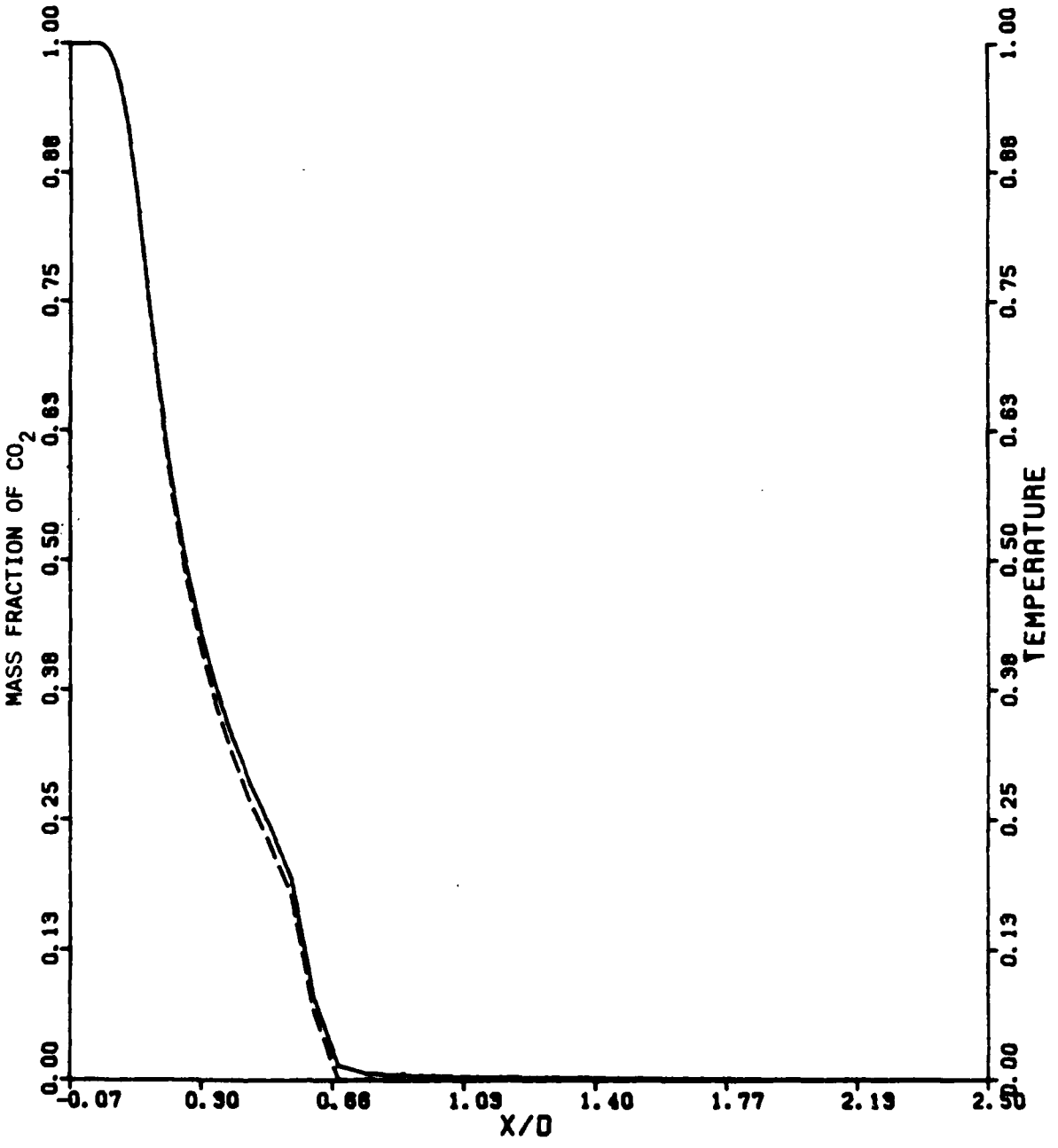

Figure 6(a). Centerline Profiles of CO_2 Mass Fraction and Temperature.

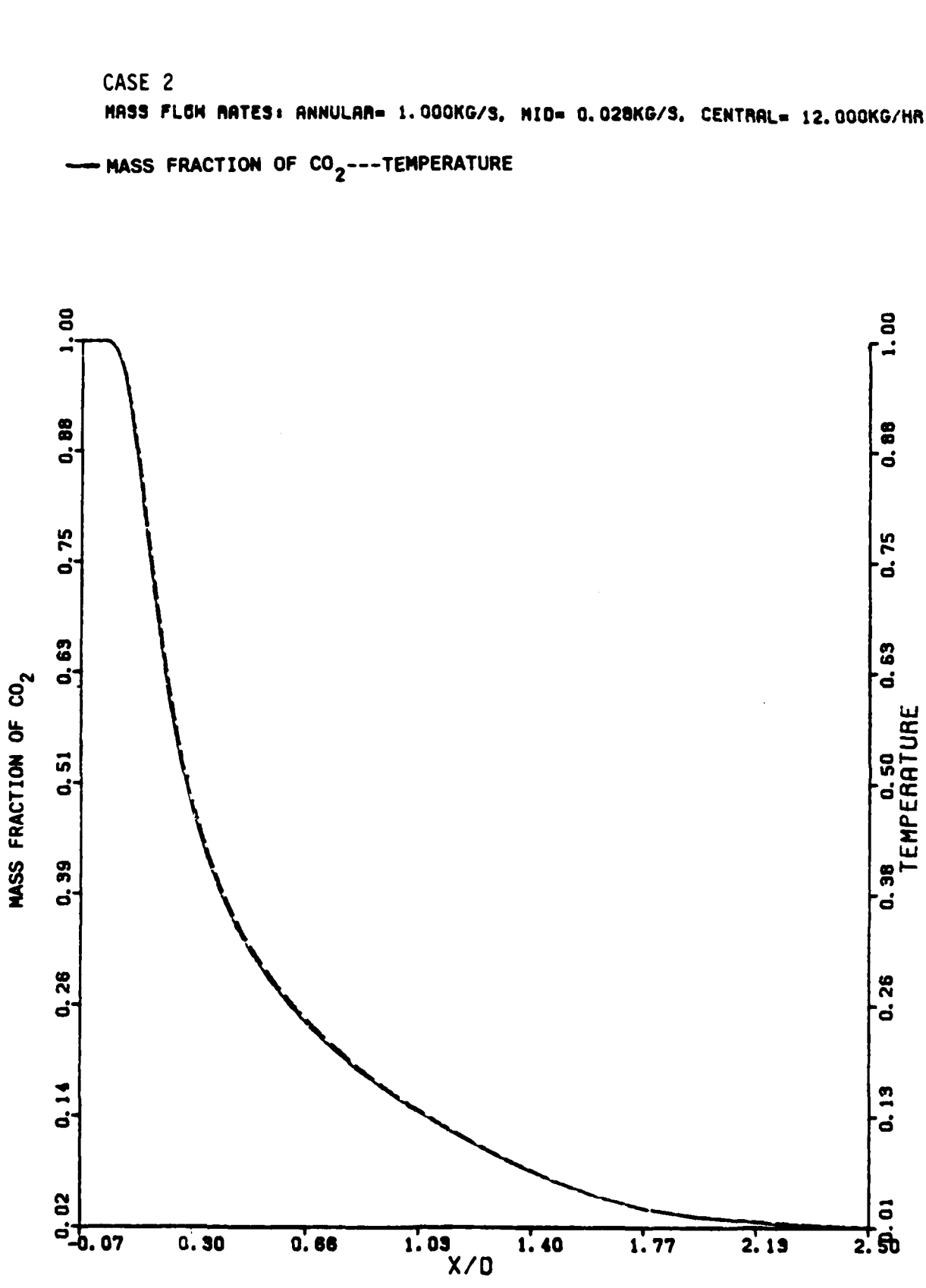

Figure 6(b). Centerline Profiles of CO_2 Mass Fraction and Temperature.

CASE 3

MASS FLOW RATES: ANNULAR= 1.000KG/S, MID= 0.050KG/S, CENTRAL= 6.000KG/HR

—MASS FRACTION OF CO_2---TEMPERATURE

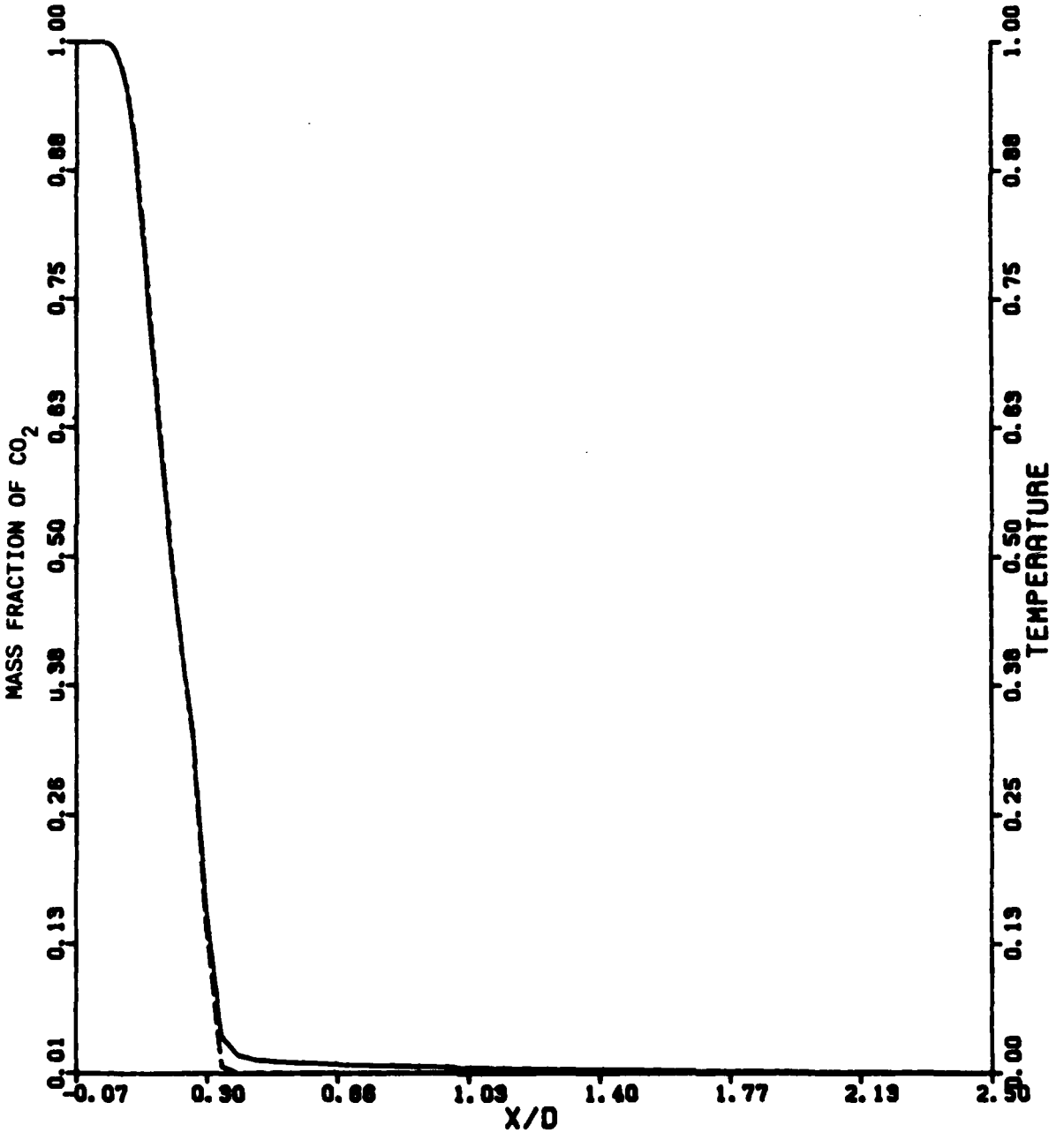

Figure 6(c). Centerline Profiles of CO_2 Mass Fraction and Temperature.

CASE 4

MASS FLOW RATES: ANNULAR= 1.000KG/S, MID= 0.058KG/S, CENTRAL= 12.000KG/HR

——MASS FRACTION OF CO_2---TEMPERATURE

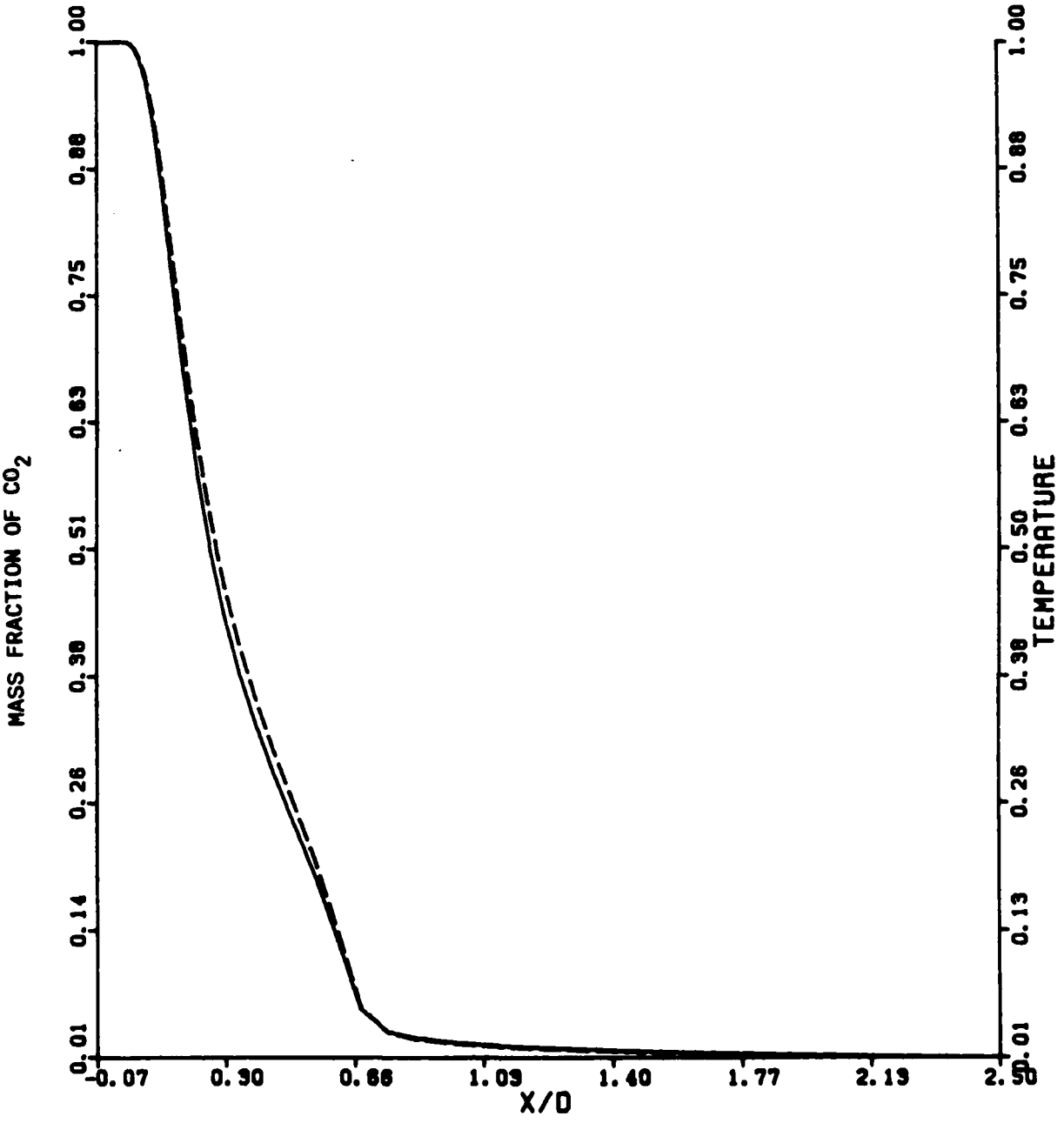

Figure 6(d). Centerline Profiles of CO_2 Mass Fraction and Temperature.

CASE 5

MASS FLOW RATES: ANNULAR= 0.928KG/S, MID= 0.028KG/S, CENTRAL= 5.780KG/HR

—MASS FRACTION OF CO_2---TEMPERATURE

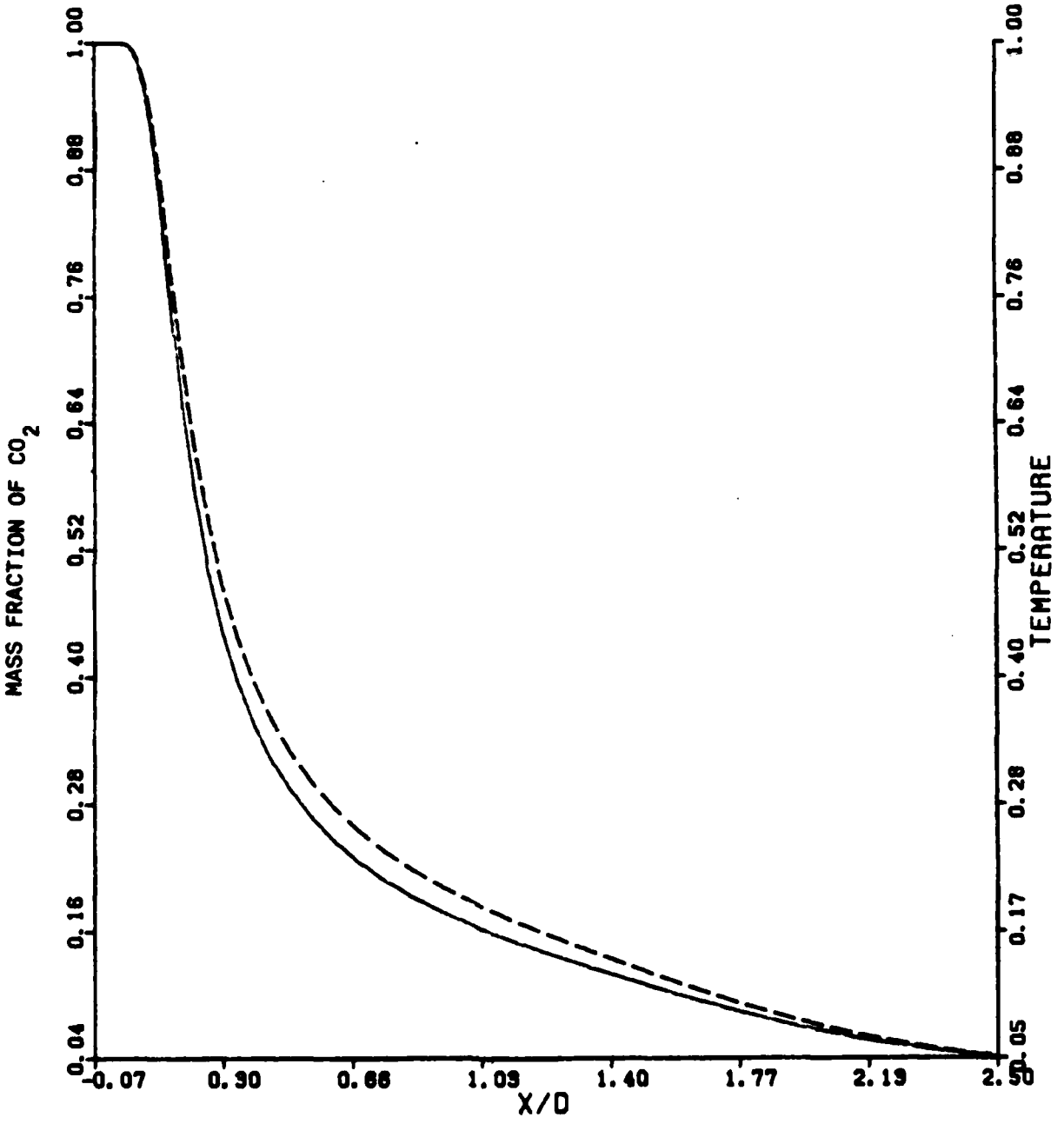

Figure 6(e). Centerline Profiles of CO_2 Mass Fraction and Temperature.

CASE 6

MASS FLOW RATES: ANNULAR= 0.928KG/S, MID= 0.028KG/S, CENTRAL= 5.760KG/HR

—MASS FRACTION OF CO_2---TEMPERATURE

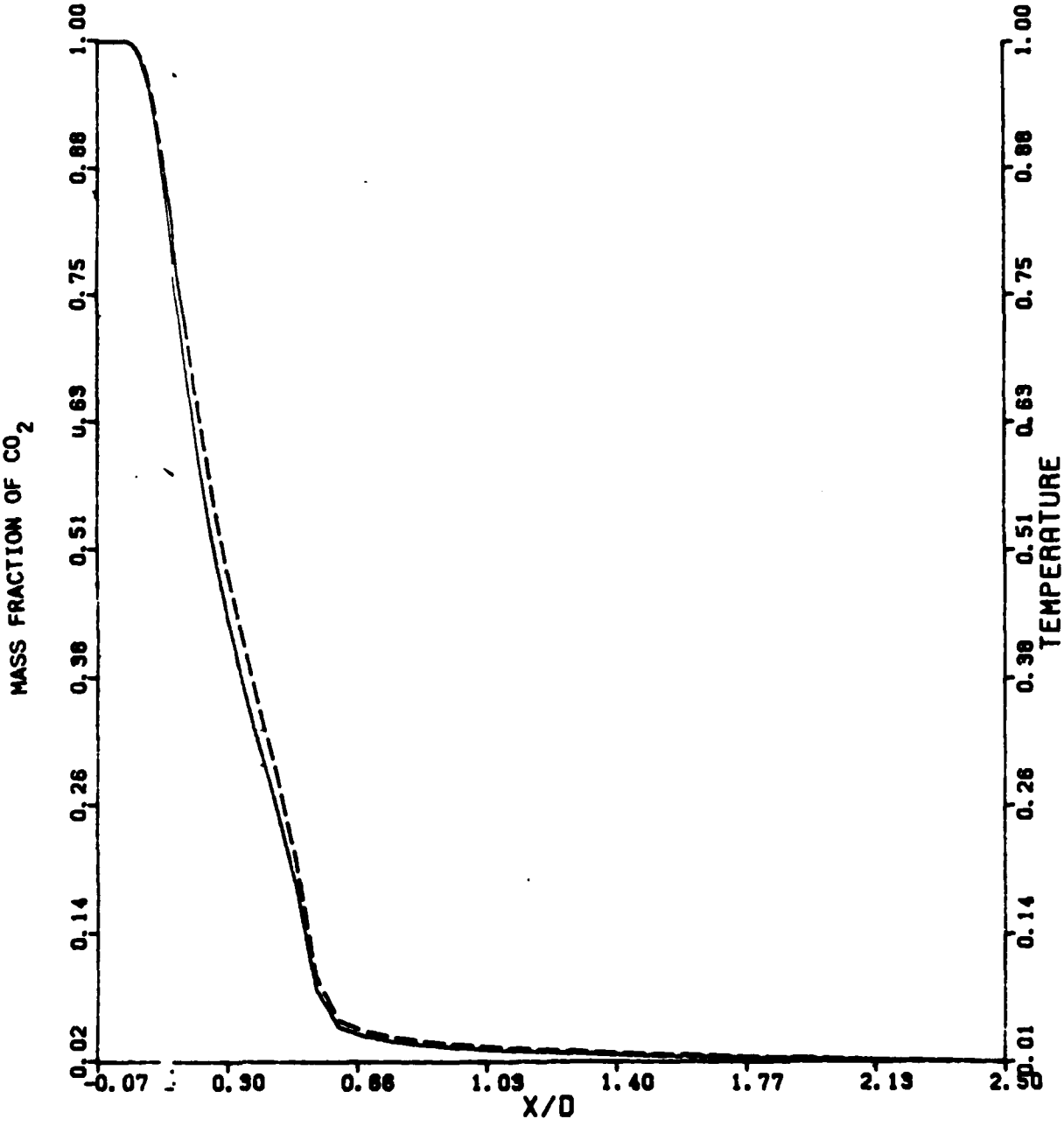

Figure 6(f). Centerline Profiles of CO_2 Mass Fraction and Temperature.

CASE 7

MASS FLOW RATES: ANNULAR= 2.010KG/S, MID= 0.028KG/S, CENTRAL= 5.780KG/HR

—MASS FRACTION OF CO_2---TEMPERATURE

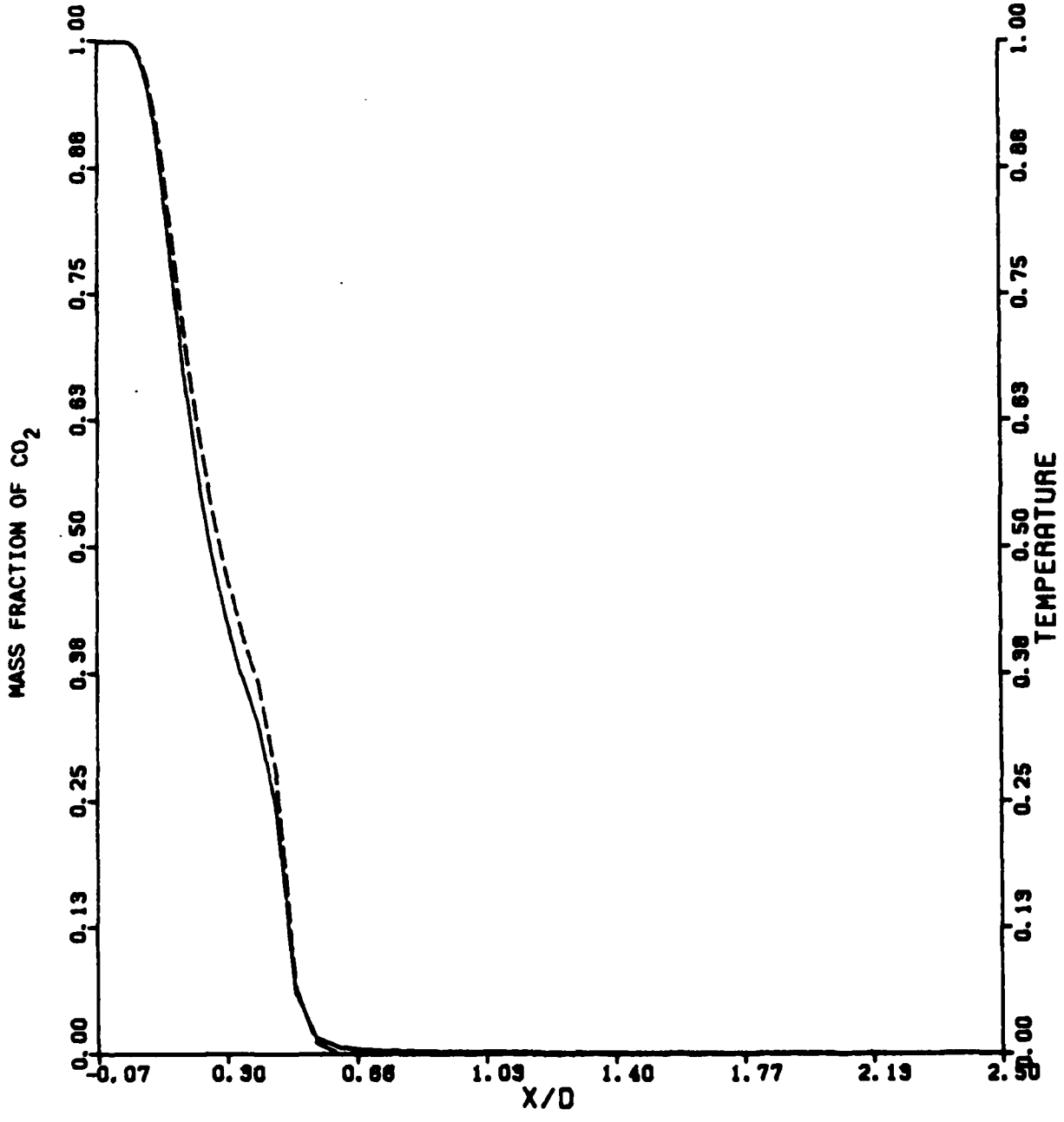

Figure 6(g). Centerline Profiles of CO_2 Mass Fraction and Temperature.

CASE 8

MASS FLOW RATES: ANNULAR= 2.010KG/S, MID= 0.028KG/S, CENTRAL= 5.760KG/HR

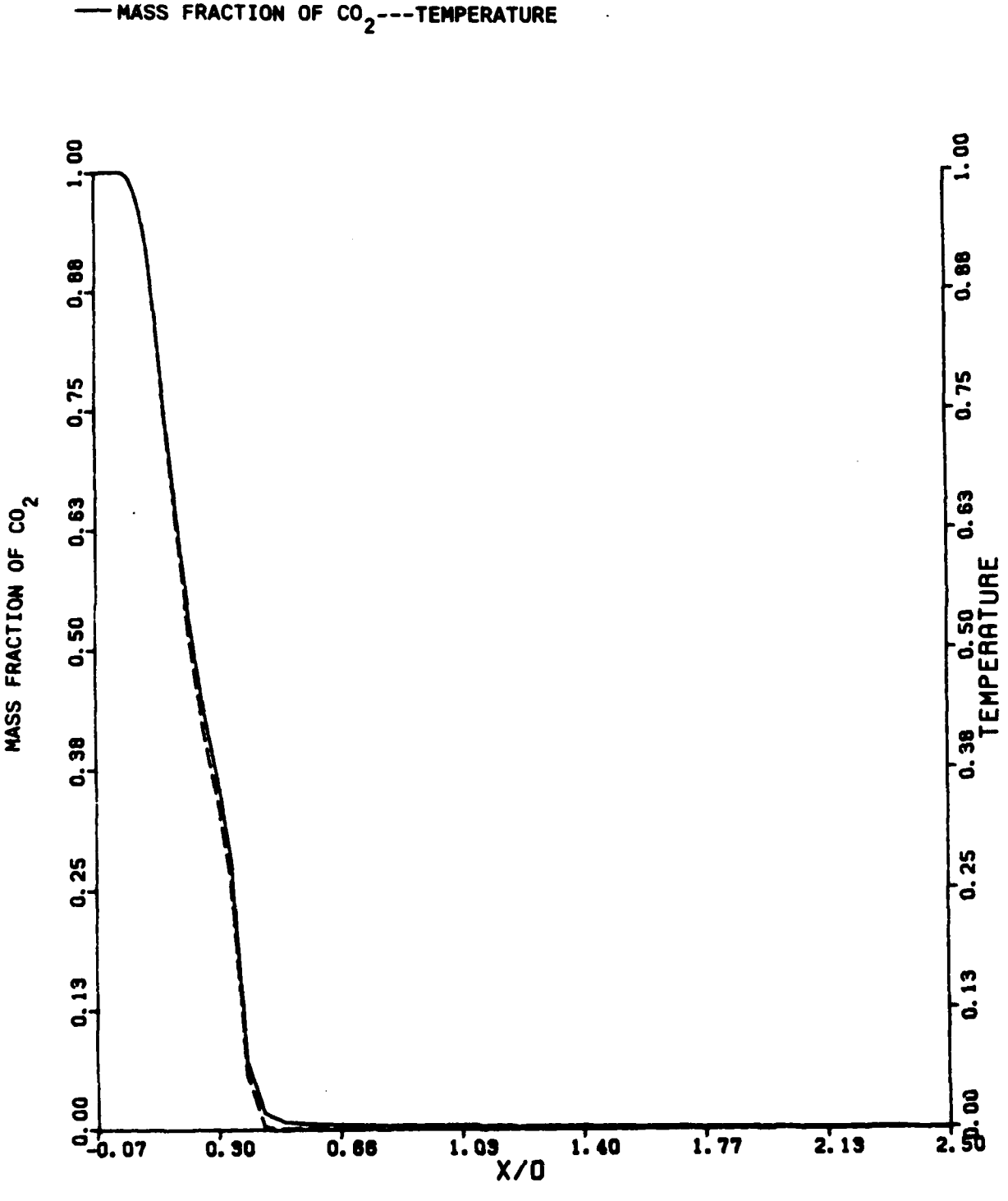

Figure 6(h). Centerline Profiles of CO_2 Mass Fraction and Temperature.

quantified by the following correlation:

$$m_{CO_2} = (T - T_{min})/(T_{max} - T_{min}) = \bar{U}/U_c =$$

$$1 - 0{\cdot}44(x/D_c - 2)/(L_f - 2). \qquad (11)$$

It would be interesting to see if the proposed measurements in the new POSF configuration confirm the correctness of Equation (11).

(3) Implications of Present Predictions

Further examination of the implications of the present predictions of the axial-velocity and scalar fields is instructive. That the development of the central jet in the proposed configuration departs significantly from the free-jet-like behavior noted in Reference 10 should not be surprising. To be sure, the present departure stems from the presence of the outer and inner annular streams, as well as of swirl in the latter (except for cases 5 and 7). These were absent under the conditions of the previous measurements (Reference 10) which addressed the development of a central jet in a negligibly small coflowing annular stream (present solely for carrying the LDA seed particles). Indeed, earlier CFD predictions of the central-jet dominant flowfields also indicated free-jetlike behavior (see, e.g., References 2, 11, and 12). Note that the central-jet dominant flowfields in the proposed POSF configuration also exhibit free-jetlike behavior. This becomes clear from an inspection of Figures 5 and 6 (b and e) corresponding to cases 2 and 5 where the central jet penetrates the recirculation zone and eliminates the centerline-flow reversal. The profiles for the mean axial velocity, CO_2 mass fraction, and temperature exhibit the characteristic 1/x - dependence for a distance of about 30 initial diameters of the central jet. Presumably, the free-jet behavior becomes the better, the smaller the values of m_a and m_s.

Until experimental data from the proposed combustor are available, we cannot ascertain the validity of the myriad implications from the present predictions. Furthermore, the computational procedure of Reference 5 itself has not been tested as comprehensively as the earlier procedures were in References 2-4 and 12. Recently completed CFD research (Reference 13) did attempt a comparative study of the predictions from the old and new procedures, with respect to the measurements in the old centerbody combustor. However, that study only addressed a limited inquiry concerning the primary vortex center and concluded that the new computational procedure was superior in its predictions. Therefore, it is of interest to further scrutinize the present predictions. It must be stressed, however, that the discussion here must be regarded as speculative at best. Note that for the proposed configuration experimental data are not available, and predictions have not been made with the earlier computational procedure. So what is attempted here is a comparative study, the conclusions of which may turn out to have dubious validity.

(a) Aspects of Conformity

For this scrutiny, we consider the swirl-free case 7 which has an outer annular mass flow of 2·01 kg/s, and a central-jet mass flow of 5·76 kg/hr. Although swirl-free, the inner annular stream has the nonzero mass flow rate of 0·028 kg/s. We compare the present prediction for this case with the prediction of the standard k-ϵ model for 2 kg/s annular air flow and 6 kg/hr CO_2 central flow in Reference 2. Figure 21 of Reference 2 compares the prediction and measurement (of Reference 10) for the centerline profiles of the mean and rms axial velocity components. The normalizations of the abscissa and the ordinate in this figure are the same as in Figure 5g. It is noteworthy that the overall trends of the mean and rms velocity profiles in the old and new POSF configurations are similar. The one distinction pertains to the rms velocity profile: the

prediction for the new configuration has two sharp peaks, whereas there was only one in the earlier prediction (i.e., old configuration).

There is reason to believe that the mean velocity profile in Figure 5g will show good agreement with the proposed measurement. Although the initial velocity ratio at present is 1·4 (in contrast with the value of 1·15 in Reference 2), this is a consequence of the different inflow areas in the new configuration. This change in the velocity ratio, of course, explains the increase in the normalized location of the forward stagnation point from about 0·28 (measurement) earlier to about 0·46 (prediction) now (note that there is no linear scaling, however). The increase in the normalized location of the rear stagnation point from about 1 (both measurement and prediction) earlier to about 1·44 (prediction) now is not easily explained by the increase in the velocity ratio. The presence of the middle stream could conceivably have a significant influence in this regard. Note, however, the ratio of the rear-to-forward stagnation point distances in the proposed configuration is 3·13 (prediction). That this is fairly consistent with the value of 3·57 (measurement) in the old configuration provides some quantitative basis for our hope that the present mean-velocity prediction will show reasonable agreement with the proposed measurement.

A comparison of the centerline CO_2 mass fraction profiles in the old and new configurations (Figure 23 from Reference 2 and Figure 6g) again brings out the similarity in the overall trends. As in the case of the axial mean velocity profiles (and certainly because of the differences therein), there are quantitative differences between the old [measurement (Reference 14) and prediction] and the new (prediction) configurations. And some of these differences could be real. Nevertheless, further insights can be gleaned from the scalar profiles. Reference 2 noted how its predictions and the

experimental measurements (References 10 and 14) confirmed the earlier anticipated trends (Reference 11), of a rapid decay first and an equally rapid approach subsequently to uniform values, exhibited by the centerline CO_2 concentration. Reference 2 had also noted that the point of intersection obtained by extrapolating the portions of the profiles that denote the rapid decay and the approach to uniformization in Figure 23 fell very close to the forward stagnation point in Figure 21. Indeed, a rationale for expecting precisely this occurrence had been suggested in Reference 11. It is appealing that the present predictions also display this behavior for the annular-stream-dominant regime. An inspection of Figures 5g and 6g (the linear segment is extrapolated beyond L_f to intersect with the extrapolation of the nearly horizontal segment) reveals this internal consistency of the present predictions. Thus, we conclude that the present predicted behavior of the mean axial velocity, CO_2 mass fraction, and temperature fields should show reasonable agreement with the yet-to-be-available measured results. An experimental verification of the predicted behavior will be gratifying in view of the "true" predictions of the present research.

(b) Area of Disagreement

It is very unlikely that the foregoing will extend to the rms velocity field. Figure 21 of Reference 2 has clearly shown that the predicted rms axial velocity profile compares rather poorly with the LDA results of Reference 10. This discrepancy between the prediction and measurement is especially significant immediately downstream of the bluff body. The assumption of isotropy in the calculations in the face of considerable anisotropic effects in the near wake is known to contribute, at least in part, to the observed discrepancy. There are other aspects of weakness in the standard k-ε model, such as the nonaccounting for the extra strain rates inherent in the large streamline curvature of the flowfield, the noninclusion of

the preferential influence of the normal stresses in the ϵ-equation, etc. It should be noted, however, that as seen in Figure 22 of Reference 3, our ad hoc corrections for these effects did not improve the nature of the rms velocity predictions.

Thus, we believe that the rms velocity profile predicted in Figure 5g may not show as good an agreement with the experimental profile as we anticipate for the mean field comparisons. Such an outcome need not cause surprise or concern. All the earlier CFD research by us and others to address complex recirculating turbulent flowfields by means of the Reynolds-averaged formulation (employing any eddy viscosity derived from the k-ϵ model) has been confronted by this dichotomy of reasonable prediction of the mean field and poor prediction of the fluctuating field. Therefore, it is worthwhile to ask why the mean-field predictions are reasonable and, in fact, are better than could be justifiably expected from the k-ϵ model. The answer to this question could be given at two different levels.

(c) Rationale

On a practical computational level, we could accept the position (advanced by Peter Bradshaw of the Imperial College, among others) that the turbulent-flow behavior is so complex and the search for general closures is so futile that the CFD study of realistic flows will require the development of geometry-specific empiricism. Indeed, this viewpoint has been voiced earlier by Reference 15 which invoked Bradshaw's arguments that in complex flows driven essentially by static pressure gradients, the turbulent shear stresses are at least two orders of magnitude smaller than typical dynamic pressures. Thus, while the details of turbulent stress gradients are locally important and their accurate predictions will require correct modeling assumptions, the global flowfield is relatively insensitive to

model inaccuracies. Furthermore, as emphasized in Reference 15, confined flowfields are characterized by large turbulence production rates at the solid boundaries and by the presence of small length scales (near these boundaries) which provide a ready sink for the turbulence energy. This fact generally leads to a near equilibrium between the production and dissipation of turbulence energy over most of the flowfield and ensures the "success" of the k-ε model in confined flows (Reference 16).

On a more fundamental level, the probable explanation of how much can be computed, and how well, using relatively simple assumptions regarding the turbulence is offered by Lumley (Reference 17). According to Lumley, the plausibility of a turbulence model, even while representing not quite real turbulence, is ensured if it conserves momentum and energy; transports the right amount of everything (e.g., momentum, energy, Reynolds stress, heat flux, etc.), although not by quite the right mechanism; satisfies thermodynamic realizability [in the sense of Schumann (Reference 18), according to which nonnegative quantities are never negative, Schwarz' inequality is always satisfied, etc.]; behaves correctly for both large and small Reynolds numbers; and reduces to real turbulence in one limit (weak inhomogeneity and unsteadiness). Presumably, any model that satisfied all these restrictions would behave about the same and all that remains is to fix the amount of transport through physical input from experiment.

Thus, it would seem that in confined flowfields, such as those exemplified by the old and new POSF combustor configurations, the turbulence is simply a mechanism for momentum transfer, and usually downhill. Modeling the turbulence by any reasonable mechanism (such as the Reynolds-averaged formulation and an eddy-viscosity model) which transports about the right amount, and which guarantees thermo-dynamic realizability will be adequate to describe the global flowfield, so long as the mean motion is handled correctly. To

be sure, this simplistic approach has not been, and will not be, successful in predicting the finer details and where additional complexities such as chemical reactions occur.

(4) Swirl Velocity Fields

The axial variation of the mean swirl velocity component for the six nonzero-swirl cases (i.e., all cases except cases 5 and 7) considered is seen in Figures 7a through 7f. Since the mean swirl velocity component should vanish on the centerline, the axial variation seen in the figures is not the centerline profile but represents the computed swirl velocity close to the centerline. The swirl velocity is shown normalized with respect to the inflow swirl velocity (W_s) of the inner annular stream. The plots also show the previously discussed centerline variation of CO_2 mass fraction [Paragraph III.1.b(2)] as a frame of reference for the discussion of the swirl-velocity profiles.

The rather small magnitudes of the normalized swirl velocity components ($\leq$ 1% except for case 2) in the vicinity of the centerline should be clear from the figures. The use of a scale factor of 10 or 100 in the ordinates helps one to discern the significant axial variations in the normalized swirl velocity. From the viewpoint of experimental verification, the vicinity of the centerline may not be the optimum location for examining the axial variation of the mean swirl velocity. As will be seen subsequently in our discussion of the radial distributions of the swirl velocity [see Paragraph III.1.c(3)], the predicted profile in the axial direction 2·5 cm radially outward from the centerline will be more helpful in experimental verification. At this location (which corresponds to the radial coordinate of the swirler axis) the magnitudes of the swirl velocity components are much larger. The present discussion, however, does not include such an offcenterline profile.

CASE 1

MASS FLOW RATES: ANNULAR= 1.000KG/S, MID= 0.028KG/S, CENTRAL= 6.000KG/HR

——MASS FRACTION OF CO_2---SWIRL VELOCITY

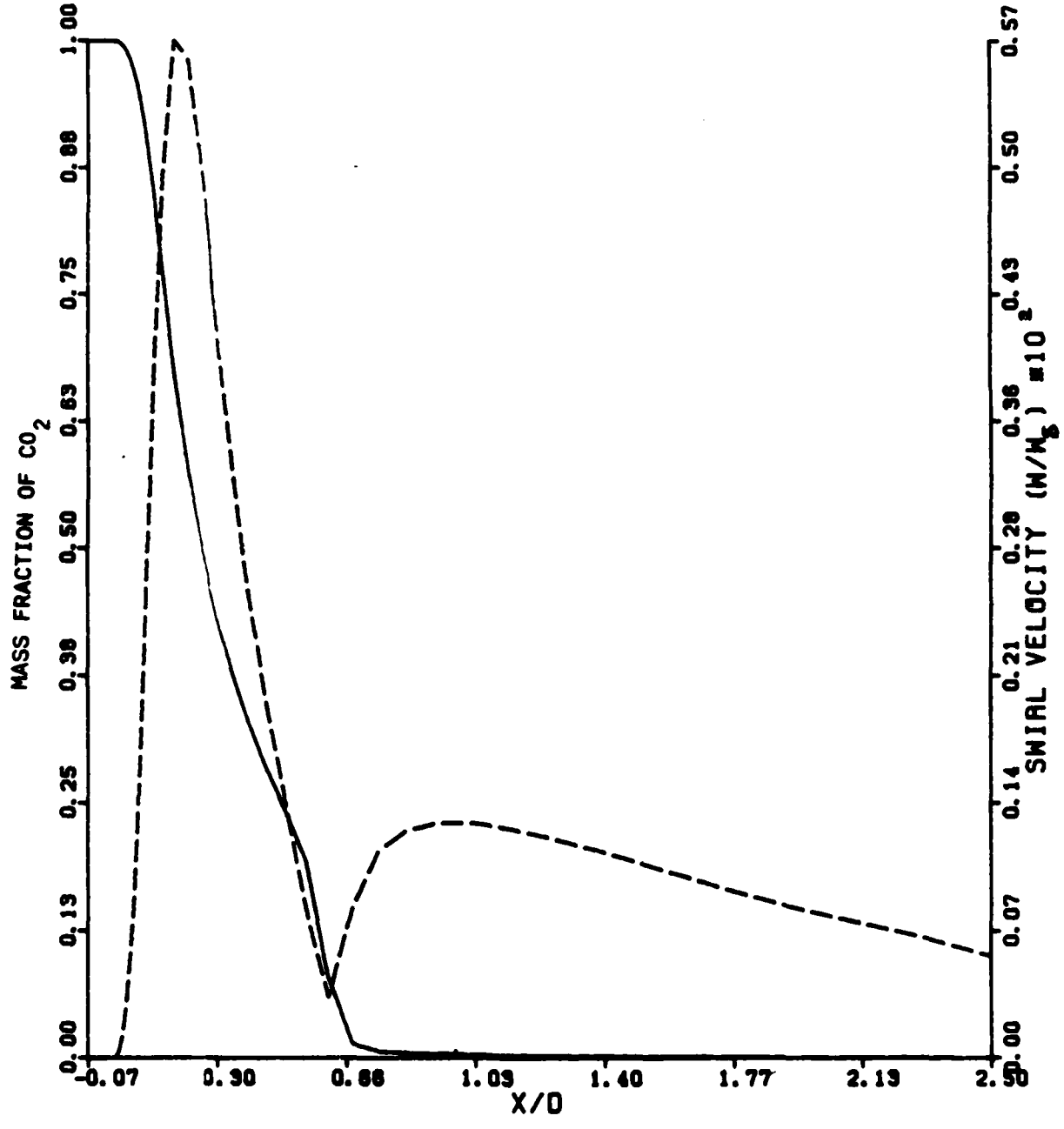

Figure 7(a). Variation of Mean Swirl Velocity.

CASE 2

MASS FLOW RATES: ANNULAR= :.000KG/S, MID= 0.020KG/S, CENTRAL= 12.000KG/HR

——MASS FRACTION OF CO_2---SWIRL VELOCITY

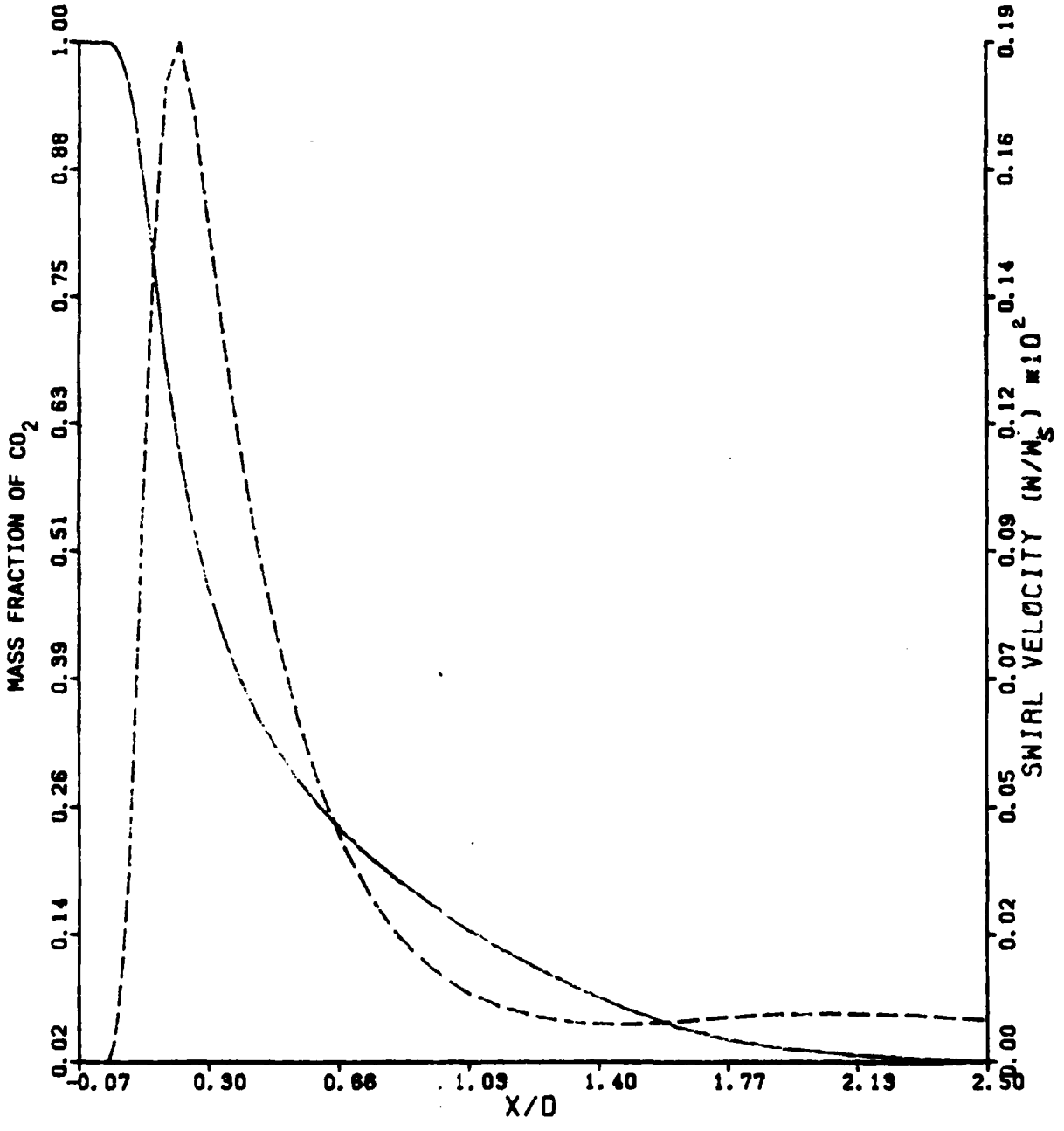

Figure 7(b). Variation of Mean Swirl Velocity.

CASE 3

MASS FLOW RATES: ANNULAR= 1.000KG/S, MID= 0.056KG/S, CENTRAL= 6.000KG/HR

—MASS FRACTION OF CO_2---SWIRL VELOCITY

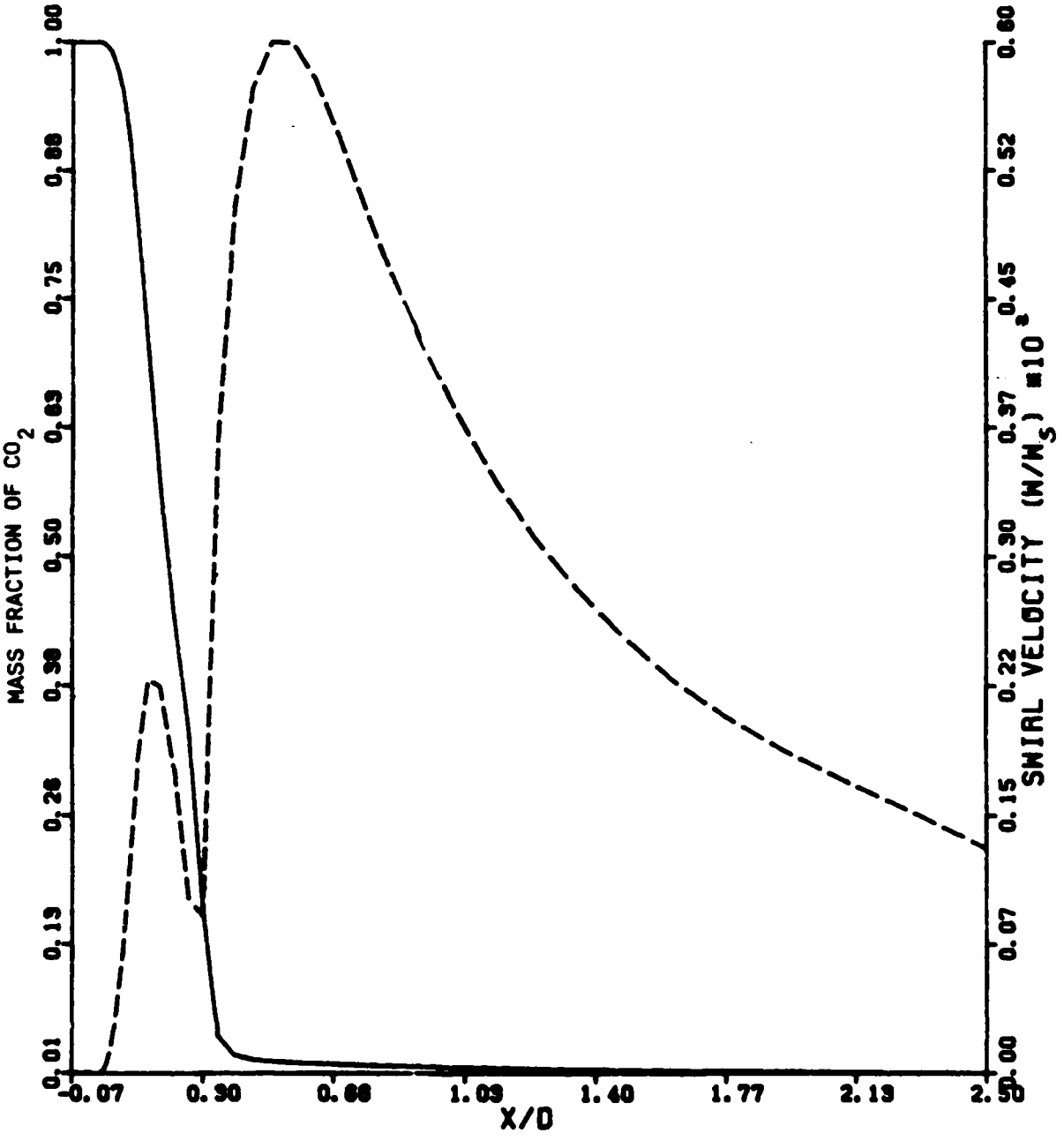

Figure 7(c). Variation of Mean Swirl Velocity.

CASE 4

MASS FLOW RATES: ANNULAR= 1.000KG/S, MID= 0.056KG/S, CENTRAL= 12.000KG/HR

—MASS FRACTION OF CO_2---SWIRL VELOCITY

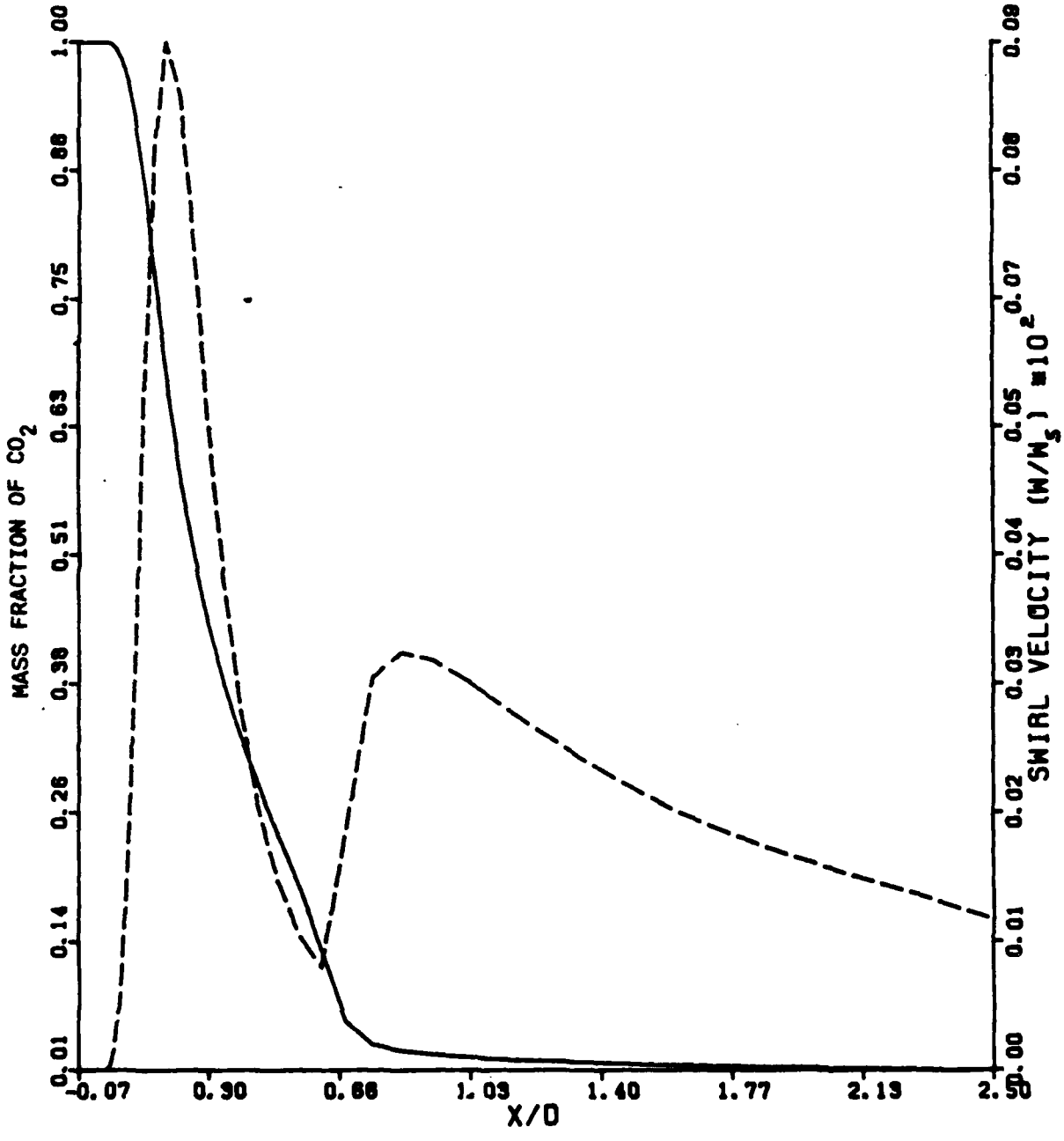

Figure 7(d). Variation of Mean Swirl Velocity.

CASE 6

MASS FLOW RATES: ANNULAR= 0.328KG/S, MID= 0.028KG/S, CENTRAL= 5.760KG/HR

—MASS FRACTION OF CO_2---SWIRL VELOCITY

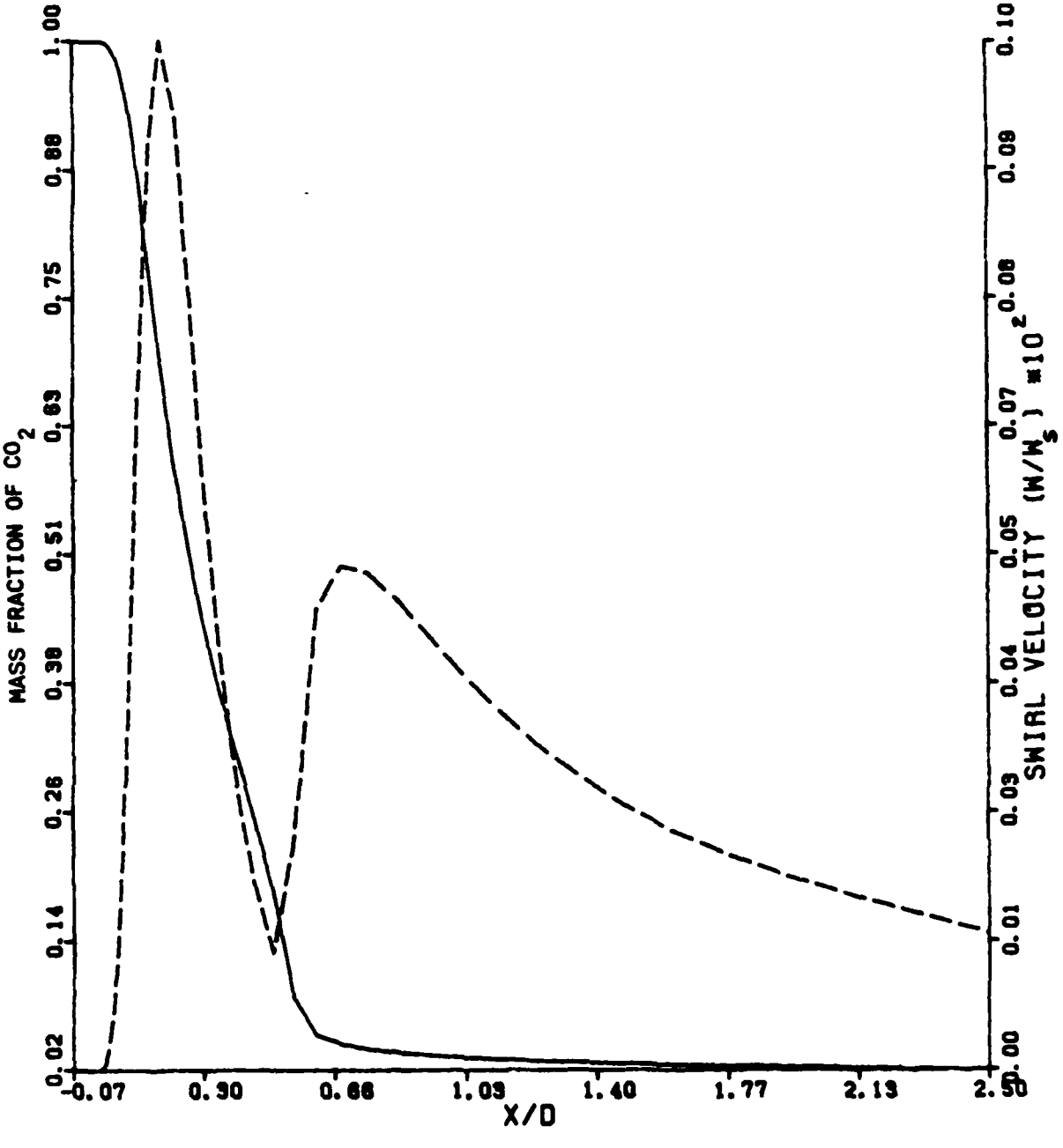

Figure 7(e). Variation of Mean Swirl Velocity.

CASE 8
MASS FLOW RATES: ANNULAR= 2.010KG/S, MID= 0.028KG/S, CENTRAL= 5.760KG/HR

——MASS FRACTION OF CO_2---SWIRL VELOCITY

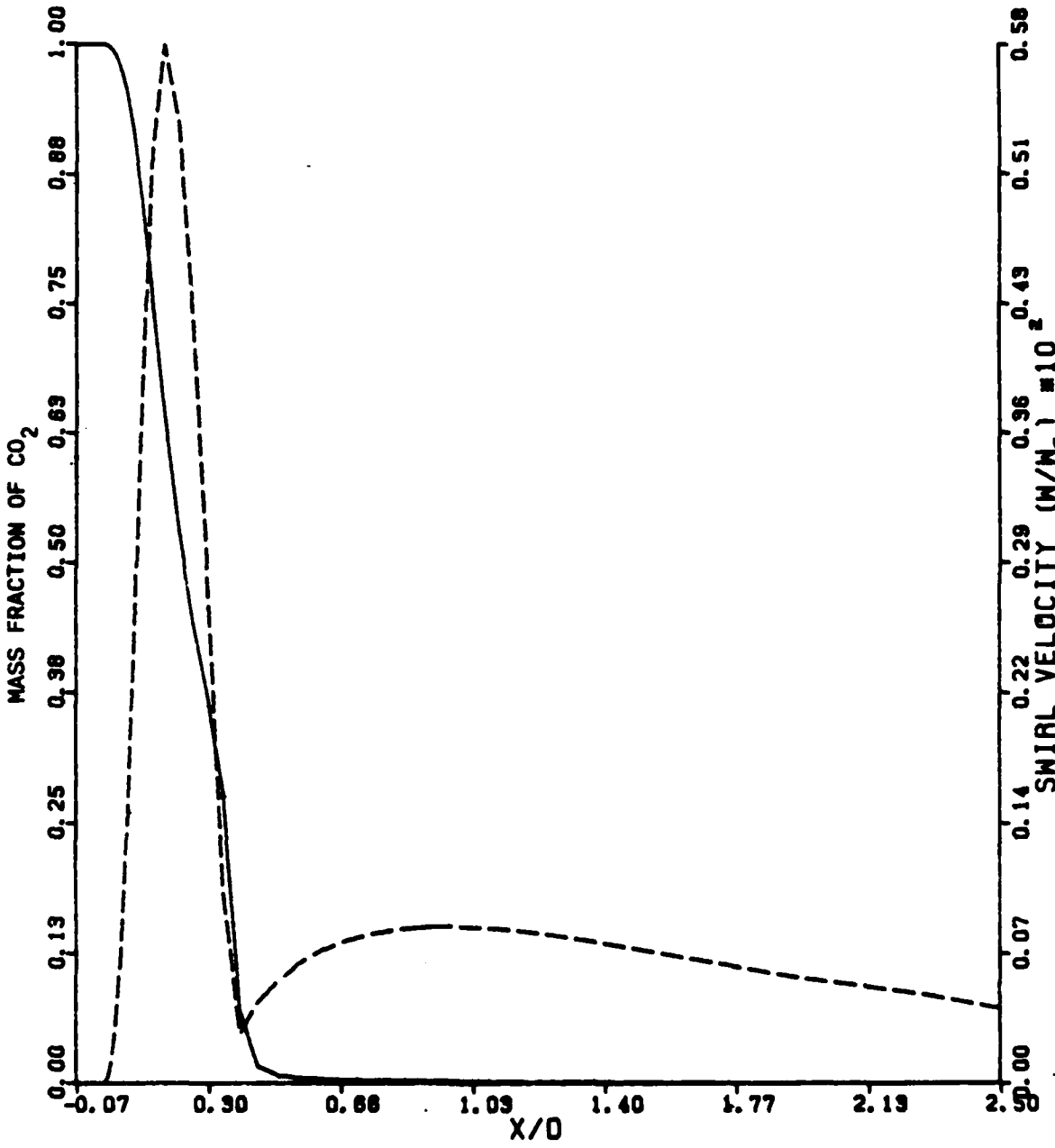

Figure 7(f). Variation of Mean Swirl Velocity.

It is clear that for all six cases the normalized swirl velocity first peaks just downstream of L_f. Subsequently, it falls off sharply to a minimum at a location corresponding to the forward stagnation point (except in Figure 7b of case 2 where the central jet penetrates the recirculation region and eliminates the centerline-flow reversal). There is a sharp rise to a second peak in the swirl velocity beyond the minimum. Farther downstream there is a gradual tapering off towards the exit boundary in all the cases. The magnitude of the second peak relative to the first peak, however, appears to depend on other parameters of the problem (such as m_a, m_s, m_c, S_N, etc.). Thus, in cases 1, 4, 6, and 8 the first peak represents the absolute maximum, while case 3 (see Figure 7c), corresponding to the maximum swirl number 0·85 considered in this study, exhibits the second peak as the absolute maximum (nearly three times as large as the first peak).

A comparison of Figures 7a and 7c shows that the near wake is dominated by the swirling stream when its mass flow rate m_s is doubled. This is evident both from the shift towards the bluff-body face in the locations of the peaks and from the decrease (by more than a factor of 2) in the magnitude of the first peak and the increase (by more than a factor of 4) in the magnitude of the second peak. An increase in the central jet mass flow, with the mass flow rates in the two outer streams kept fixed, diminishes the magnitudes of both peaks in swirl velocity considerably. This is clear from a comparison of Figures 7c and 7d which indicates that the increase in m_c is to counter the influence of the swirling stream. Qualitatively, the trends in Figures 7a and 7d have become similar. This is consistent with the identical value of swirl number (see Table 4) in cases 1 and 4.

One may expect that a decrease in the outer annular mass flow rate (m_a) would produce a result somewhat similar to that of an increase in m_c. This is the case, as shown by a

shown by a comparison of Figures 7a and 7e. There is a significant reduction in the magnitudes of both peaks. The relative increase in the second peak vis-a-vis the first peak is larger, however. Finally, an increase in m_a from 1 to 2 kg/s essentially preserves the trend. This is seen from a comparison of Figures 7a and 7f which indicates that the first peak remains unchanged (both in magnitude and location), whereas the second peak is decreased in magnitude. It is worth noting that the similarity of the trends in cases 1, 4, 6, and 8 is consistent with the nearly identical values of S_N.

c. Radial Distributions

A further examination of the predicted behavior of the POSF combustor flowfields can be made by considering the radial variation of selected flow variables. For this purpose four axial stations were selected (located at 0·1, 0·73, 1·58, and 4·12 cm from the centerbody face) and the radial distributions thereat of the turbulent kinetic energy, temperature, CO_2 mass fraction, and mean swirl velocity were studied. In the plots of the profiles both the axial and radial distances are normalized with respect to the centerbody radius H (= 7 cm). The normalized locations of the radius of the central jet, inner and outer radii of the swirling stream, and the radius of the centerbody are identified by diamond markers shown along the ordinate.

(1) Profiles of Turbulent Kinetic Energy

Figures 8a through 8h show the radial variation of (dimensional) turbulent kinetic energy [expressed in $(m/s)^2$] for the eight test cases. Note that with the assumption of isotropy, these profiles also represent the variation of the square of the rms axial velocity components (magnified by a factor of 3/2).

These profiles show that in all the cases relatively strong local peaks occur in the vicinity of the central-jet

MASS FLOW RATES: ANNULAR= 1.000KG/S, MID= 0.028KG/S, CENTRAL= 8.000KG/HR
CASE 1

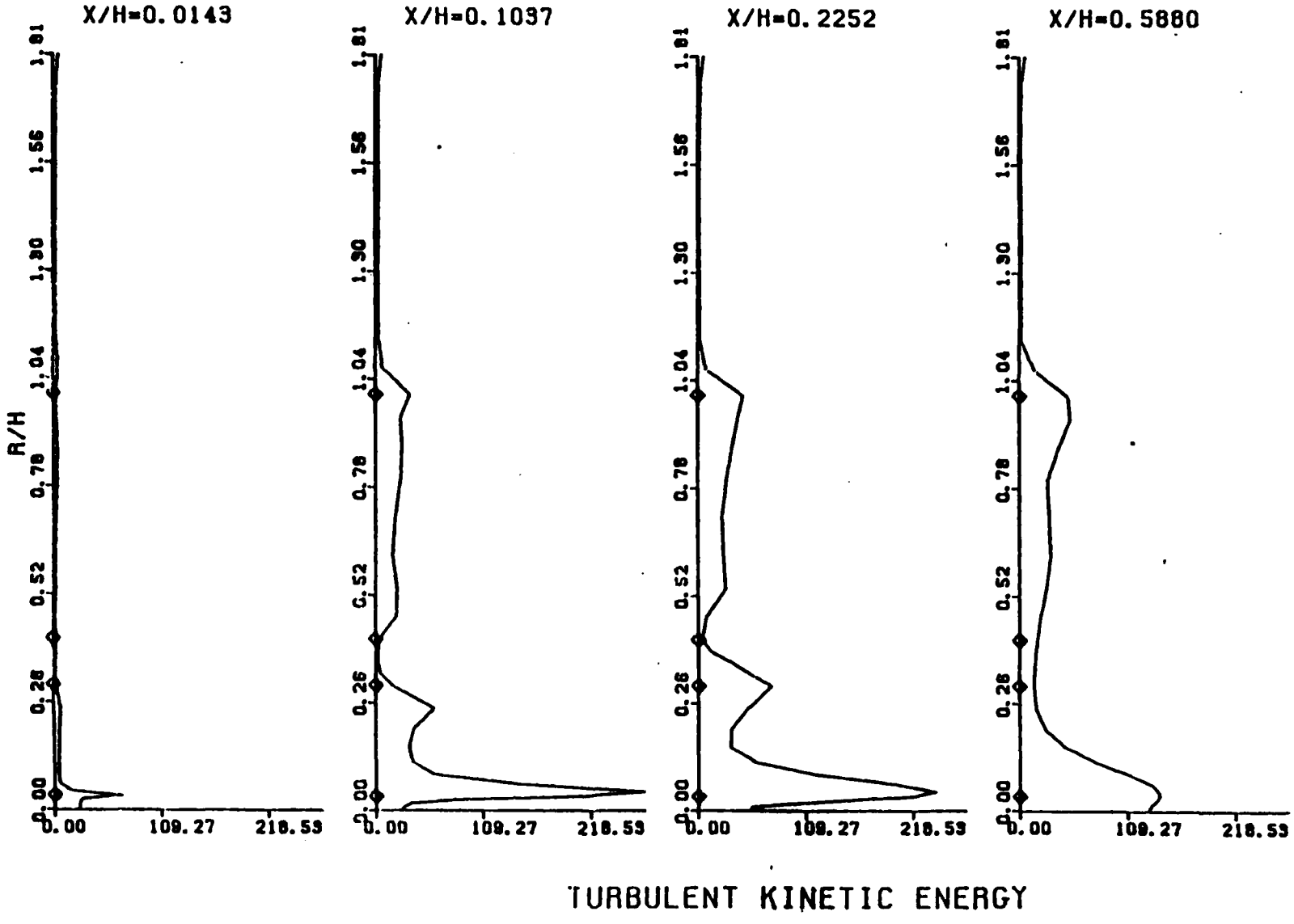

Figure 8(a). Radial Profiles of Turbulent Kinetic Energy.

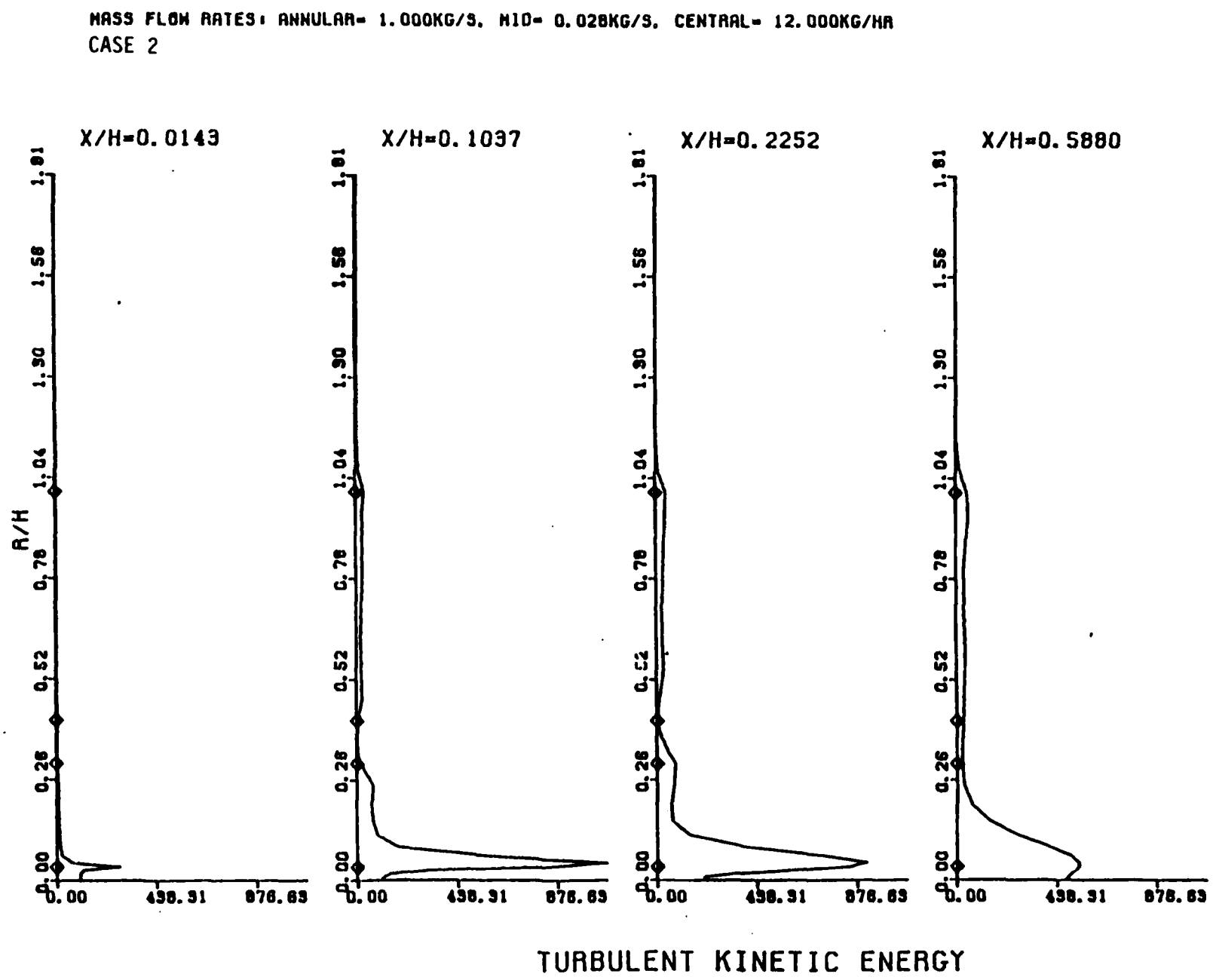

Figure 8(b). Radial Profiles of Turbulent Kinetic Energy.

MASS FLOW RATES: ANNULAR= 1.000KG/S. MID= 0.056KG/S. CENTRAL= 8.000KG/HR
CASE 3

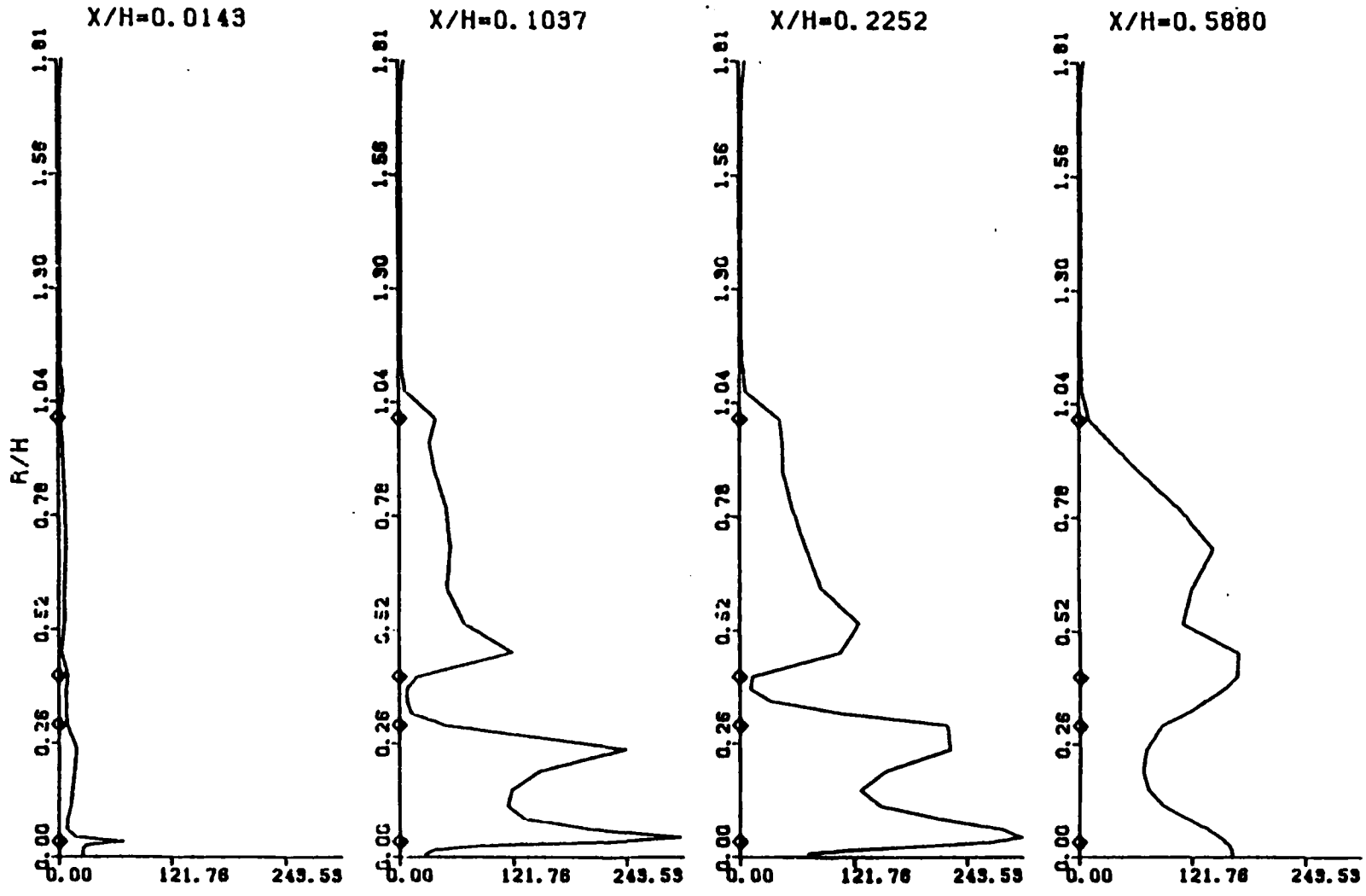

TURBULENT KINETIC ENERGY

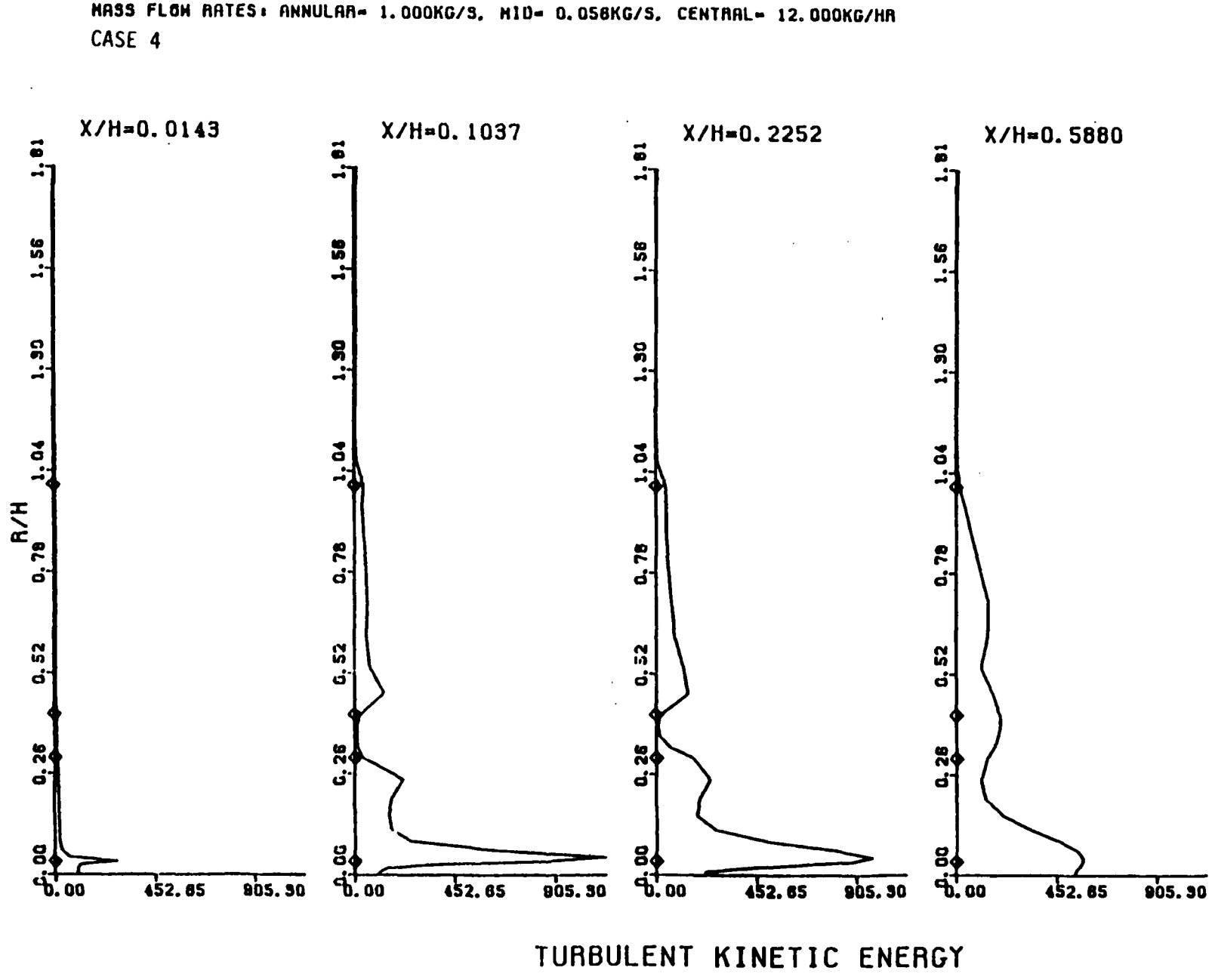

Figure 8(d). Radial Profiles of Turbulent Kinetic Energy.

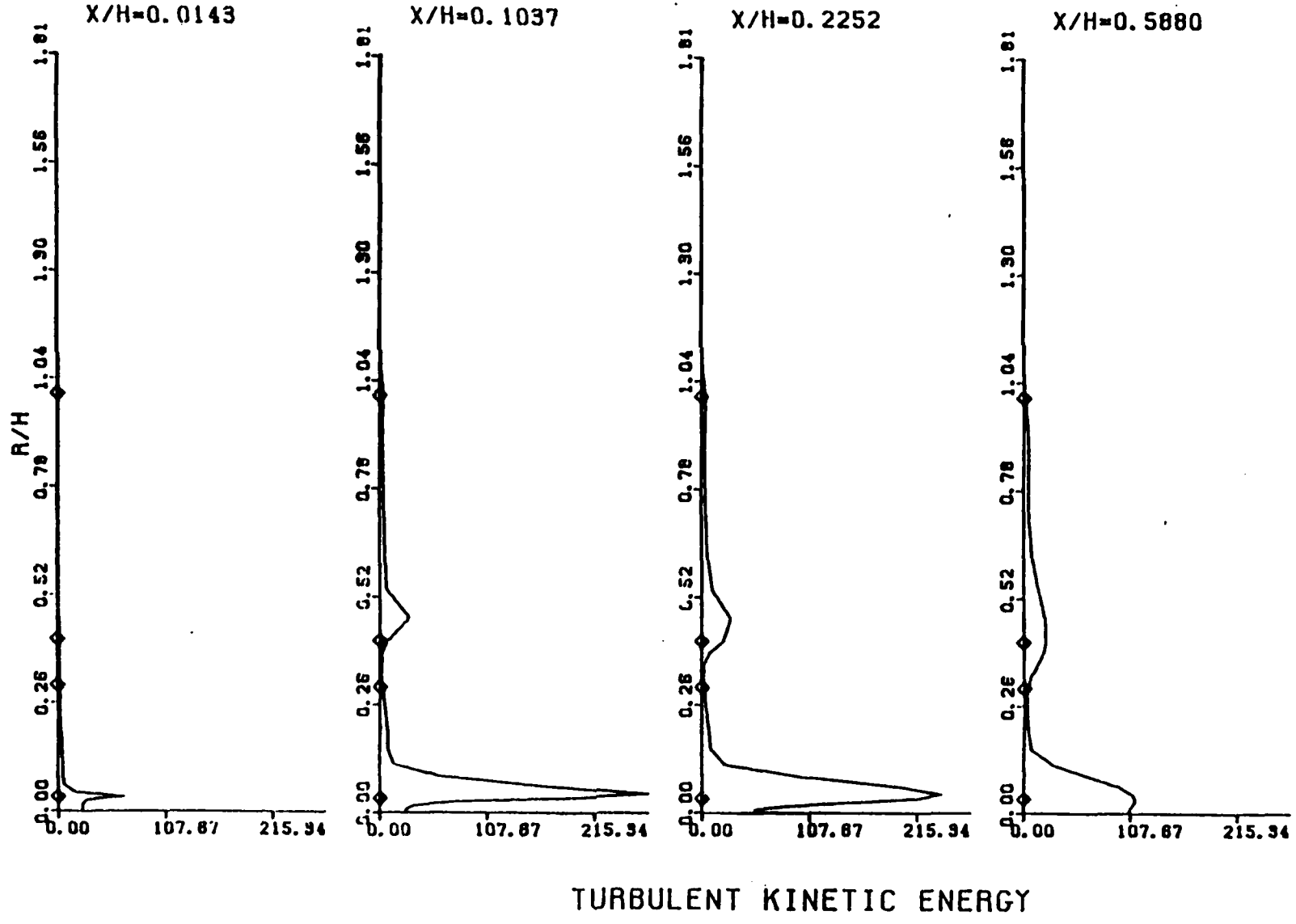

Figure 8(e). Radial Profiles of Turbulent Kinetic Energy.

MASS FLOW RATES: ANNULAR= 0.928KG/S, MID= 0.028KG/S, CENTRAL= 5.780KG/HR
CASE 6

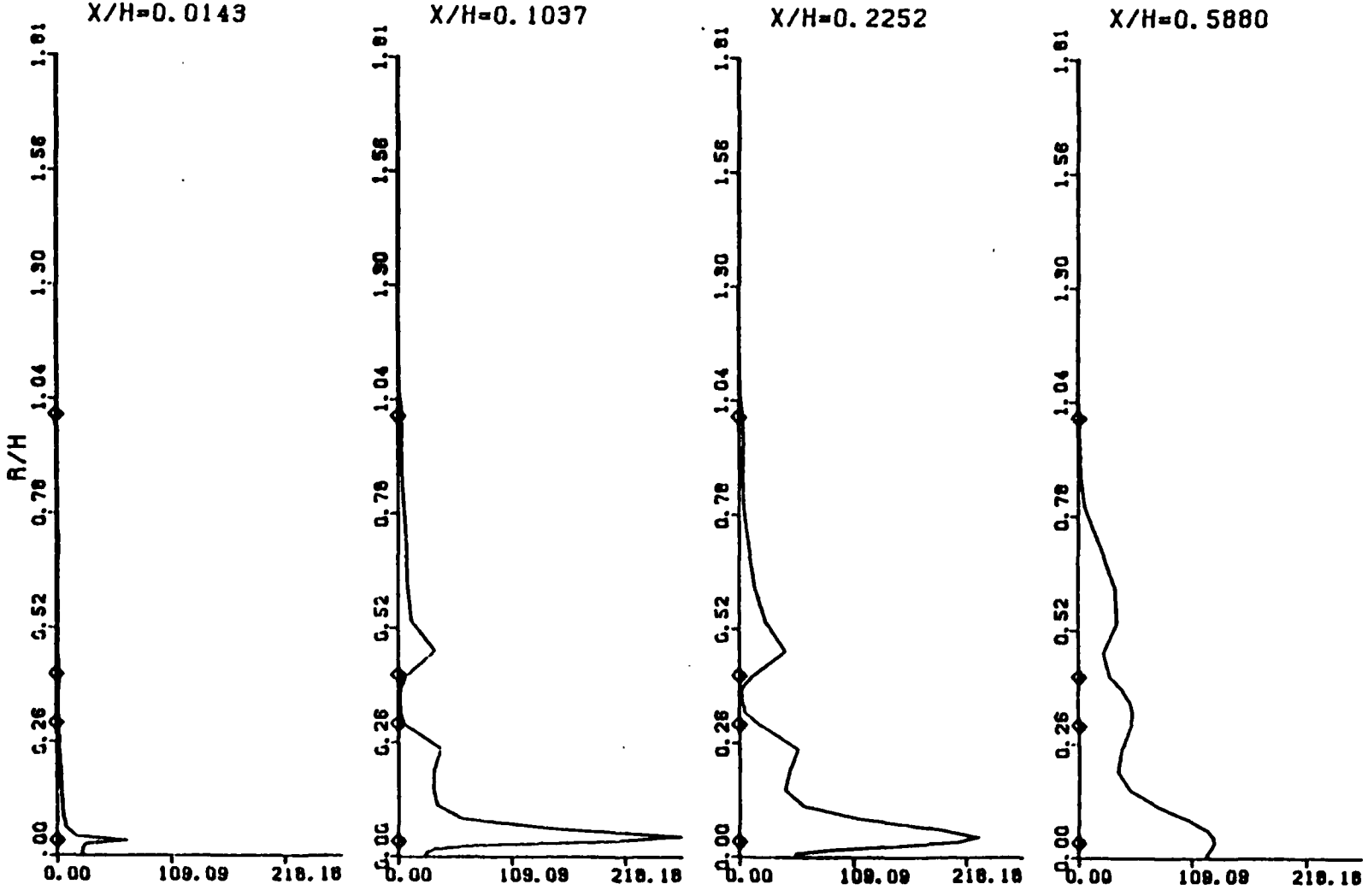

Figure 8(f). Radial Profiles of Turbulent Kinetic Energy.

MASS FLOW RATES: ANNULAR= 2.010KG/S, MID= 0.028KG/S, CENTRAL= 5.760KG/HR
CASE 7

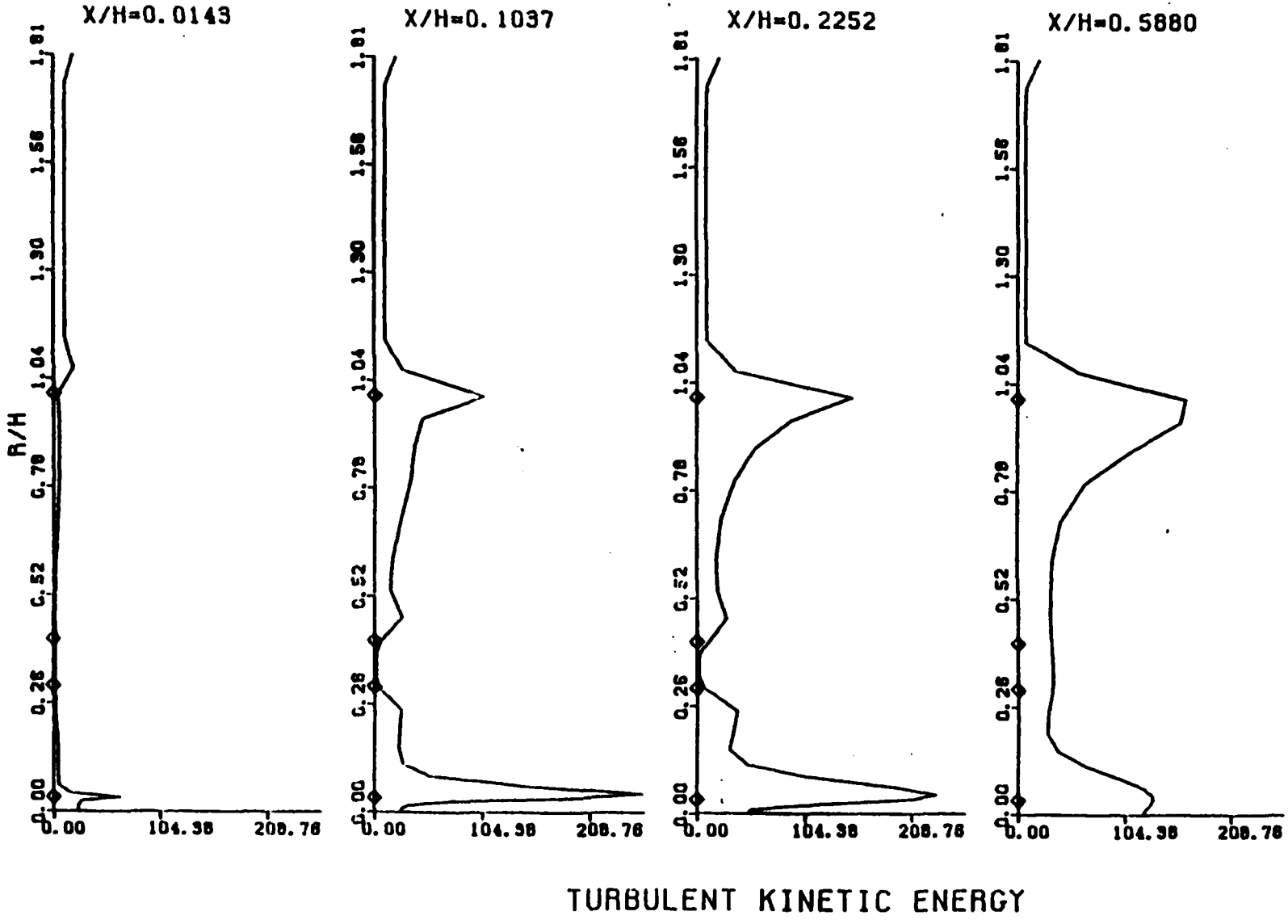

Figure 8(g). Radial Profiles of Turbulent Kinetic Energy.

MASS FLOW RATES: ANNULAR= 2.010KG/S, M10= 0.028KG/S, CENTRAL= 5.760KG/HR
CASE 8

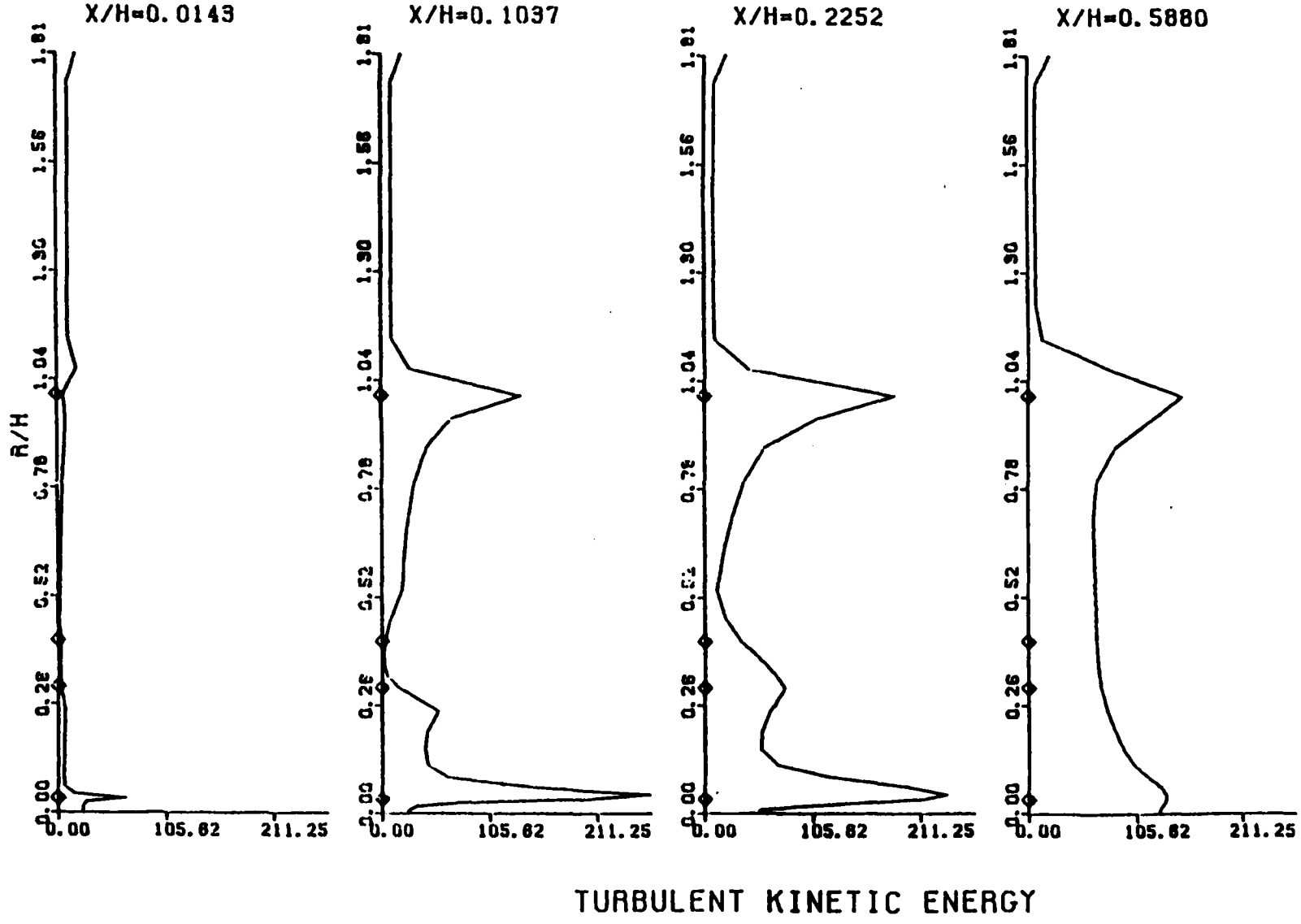

Figure 8(h). Radial Profiles of Turbulent Kinetic Energy.

radius. This signifies the development of the central jet. Previous LDA measurements (Reference 10) of the development of the central jet in a weak annular flow also observed similar trends. The local peaks in the shear layers of the inner and outer streams, on the other hand, do not exhibit a relative dominance, unless the flowfields are characterized by increased strength of these streams. Thus, Figure 8c (corresponding to case 3) shows the greatly enhanced turbulence activity in the shear layers of the swirling stream. As discussed in Paragraph III.1.a(1), case 3 is an example of the flowfield dominated by the swirling stream (recall that in case 3, m_s is twice that of case 1 and the swirl number is the highest). An integrated perspective of the increased turbulent mixing in the near wake is available by inspecting Figures 3c and 8c.

The relative dominance by the outer annular stream is noticeable in Figures 8g and 8h (which correspond to cases 7 and 8 with m_a = 2 kg/s) which show the increasing peak of turbulent kinetic energy in the outer shear layer (at approximately one radius of the centerbody). Finally, the effect of swirl in the flowfield can be understood by comparing Figures 8f and 8h with Figures 8e and 8g (swirl-free cases) respectively. The introduction of swirl serves to increase the turbulence activity in the vicinity of the middle stream.

It is of interest to compare these results with respect to the predictions in the old centerbody configuration (Reference 3). The radial distribution of the turbulent kinetic energy for 2 kg/s annular flow and zero central flow (seen in Figure 29 of Reference 3) shows trends similar to those in Figure 8g. The comparison, however, of the predicted and measured radial distributions of the rms axial velocity field in a small-scale combustor (seen in Figure 19 of Reference 3) suggests that in the case of present predictions also, the quantitative comparison with measurements (when they are available) is likely to be poor [see Paragraph III.1.b(3b)].

(2) Temperature Profiles

Figures 9a through 9h show the radial variation of the (dimensional) temperature field at four axial stations. With our choice of the initial temperatures of 400°K for the central jet and 293°K for the two annular streams and with the rather small mass-flow rate m_c, it should not be surprising that the temperature profiles indicate only a very small spatial extent of the temperature rise above the ambient. Such dramatic effects as seen for the velocity fields (e.g., cases 3, 7, and 8) are not discernible for the temperature field. Perhaps much hotter central jet, or an increase in the temperature of the swirling stream could show more interesting characteristics of the temperature field as it is affected by the different parameters of the problem.

(3) Profiles of CO_2 Mass Fraction and Swirl Velocity

The discussion of the radial distributions is concluded with the consideration here of the profiles of the CO_2 mass fraction and the mean swirl velocity fields. These are seen in Figures 10a through 10f. The four axial stations considered here represent locations much farther downstream (by a factor of 5 to 10) than those seen earlier for the profiles of temperature and kinetic energy. The present choice is dictated more by the increased penetration of the flowfield by the mean swirl velocity component in both axial and radial directions. In the figures the CO_2 mass fraction profiles correspond to those that are essentially confined to small values of the ordinate. Note, however, that the CO_2 mass fraction profiles will be identical to the temperature [normalized as in Paragraph III.1.b(2)] profiles seen in Figures 9a through 9h (as observed previously in Figures 6a through 6h). Therefore, attention in the present discussion is essentially directed to an examination of the swirl velocity profiles.

CASE 1
MASS FLOW RATES: ANNULAR= 1.000KG/S, MID= 0.028KG/S, CENTRAL= 6.000KG/HR

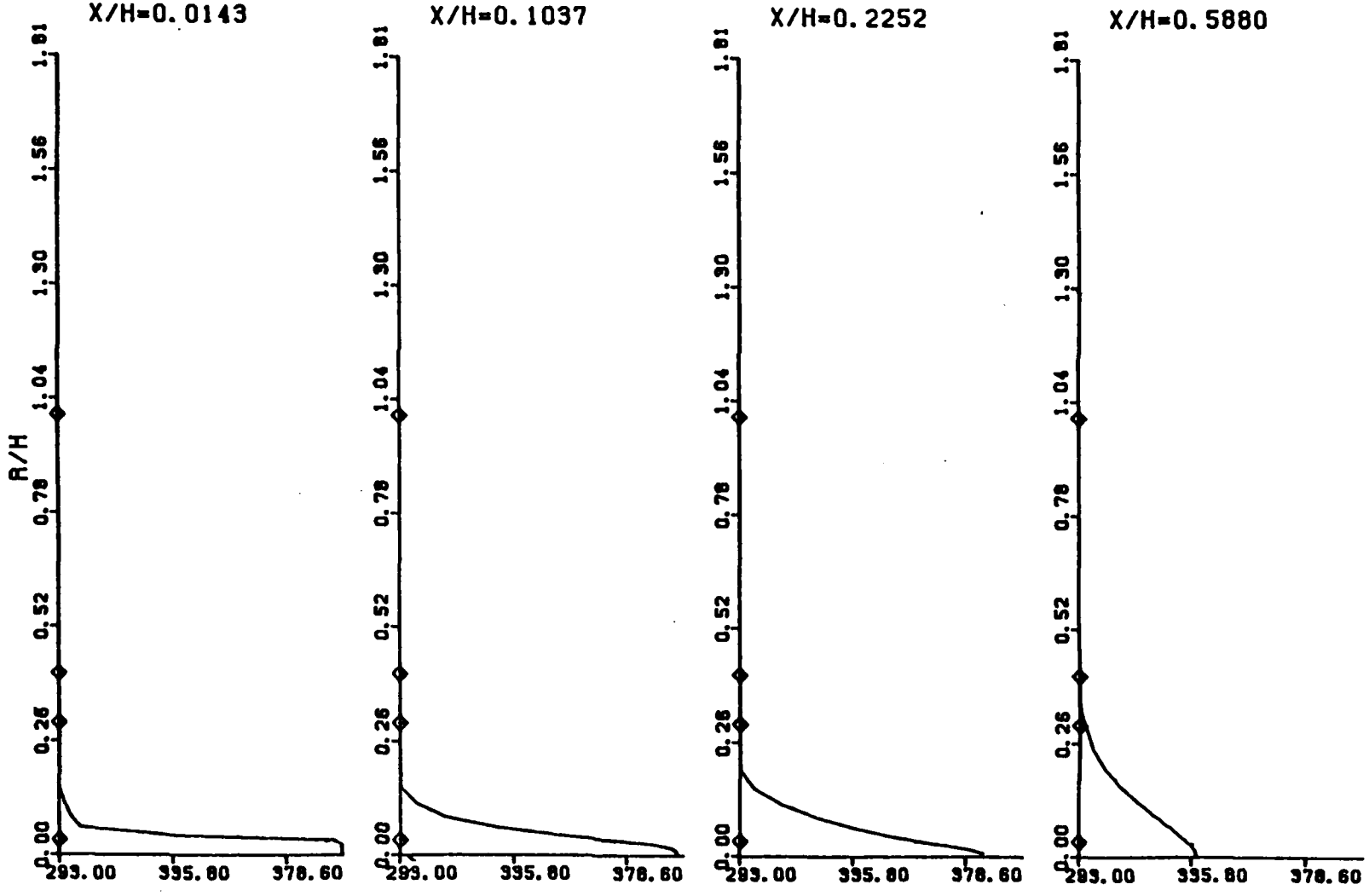

TEMP. PROFILE

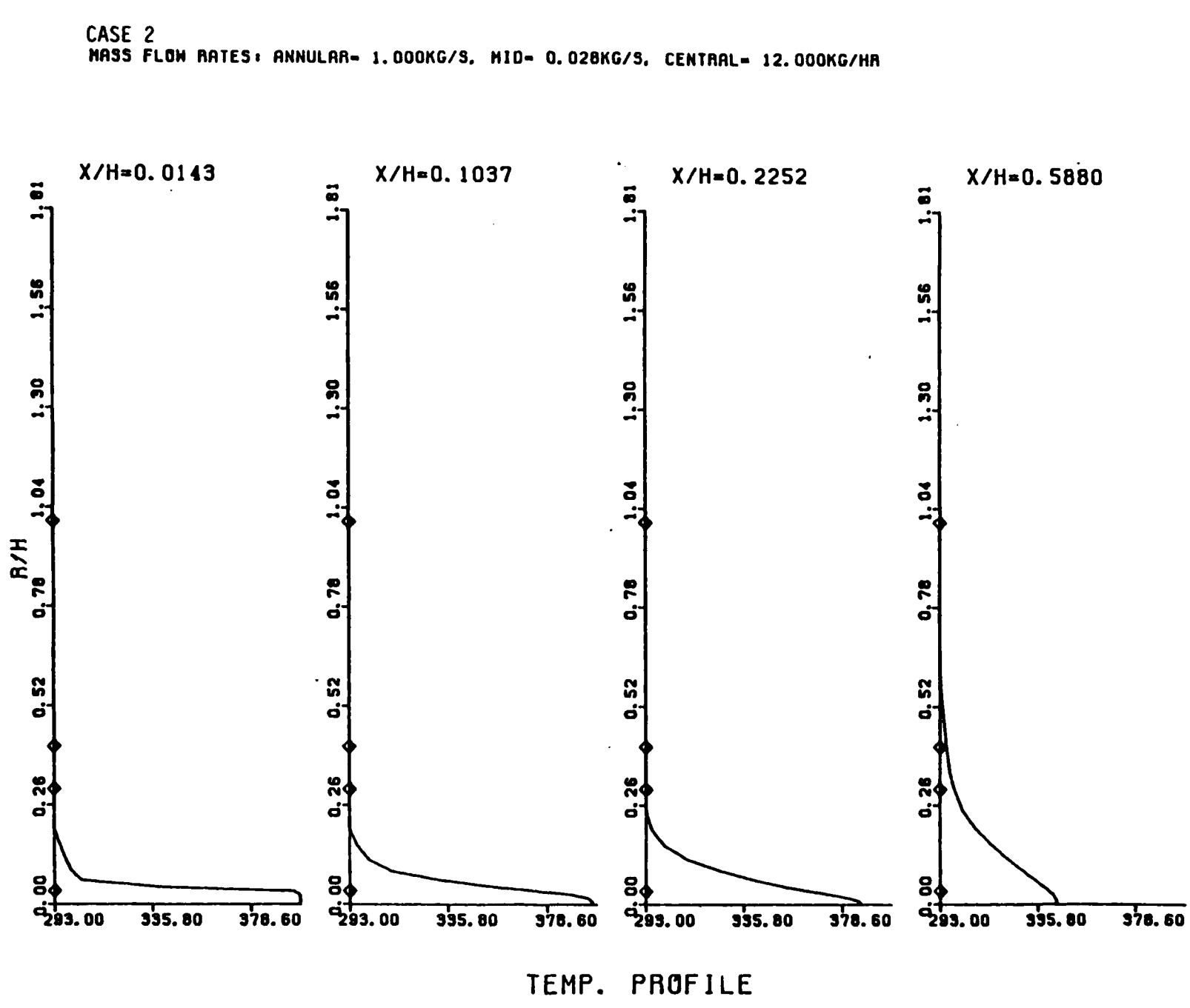

Figure 9(b). Radial Profiles of Temperature.

CASE 3
MASS FLOW RATES: ANNULAR= 1.000KG/S, MID= 0.058KG/S, CENTRAL= 6.000KG/HR

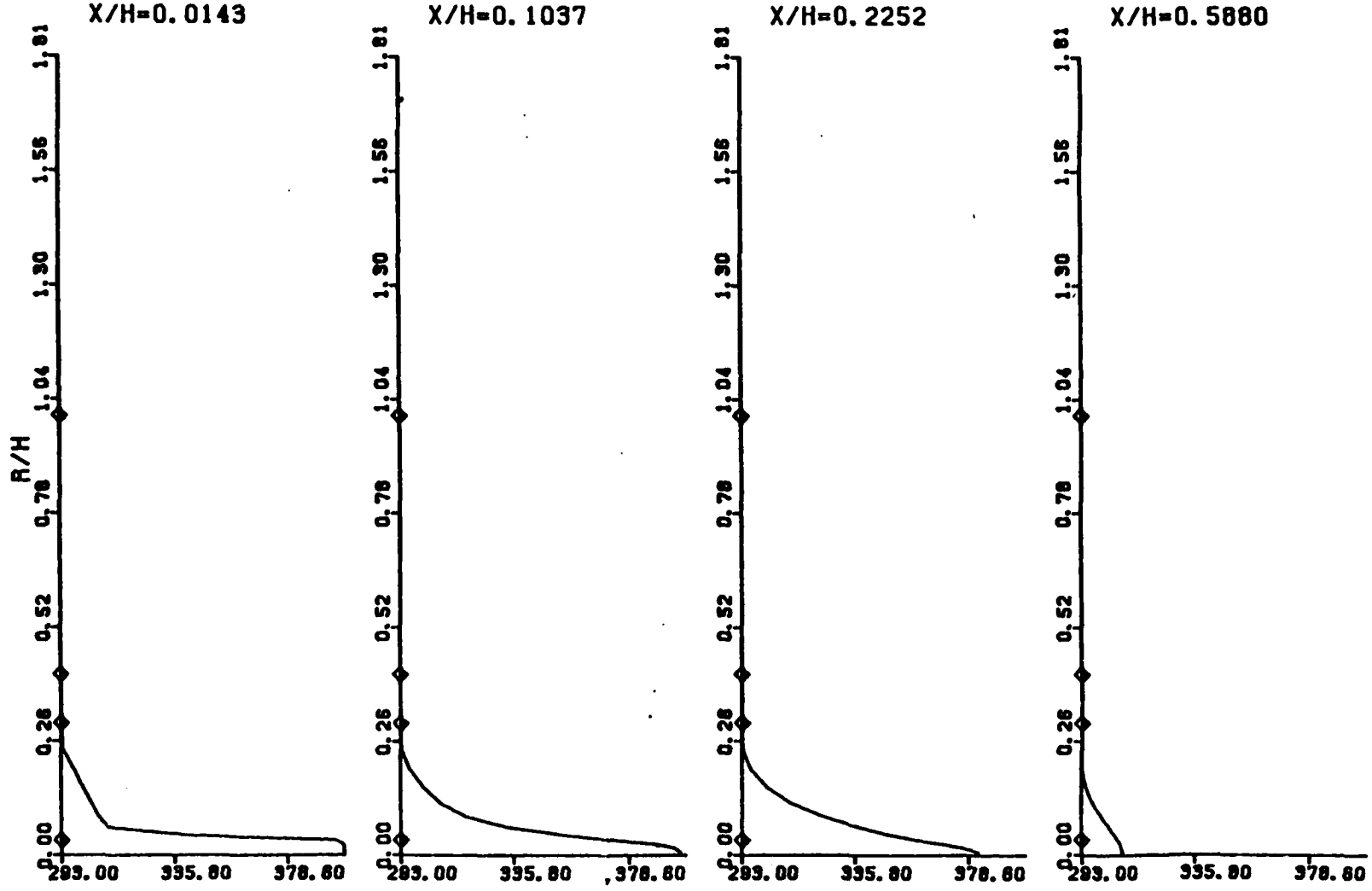

Figure 9(c). Radial Profiles of Temperature.

CASE 4

MASS FLOW RATES: ANNULAR= 1.000KG/S, MID= 0.056KG/S, CENTRAL= 12.000KG/HR

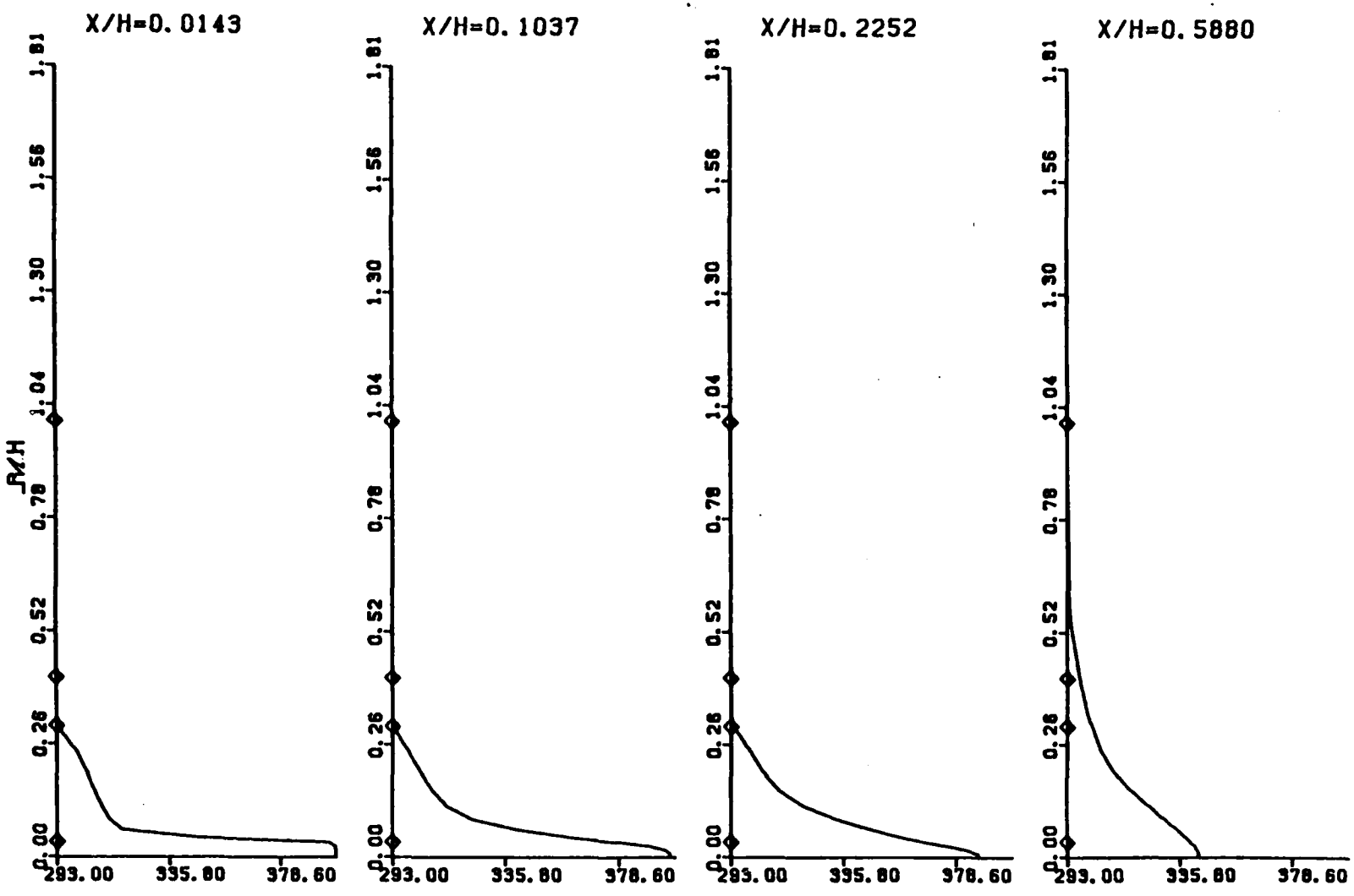

Figure 9(d). Radial Profiles of Temperature.

CASE 5

MASS FLOW RATES: ANNULAR= 0.328KG/S, MID= 0.028KG/S, CENTRAL= 5.760KG/HR

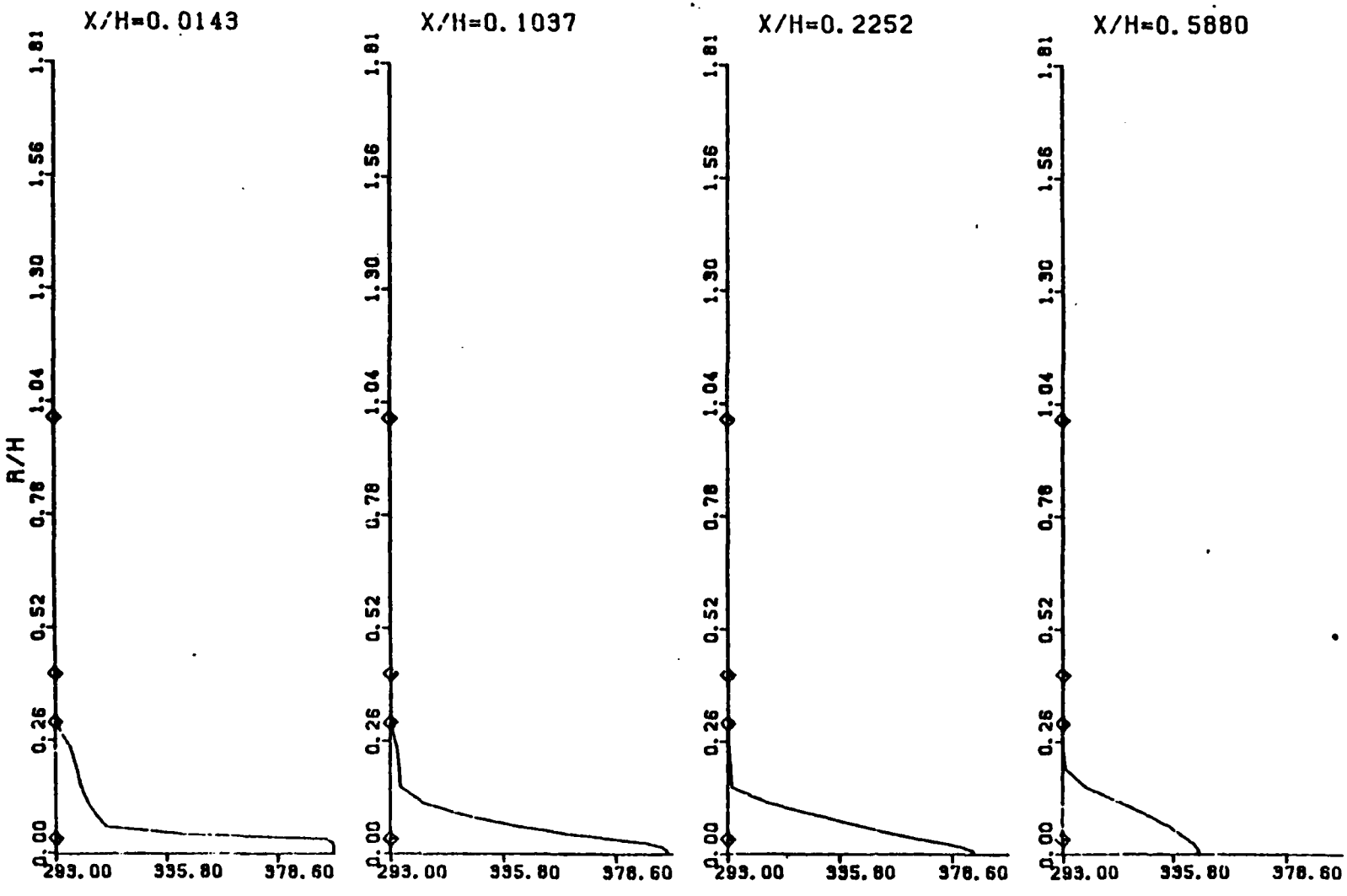

TEMP. PROFILE

CASE 6

MASS FLOW RATES: ANNULAR= 0.928KG/S. MID= 0.028KG/S. CENTRAL= 5.760KG/HR

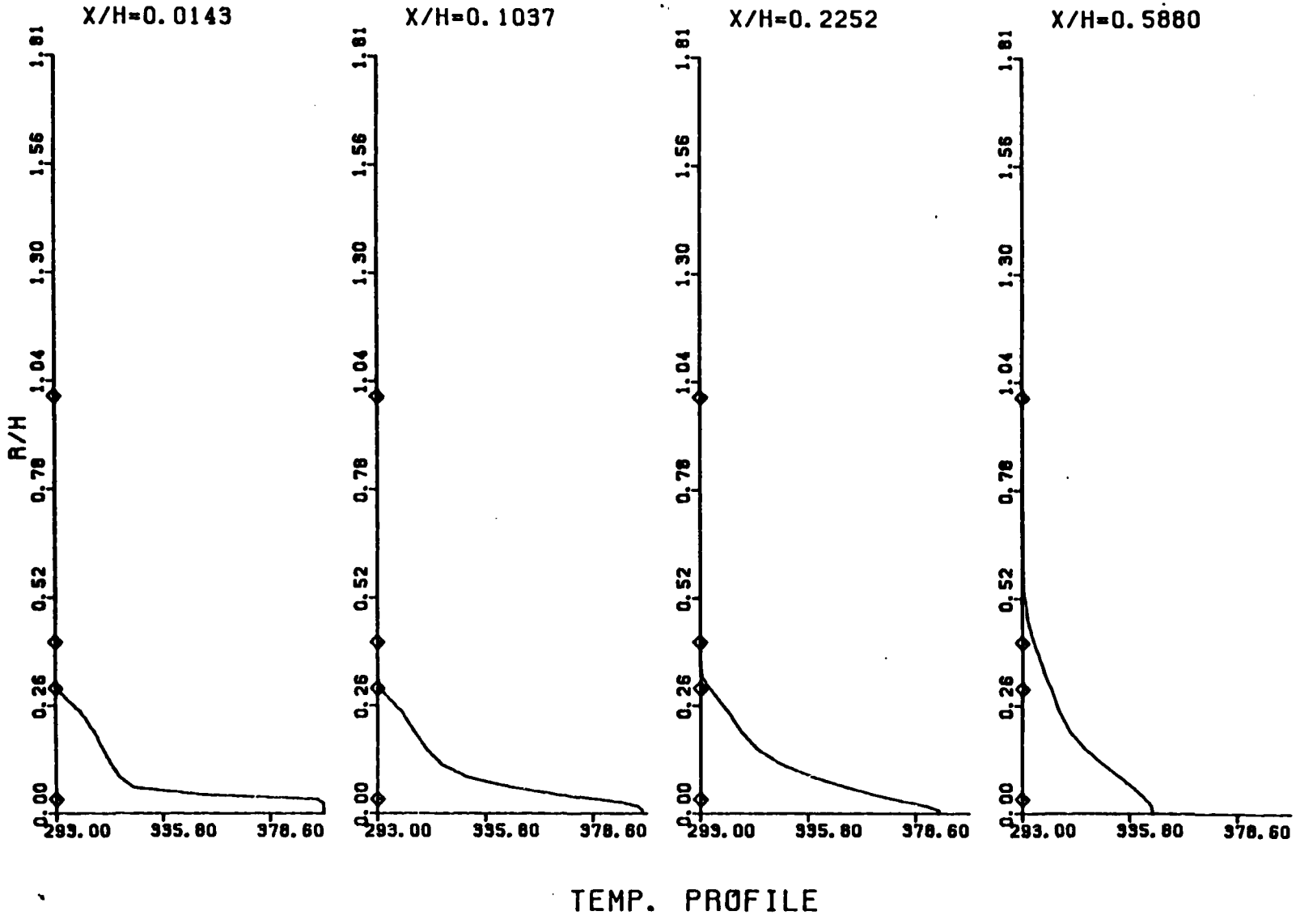

Figure 9(f). Radial Profiles of Temperature.

CASE 7
MASS FLOW RATES: ANNULAR= 2.010KG/S, MID= 0.028KG/S, CENTRAL= 5.760KG/HR

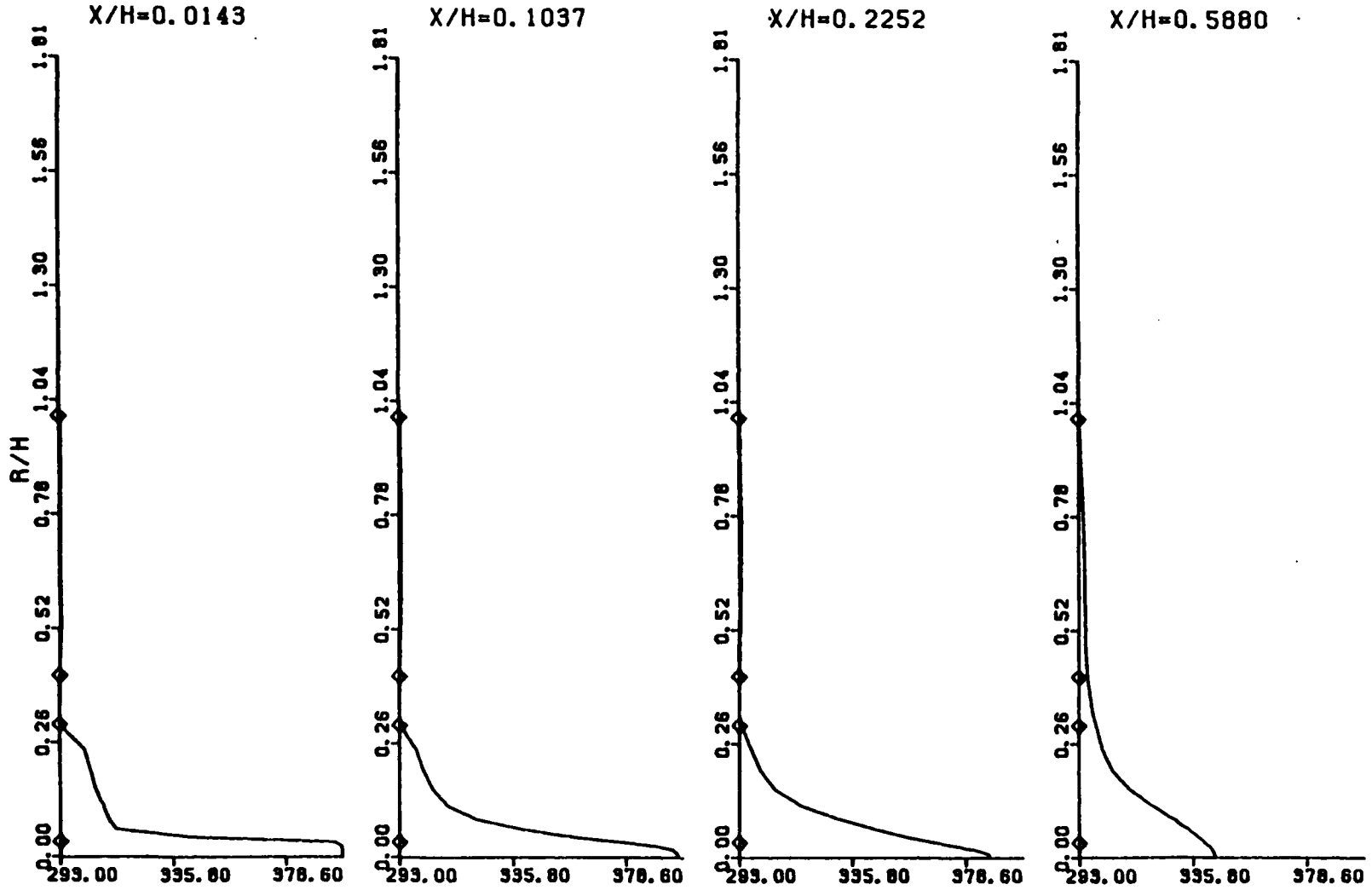

Figure 9(a). Radial Profiles of Temperature.

CASE 8

MASS FLOW RATES: ANNULAR= 2.010KG/S, MID= 0.028KG/S, CENTRAL= 5.760KG/HR

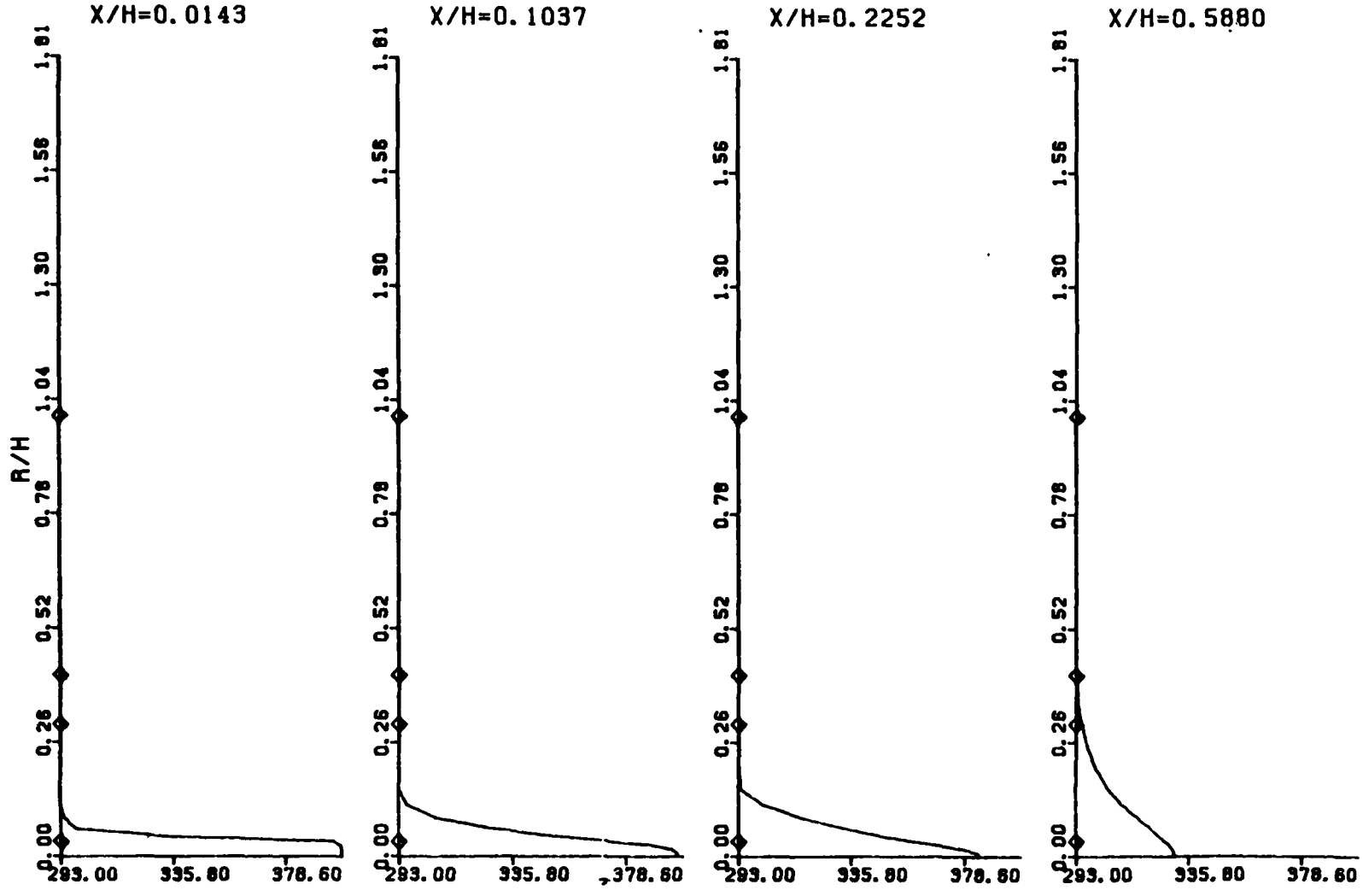

Figure 9(h). Radial Profiles of Temperature.

CASE 1
MASS FLOW RATES: ANNULAR= 1.000KG/S, MID= 0.028KG/S, CENTRAL= 6.000KG/HR

_ _ _ X/H=0.0514, . . . X/H=0.2252, ___ X/H=1.0951, _ . _ X/H=4.5887,

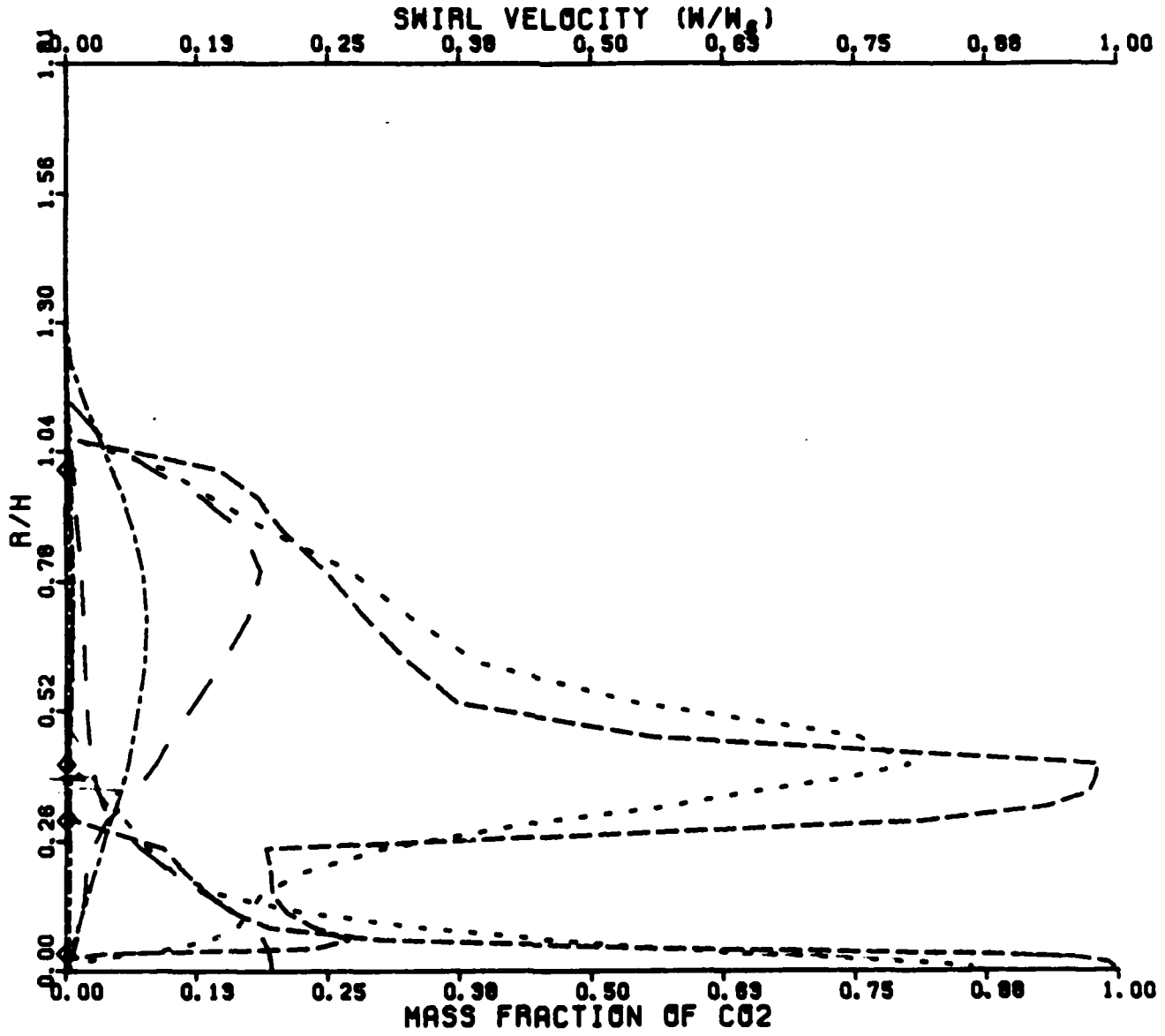

Figure 10(a). Radial Profiles of CO_2 Mass Fraction and Swirl Velocity.

CASE 2

MASS FLOW RATES: ANNULAR= 1.000KG/S, MID= 0.028KG/S, CENTRAL= 12.000KG/HR

_ _ _ X/H=0.0514, . . . X/H=0.2252, ___ X/H=1.0951, _ . _ X/H=4.5887,

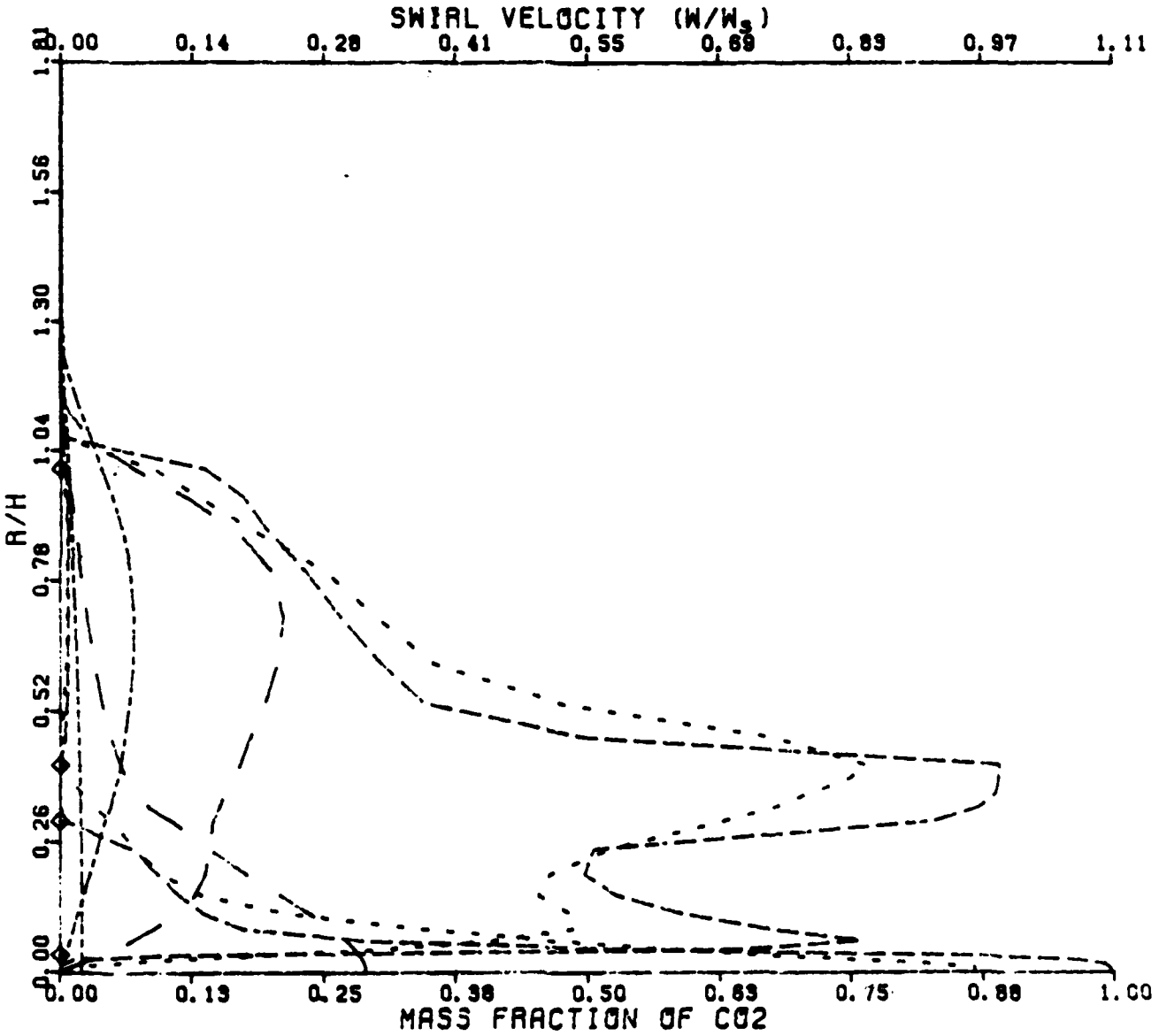

Figure 10(b). Radial Profiles of CO_2 Mass Fraction and Swirl Velocity.

AD-A171 169 COMPUTATIONAL FLUID DYNAMIC STUDIES OF CERTAIN DUCTED BLUFF-BODY FLOWFIEL (U) DAYTON UNIV OH RESEARCH INST M S RAJU ET AL JUL 86 UDR-TR-5-83-VOL-2 2/2

UNCLASSIFIED AFWAL-TR-86-2004-VOL-2 F33615-84-C-2411 F/G 21/2 NL

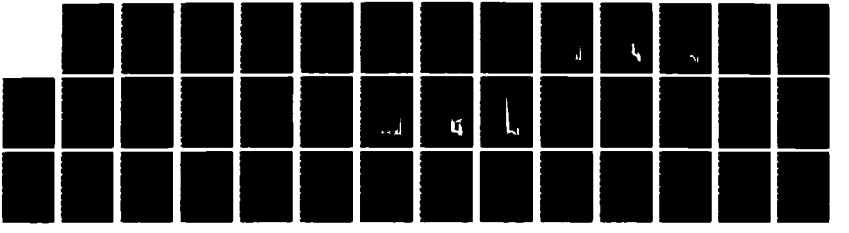

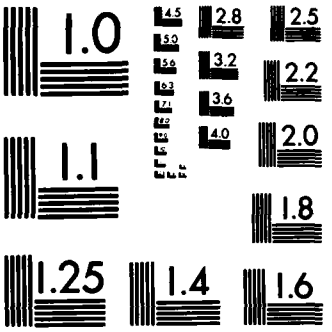

ICROCOPY RESOLUTION TEST CHART
NATIONAL BUREAU OF STANDARDS-1963-A

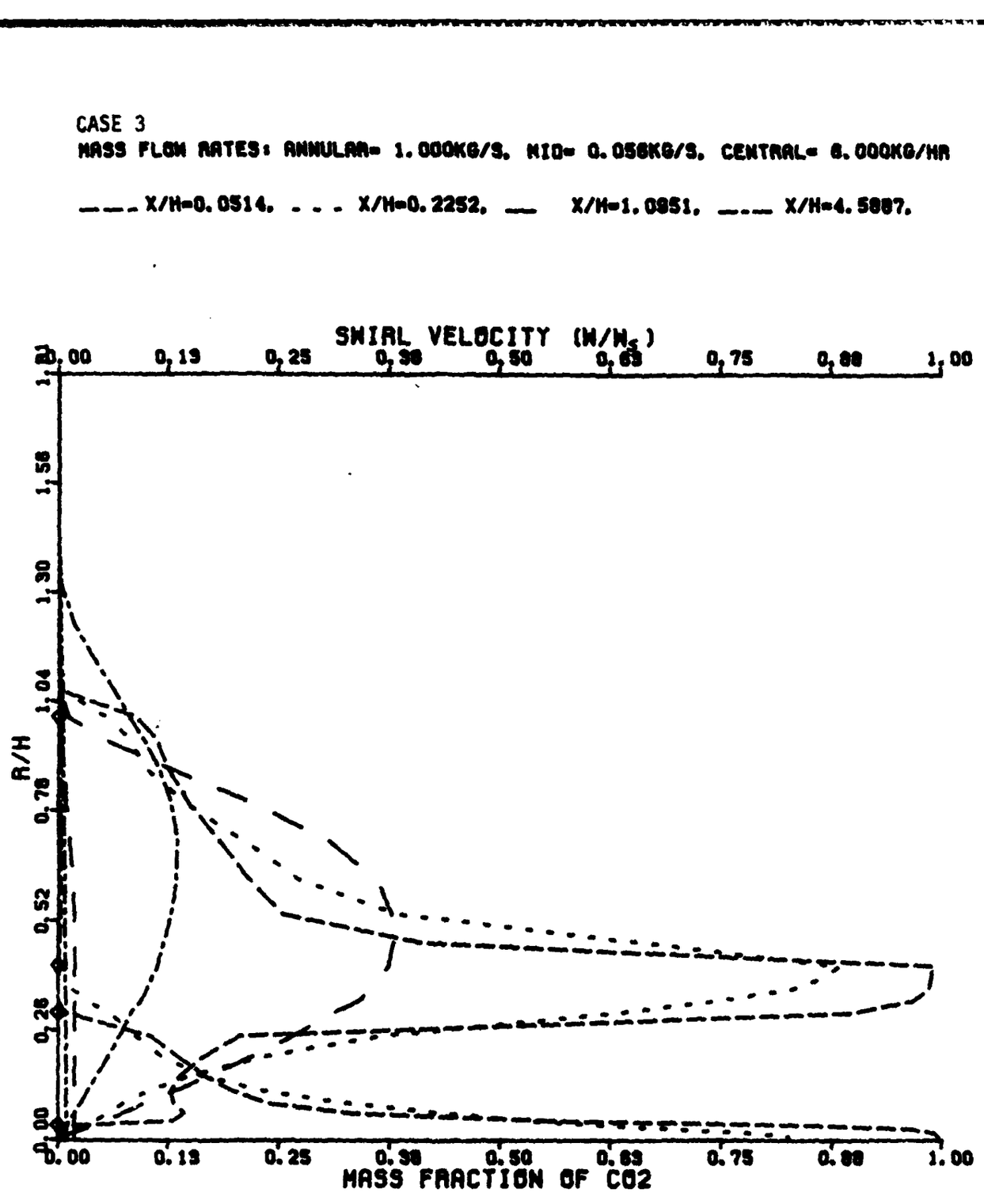

Figure 10(c). Radial Profiles of CO_2 Mass Fraction and Swirl Velocity.

CASE 4
MASS FLOW RATES: ANNULAR= 1.000KG/S, MID= 0.058KG/S, CENTRAL= 12.000KG/HR

____ X/H=0.0514, . . . X/H=0.2252, ___ X/H=1.0951, ____ X/H=4.5887,

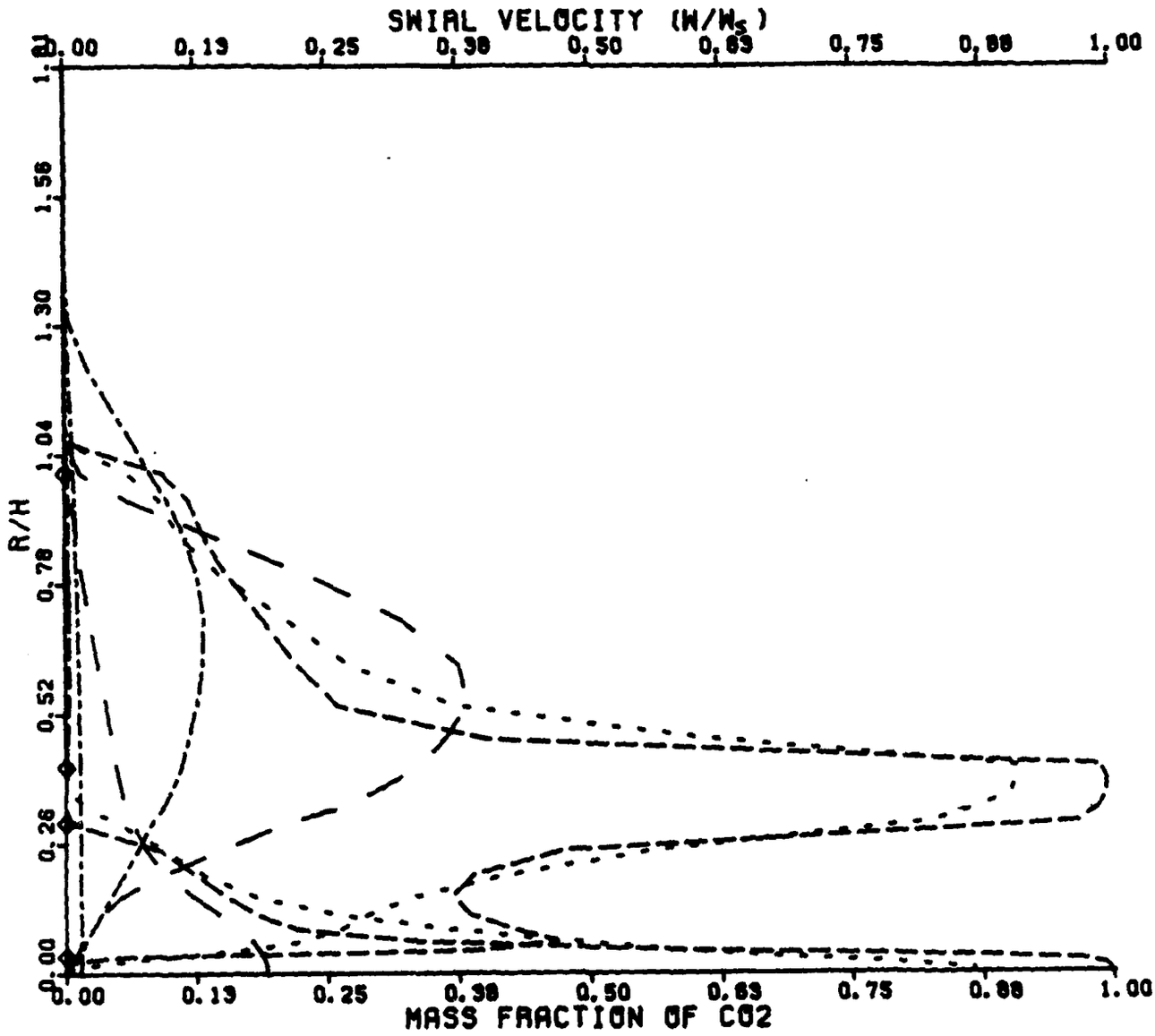

Figure 10(d). Radial Profiles of CO_2 Mass Fraction and Swirl Velocity.

CASE 6
MASS FLOW RATES: ANNULAR= 0.328KG/S, MID= 0.028KG/S, CENTRAL= 5.760KG/HR

_ _ _ X/H=0.0514, . . . X/H=0.2252, __ X/H=1.0951, _ . _ X/H=4.5887,

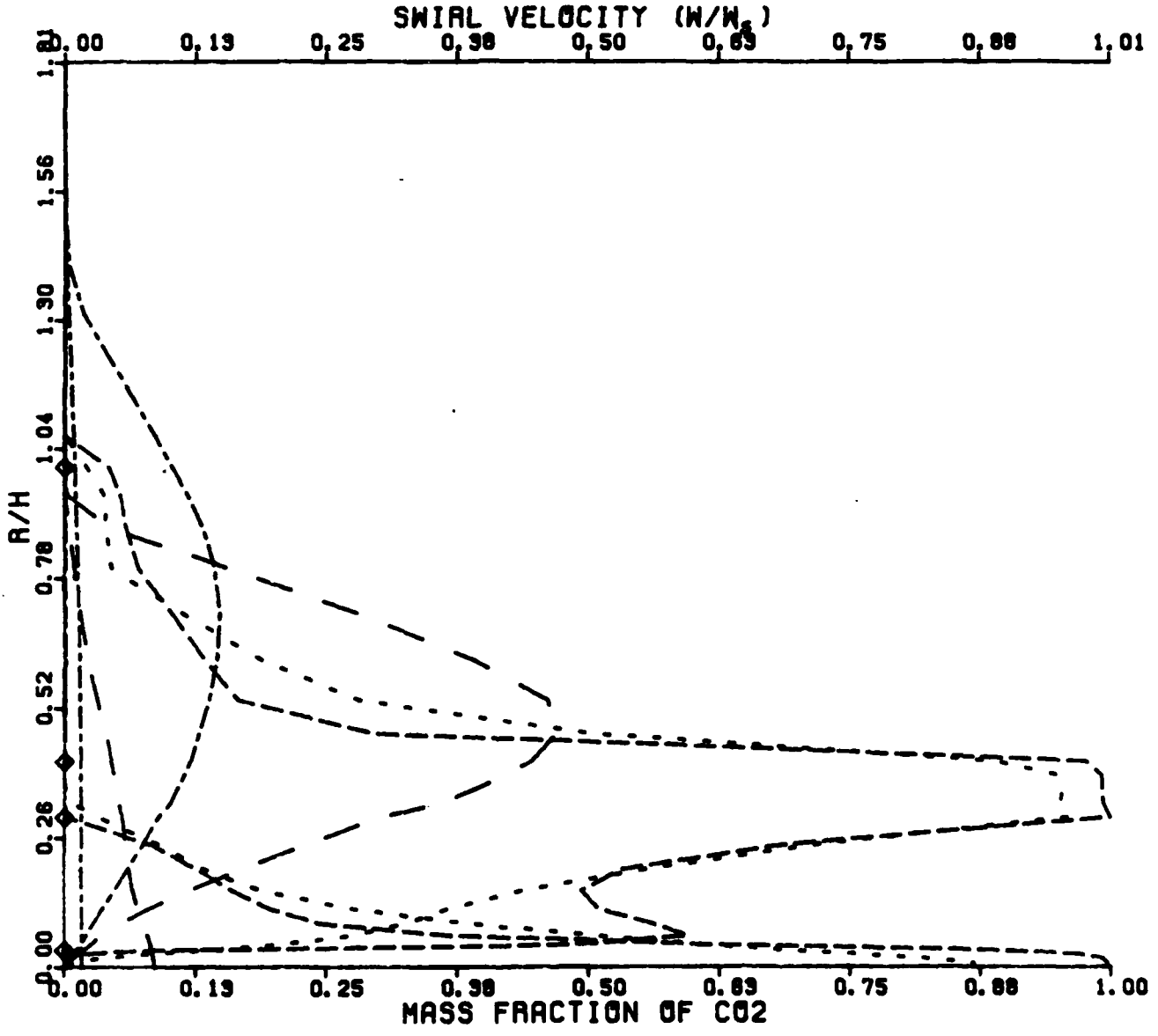

Figure 10(e). Radial Profiles of CO_2 Mass Fraction and Swirl Velocity.

CASE 8
MASS FLOW RATES: ANNULAR= 2.010KG/S, MID= 0.028KG/S, CENTRAL= 5.780KG/HR

_ _ _ X/H=0.0514, - - - X/H=0.2252, ___ X/H=1.0951, _ - _ X/H=4.5887.

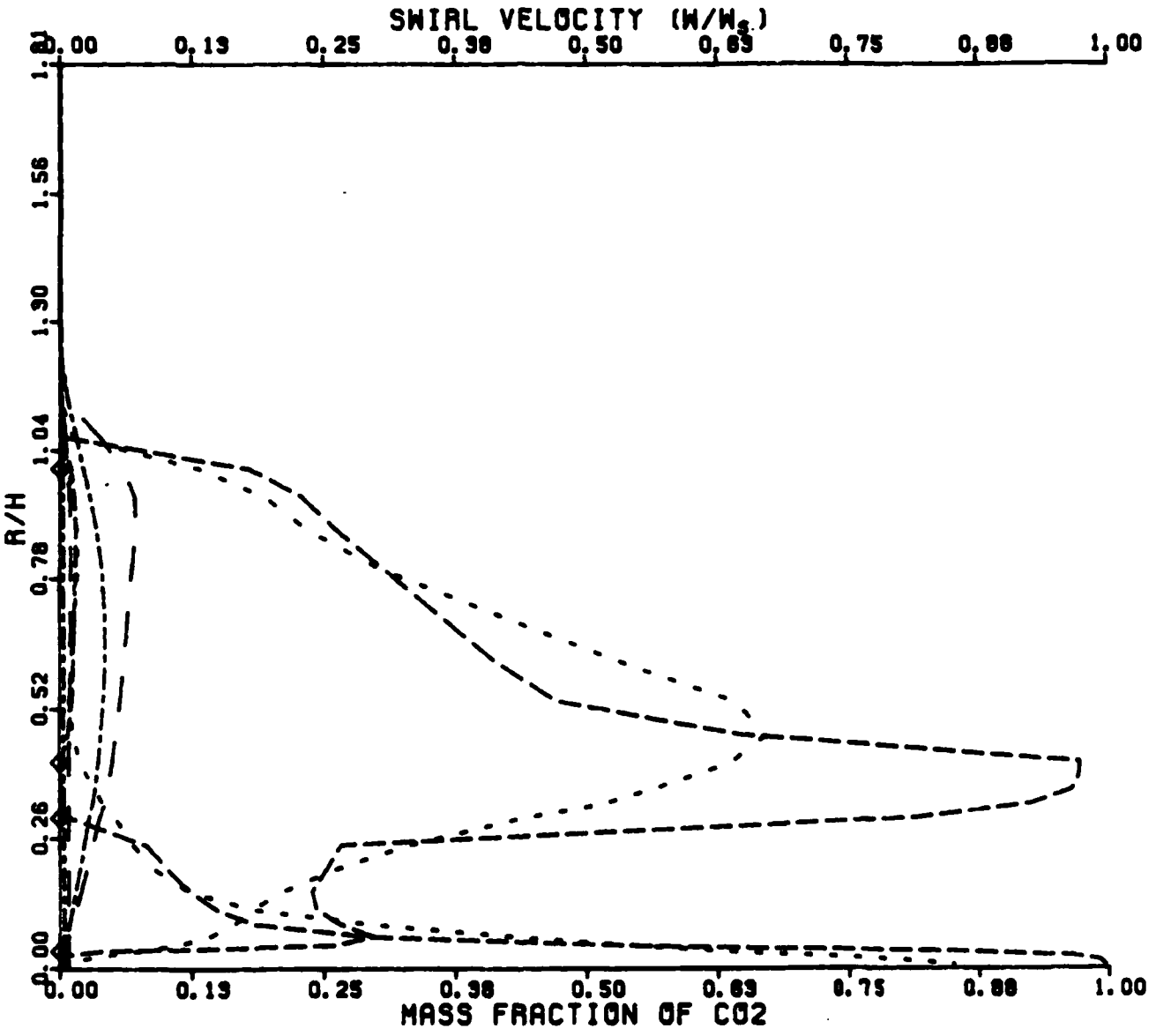

Figure 10(f). Radial Porfiles of CO_2 Mass Fraction and Swirl Velocity.

The distributions of the swirl velocity in the figures correspond to those profiles which display the offcenterline (R/H = 0) peaks. The peak values of the swirl velocity occur in the vicinity of the swirling stream at the two axial stations closest to the bluff body. This is indicative of the fact that the swirl remains confined to the middle stream. The peaks are shifted radially outward, towards the outer annular stream, at the two stations farther downstream. It is interesting to note that all these peaks occur on the outer side of the swirling stream in all the cases. That no peak occurred on the inner side of the swirling stream in all the parametric variations considered by us suggests that this is more likely to be a consequence of the present geometrical parameters. This conjecture can be ascertained only by a CFD examination of a parametric variation of the swirler and centerbody radii.

The profiles at the two near-field locations conform to each other more closely (this is especially true in Figure 10e). The more dramatic effect of the stronger swirling stream is brought out in Figure 10c which shows the relative increase in swirl velocity even at the two far-field locations. Another interesting aspect of the profiles at these two latter locations is noticeable in Figures 10c, 10d, and 10e. The radial profiles in these cases show a much greater symmetry, unlike the clearly asymmetric profiles (more skewed towards the outer annular stream) seen typically. The physical significance of this peculiar behavior is not clear. We must determine from experiments how realistic is the predicted behavior concerning this and other aspects of the flowfield.

Although the radial distributions discussed herein have not addressed the mean axial velocity fields, it is generally likely that these profiles will exhibit trends observed in the previous POSF configuration. The agreement with experimental data is also likely to be fair. Finally, we may expect that Abramovich-type universal profiles (see Reference 2) will also apply in the proposed configuration.

2. REACTING FLOWFIELDS

Cases 9 and 10 of the present CFD study are concerned with the reacting flowfields of the proposed POSF configuration which result from the combustion of gaseous propane in the central jet and air in the two annular streams. Of the two cases, case 9 deals with the swirl-free middle stream, while case 10 corresponds to the swirling middle stream. Before we discuss each case in turn, some comments are in order regarding the reacting-flowfield calculation procedure of Reference 5.

a. Shortcomings of Computational Procedure

The computer code of Reference 5 employs the Magnussen-Hjertager model (Reference 7) for describing the combustion of propane and air (see Paragraph II.2). The source term S_{mf} for the fuel-mass-fraction equation [see Equation (1)], in accordance with this model, is explicitly indicated in Table 1. The appropriate value of S_{mf} is denoted by the minimum of the three terms found inside the square brackets. While a strict implementation of the Magnussen-Hjertager model would require the search for this minimum value, the computer code of Reference 5 has not complied with that requirement. The reason for this lacuna in the code is not clear. When the present study carried out a strict implementation of the Magnussen-Hjertager model in the calculations, the computed results led to nonphysical and large negative mass fractions of oxygen. Presumably, this difficulty might have persuaded the code developers to abandon the correct implementation. For the present, it is essential to recognize this deficiency of the computational procedure.

Furthermore, the computer code imposes an arbitrary lower bound on the temperature field. The prescribed minimum value is 293°K (see line 83 of subroutine PROPS of the code). When this was changed to 150°K, we found that the temperatures in the

flowfield reached values as low as 160°K. It appears that major modifications are required in the algorithm to implement a proper coupling of the combustion model to the hydrodynamics. Clearly, the required algorithm improvements are beyond the scope of the present research study. Instead, the present intent has been to examine two computational cases, mainly to obtain some tentative ideas on the reacting flowfield behavior of the new POSF configuration.

b. Swirl-Free Flowfield

Case 9 has a value of zero for the parameter S_R. The mass-flow rates in all the three streams are identical with the corresponding values of cases 7 and 8 of the nonreacting flows. Thus, this flowfield is largely an annular-stream dominant one. Note that a comparison of cases 7 and 9 will reveal the influence of combustion. Before we look at the computed results, it is important to mention that the present calculations never converged for case 9. While convergence of the numerical calculations depends on the specific value of the many inflow parameters of the problem, no attempt was made to investigate the parametric effect on the numerical convergence for this particular case.

(1) Overview of Flowfield Structure

Figures 11a through 11c show the plots of velocity vectors, temperature contours, and density contours respectively. An overview of the flow structure can be obtained from an inspection of these three plots. Furthermore, the changes in the flowfield caused by the introduction of combustion are noted by comparing Figure 11a with Figure 4b (the bottom half). Thus, combustion is seen to generate an additional vortex in Figure 11a. The vortex center of this clockwise vortex is located farther downstream of the primary vortex center and closer to the centerline than the latter. It appears as if the

CASE 9
MASS FLOW RATES: ANNULAR= 2.010KG/S, MID= 0.028KG/S, CENTRAL= 5.780KG/HR

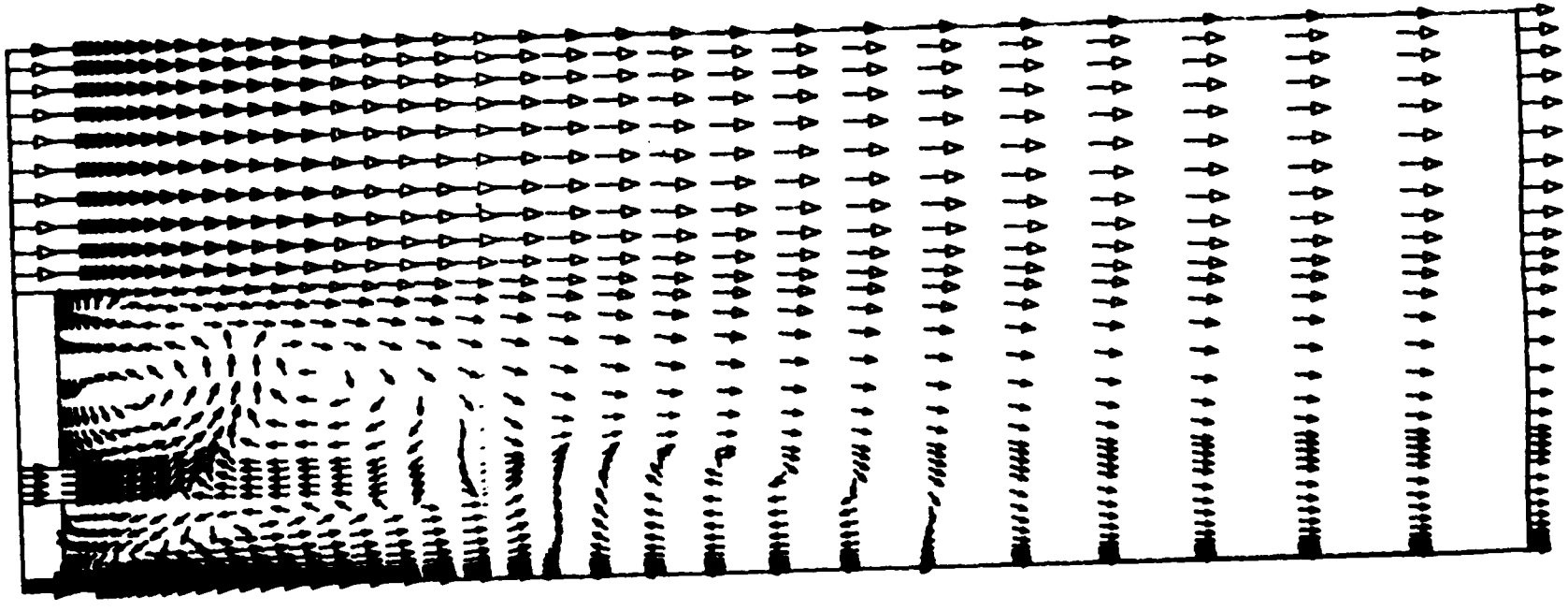

Figure 11(a). Velocity-Vector Plot for Swirl-Free Reacting Flow.

CASE 9
MASS FLOW RATES: ANNULAR= 2.010KG/S, MID= 0.028KG/S, CENTRAL= 5.760KG/HR

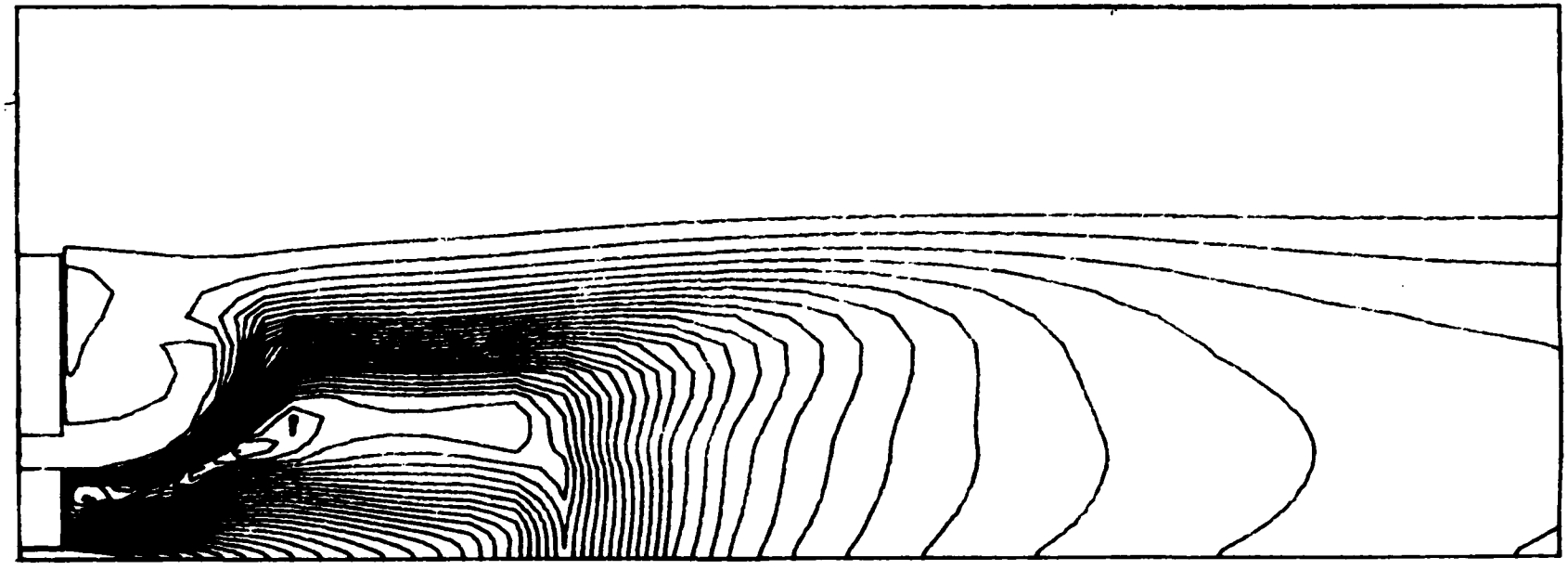

Figure 11(b). Temperature Contours for Swirl-Free Reacting Flow.

CASE 9
MASS FLOW RATES: ANNULAR= 2.010KG/S, MID= 0.020KG/S, CENTRAL= 5.760KG/HR

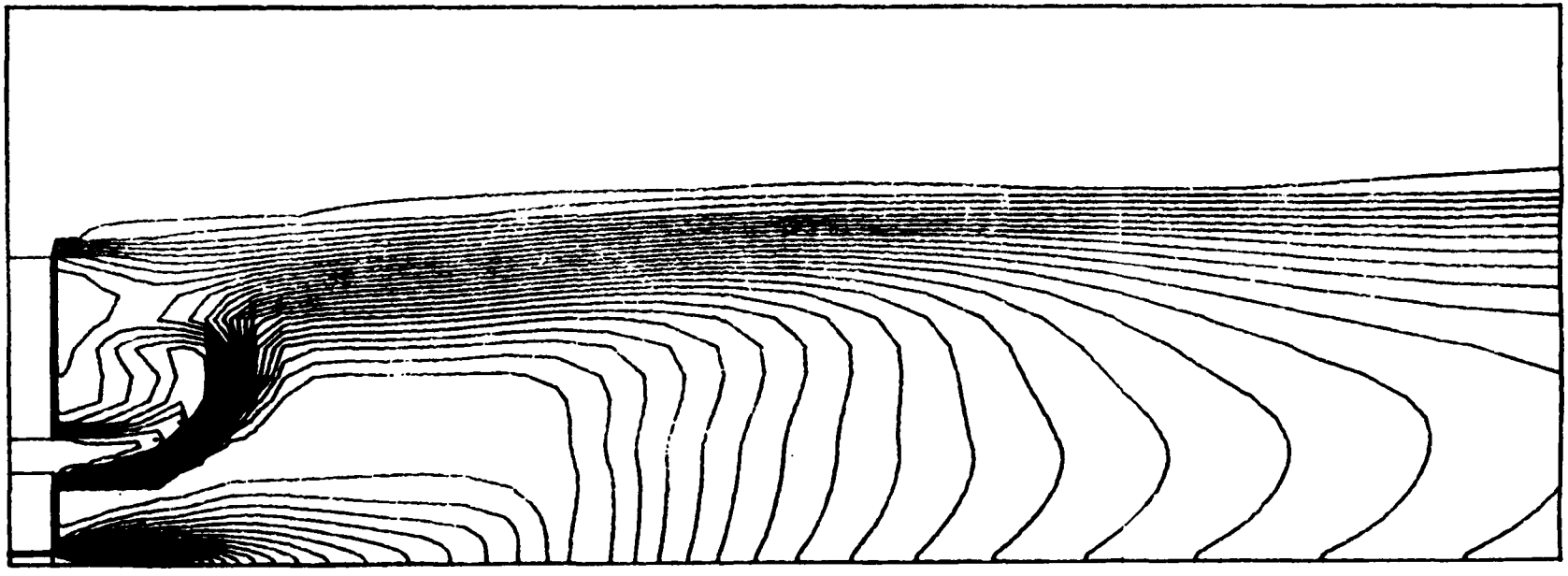

Figure 11(c). Density Contours for Swirl-Free Reacting Flow.

primary vortex in the nonreacting case (Figure 4b) has split into two large vortices moving away from each other. Their spatial separation is large enough that no counterclockwise vortex is required in between (on kinematic grounds). Their separation is enhanced by a further penetration of the central jet. This is evident from the downstream movement of the forward stagnation point to a normalized distance (in terms of the centerbody diameter) of 0.83 which is nearly twice the nonreacting value of 0.465. The downward movement of the rear stagnation point is slight however (from 1.455 previously to 1.475 now). The marked increase in the forward stagnation point location due to combustion is consistent with the experience in the old centerbody configuration (Reference 19).

Further elucidation of the reacting flowfield can be had from Figures 11b and 11c. The regions of the maximum temperature and minimum density in the flowfield can be identified by the dark bands in the temperature and density contours. Clearly these regions correspond to the locations where the combustion intensity of the flame is a maximum. A look at Figure 11a shows that the flame occurs in the region where the fuel is drawn in the counterclockwise direction and is mixed with the incoming fresh air of the middle stream first and the entrained air of the outer annular stream (through the clockwise vortex) next. The supply of fuel into the reaction zone is augmented both by an entrainment process due to a small counterclockwise vortex (located between the central jet and the middle stream) and by the flow reversal and forward stagnation of the central jet due to the bigger clockwise vortex present farther downstream. Note that the latter also aids in bringing the hot combustion products into the reaction zone, thereby providing the required species and energy for the chemical reactions.

(2) Centerline Variations

The foregoing description of the overall flowfield facilitates the considerations of the centerline variations of the axial velocity fields and the scalar fields. These are presented in Figures 12a and 12b respectively. The normalized mean axial velocity profile in Figure 12a may be compared to the corresponding nonreacting case seen in Figure 5g. Such a comparison immediately reveals that with the occurrence of combustion, the mean axial velocity decays more slowly; the central jet penetrates farther; the forward stagnation point is pushed farther downstream (nearly twice as far as in Figure 5g); the magnitude of the peak negative velocity is decreased by more than a factor of 2 and its location is moved farther downstream; and the location of the rear stagnation point and the subsequent recovery of the mean axial velocity are only slightly affected. All these trends are generally consistent with the experience in the earlier POSF configuration (e.g., see Reference 19).

Comparison of the nonreacting and reacting profiles of the rms velocity component shows that there are slight differences in the magnitudes and locations of the two peaks. Overall, however, the turbulence intensity in the reacting case is seen to be higher almost everywhere along the centerline. While the assumption of isotropy has a crucial effect on this prediction, it appears that combustion in the present situation of initially unmixed reactants might offset the decrease in turbulence due to dilatation effect by an increase due to the production of turbulence kinetic energy through augmented shear stress. Future measurements should be able to verify this possibility.

The scalar profiles in Figure 12b show the centerline variations of the mass fraction of propane and the normalized temperature $(T - T_{min})/(T_{max} - T_{min})$. Here T_{max} is the flame temperature. The scalar profiles show that the

CASE 9

MASS FLOW RATES: ANNULAR= 2.010KG/S, MID= 0.028KG/S, CENTRAL= 5.760KG/HR

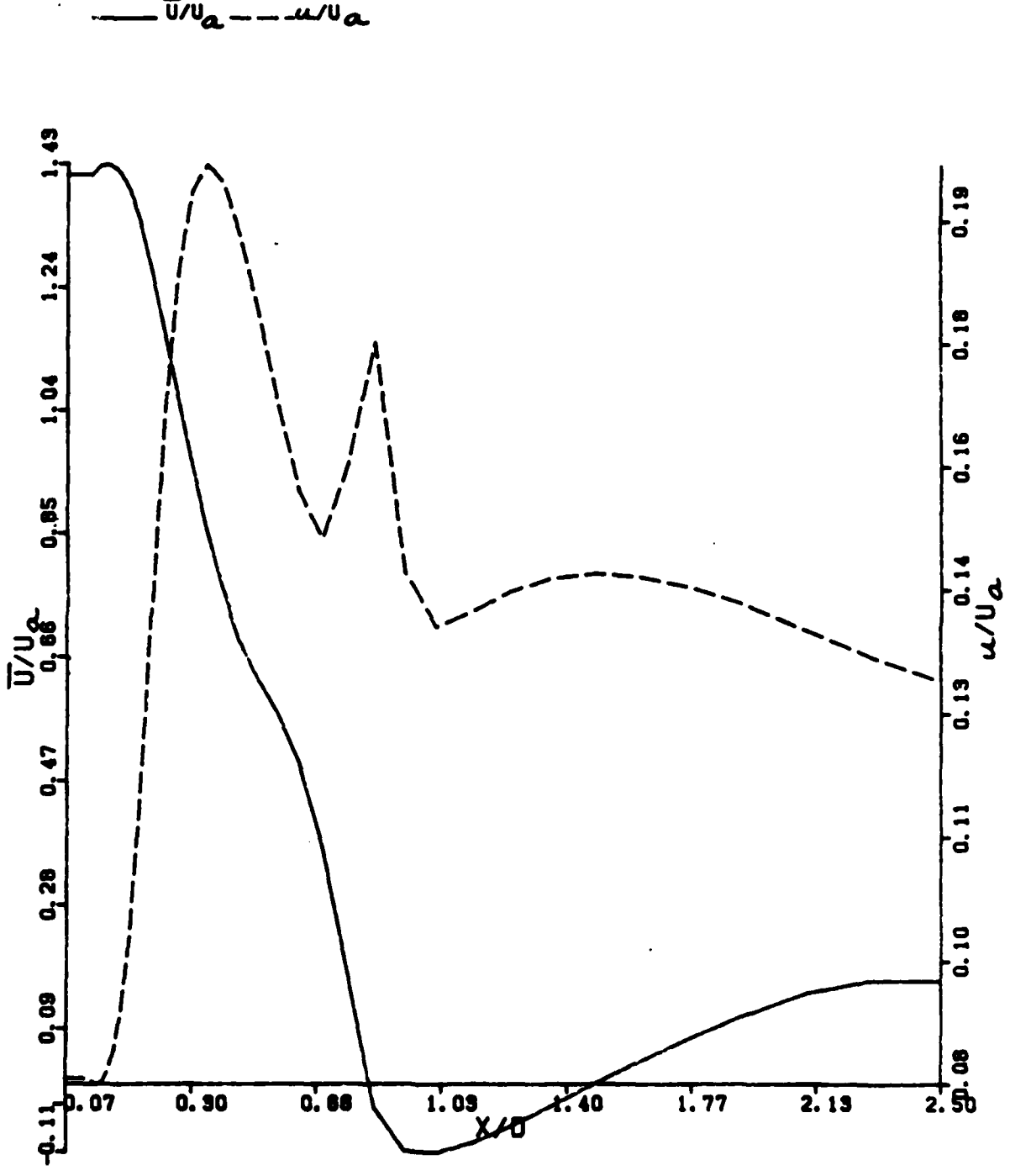

Figure 12(a). Centerline Profiles of Mean and rms Axial Velocity Components.

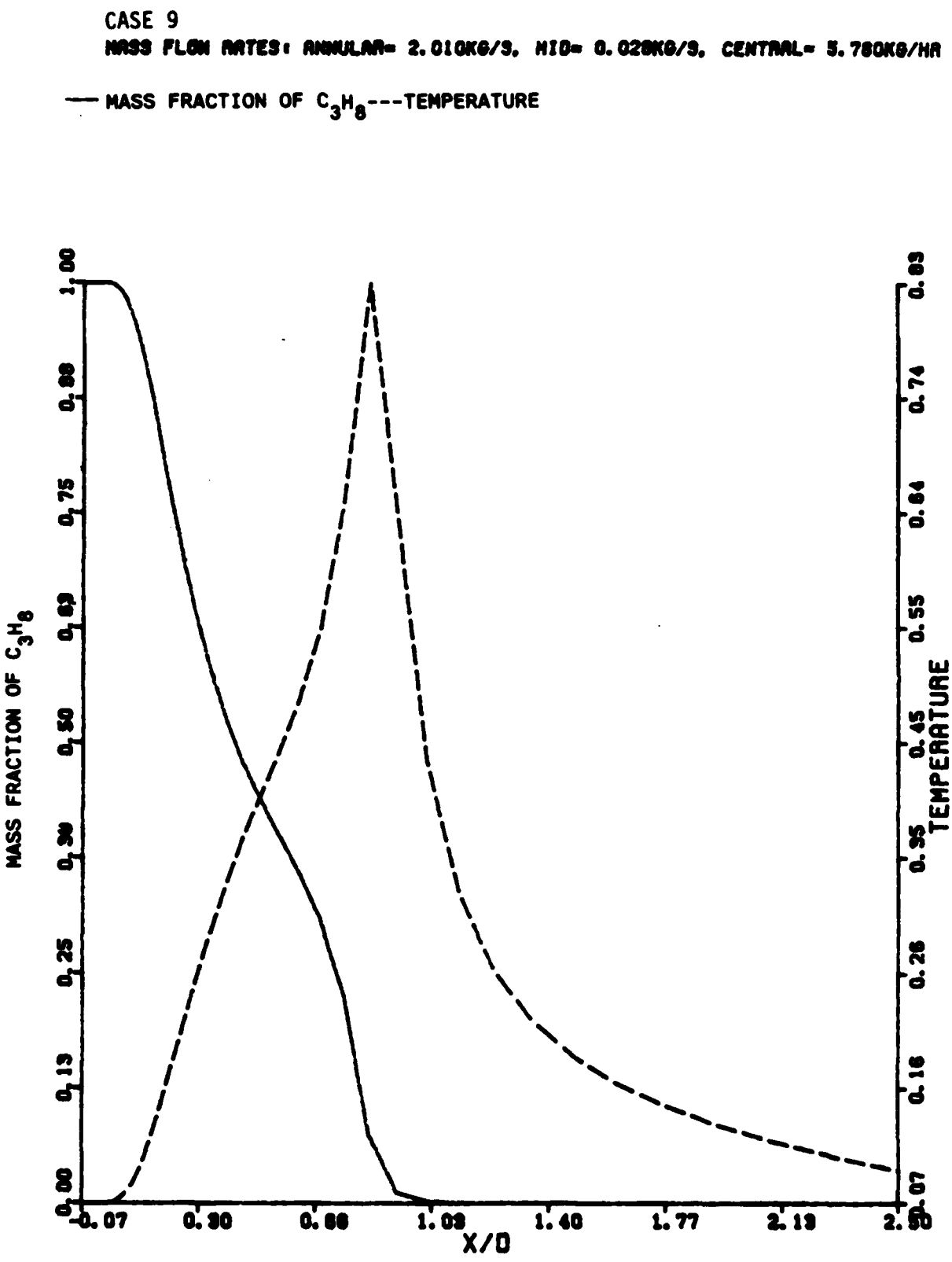

Figure 12(b). Centerline Profiles of Propane Mass Fraction and Temperature.

centerline temperature peaks where the propane mass fraction vanishes. Furthermore, from Figure 12a this location is seen to coincide with the forward stagnation point. Note, however, that the centerline peak temperature is only 83% of the normalized flame temperature. This confirms that the maximum temperature (i.e., the most intense reaction zone) occurs offcenterline. We note that the flame temperature in case 9 is 1,850°K.

(3) Radial Profiles

Before concluding the discussion of case 9, we consider the radial variation of turbulent kinetic energy and temperature at different axial locations. These distributions (for dimensional values of the variables) are presented in Figures 13a and 13b respectively.

A comparison of Figures 8g and 13a shows that there is very little difference in the trends of the radial profiles of turbulence kinetic energy between the nonreacting and reacting cases. Indeed, in the two near-field locations the profiles almost coincide. In the two far-field locations, the profiles coincide in the outer annular region, indicating thereby the very little influence of combustion on the turbulence there. Closer to the centerline, the kinetic energy in the reacting case is more than that in the nonreacting case, the increase being appreciable especially at the farthest axial location. These flowfield features are in conformity with the aspects discussed earlier.

The temperature profiles seen in Figure 13b confirm the overall description suggested by the velocity-vector plot and temperature-contour plot seen in Figures 11a and 11b respectively. The propagation of the reaction zone axially downstream and radially outward is clearly noticeable from the radial distributions of the temperature. Also unmistakable is the negligible impact of combustion on the outer parts of the flowfield.

CASE 9

MASS FLOW RATES: ANNULAR= 2.010KG/S. MID= 0.020KG/S. CENTRAL= 5.780KG/HR

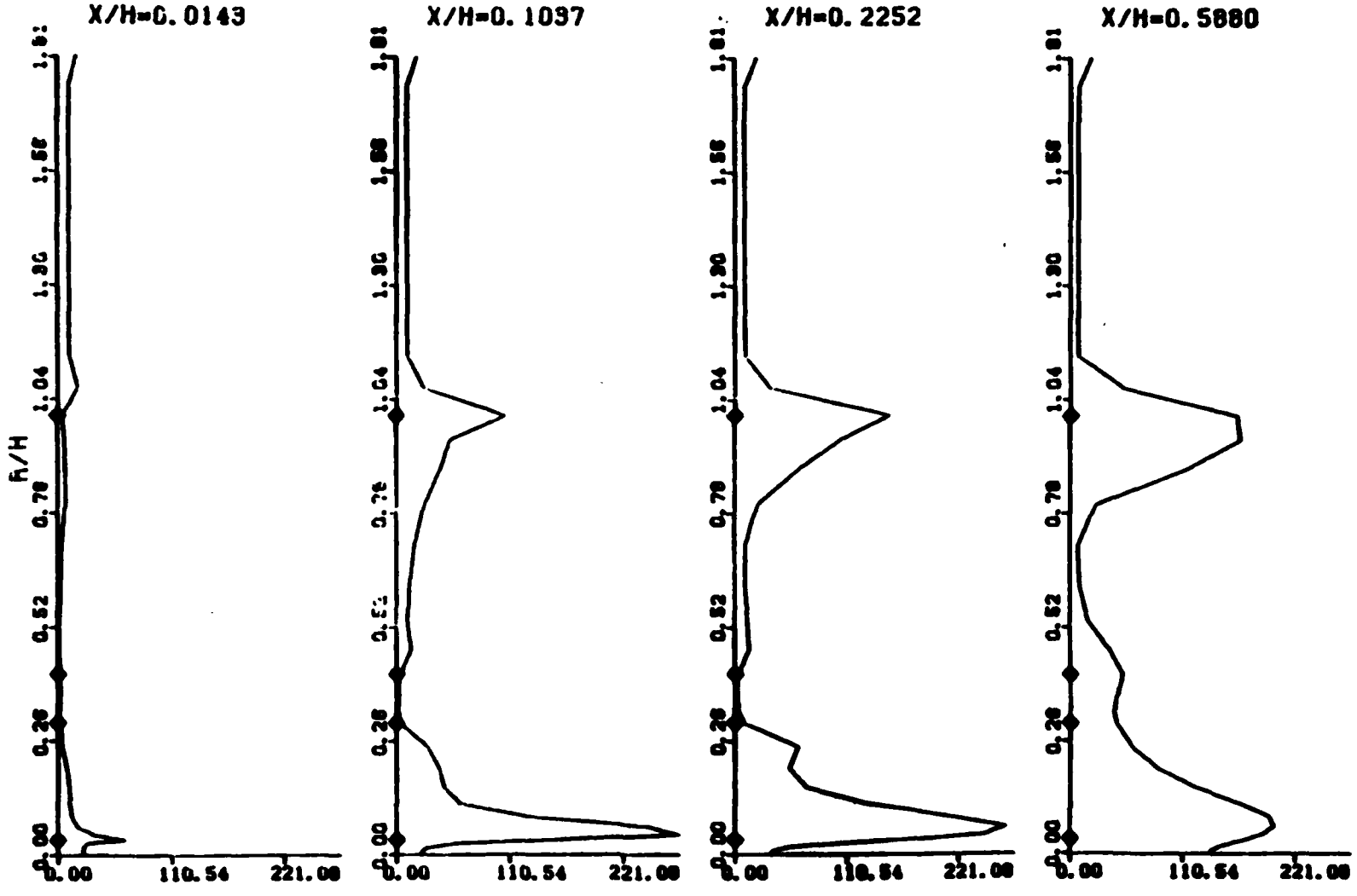

Figure 13(a). Radial Profiles of Turbulent Kinetic Energy.

CASE 9
MASS FLOW RATES: ANNULAR= 2.010KG/S, MID= 0.028KG/S, CENTRAL= 5.760KG/HR

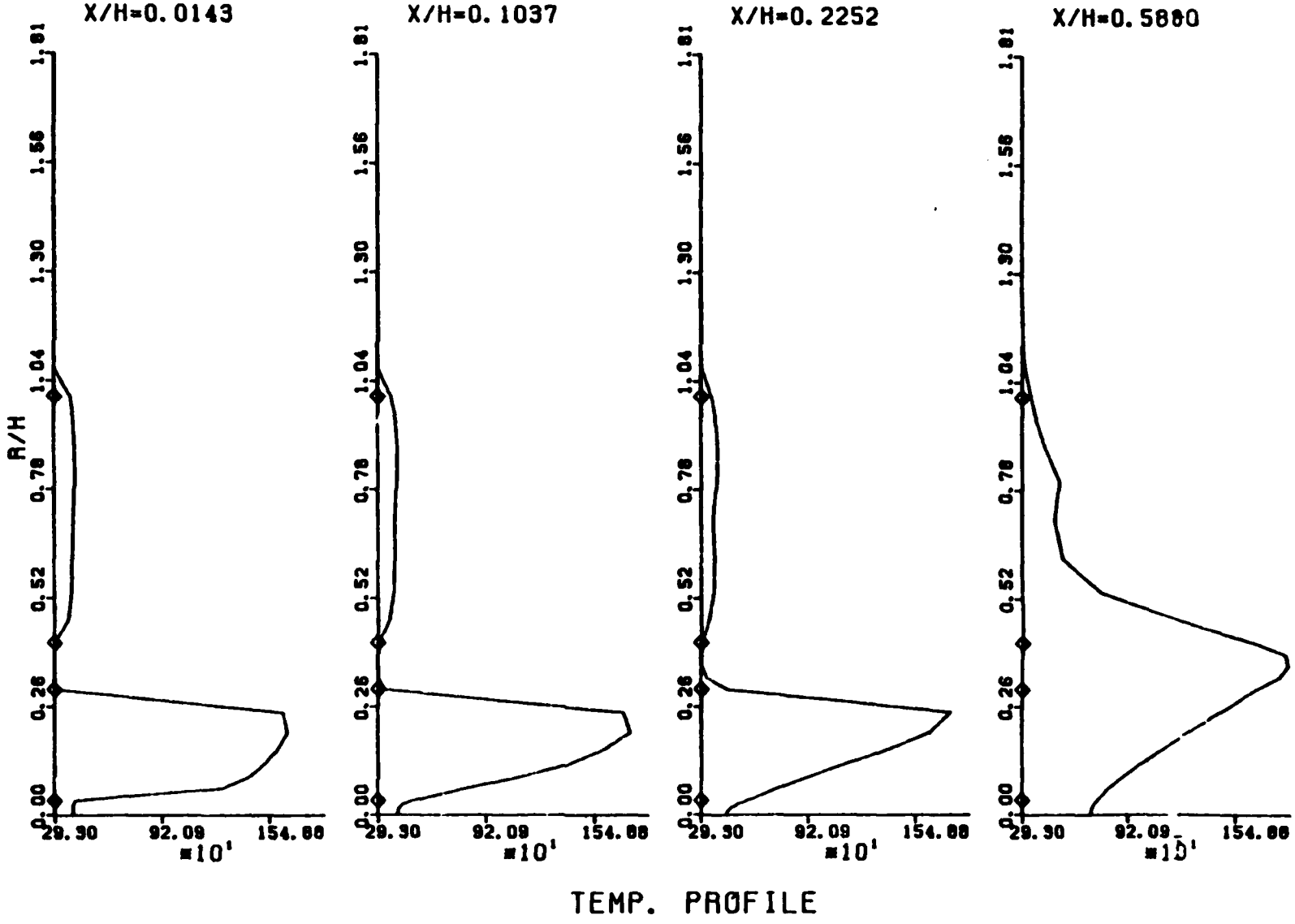

Figure 13(b). Radial Profiles of Temperature.

c. Flowfield with Swirl

The flowfield with nonzero swirl in the middle stream (S_R = 1·0) corresponds to case 10. Note that the computations in this case, unlike those of case 9, had converged. The precise reason for the favorable influence of the presence of swirl on the numerical convergence is not clear.

(1) Overall Flowfield Features

The global features of the flowfield can be understood from the plots of velocity vectors, temperature contours, and density contours seen in Figures 14a, 14b, and 14c respectively. Furthermore, a comparison of cases 9 and 10 shows the effect of swirl on the reacting flowfield, whereas a comparison of cases 8 and 10 reveals the influence of combustion on the swirling flowfield.

From a comparison of Figures 11a and 14a it is clear that while the overall flowfield structure remains the same with or without swirl, the details concerning the location of the vortex centers and the spatial extent of the vortices are different. Thus, with swirl the large clockwise vortex farthest from the bluff body has moved radially outward and axially upstream. This movement towards the centerbody shoulder in turn causes the upstream movement of the other large clockwise vortex, as well as the small counterclockwise vortex (the spatial extent of the latter is almost halved with swirl). These trends were also seen [in Paragraph III.1.a(2)] for nonreacting flows (cases 7 and 8). The small counterclockwise vortex (located between the swirling stream and the central jet), on the other hand, is seen to have moved axially downstream and radially outward (with the radial movement being much smaller than the axial one) when swirl is present. Qualitatively speaking, the net result of these vortex movements is to intensify the mixing rate in the L-shaped region formed by the three leftmost vortices. This is also

CASE 10
MASS FLOW RATES: ANNULAR= 2.010KG/S, MID= 0.028KG/S, CENTRAL= 5.760KG/HR

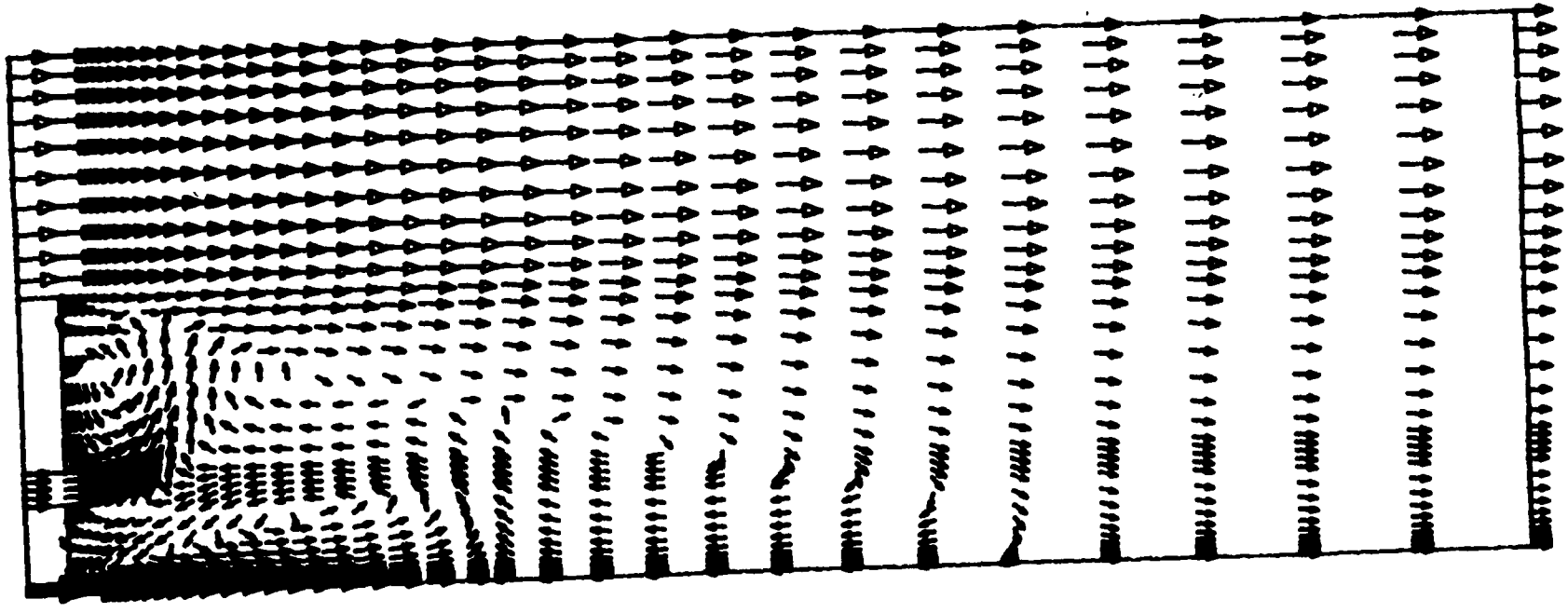

Figure 14(a). Velocity-Vector Plot for Reacting Flow with Swirl.

CASE 10
MASS FLOW RATES: ANNULAR= 2.010KG/S, MID= 0.020KG/S, CENTRAL= 5.780KG/HR

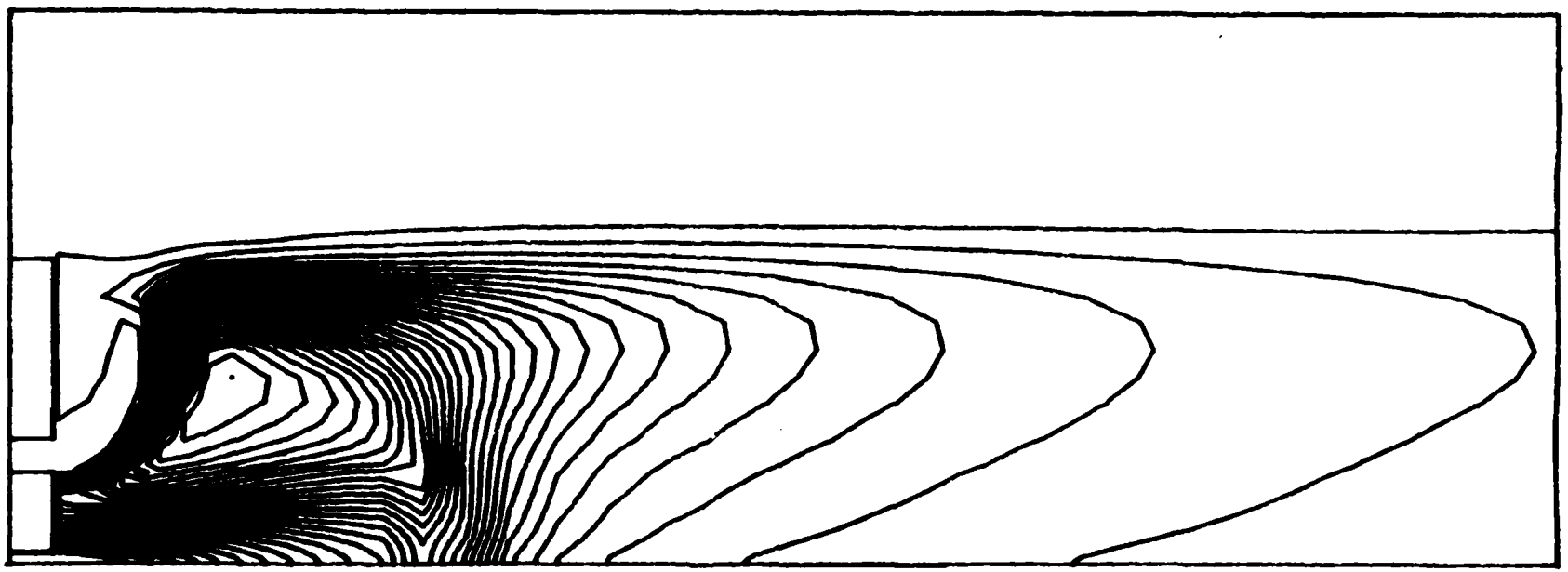

Figure 14(b). Temperature Contours for Reacting Flow with Swirl.

CASE 10
MASS FLOW RATES: ANNULAR= 2.010KG/S, MID= 0.028KG/S, CENTRAL= 5.760KG/HR

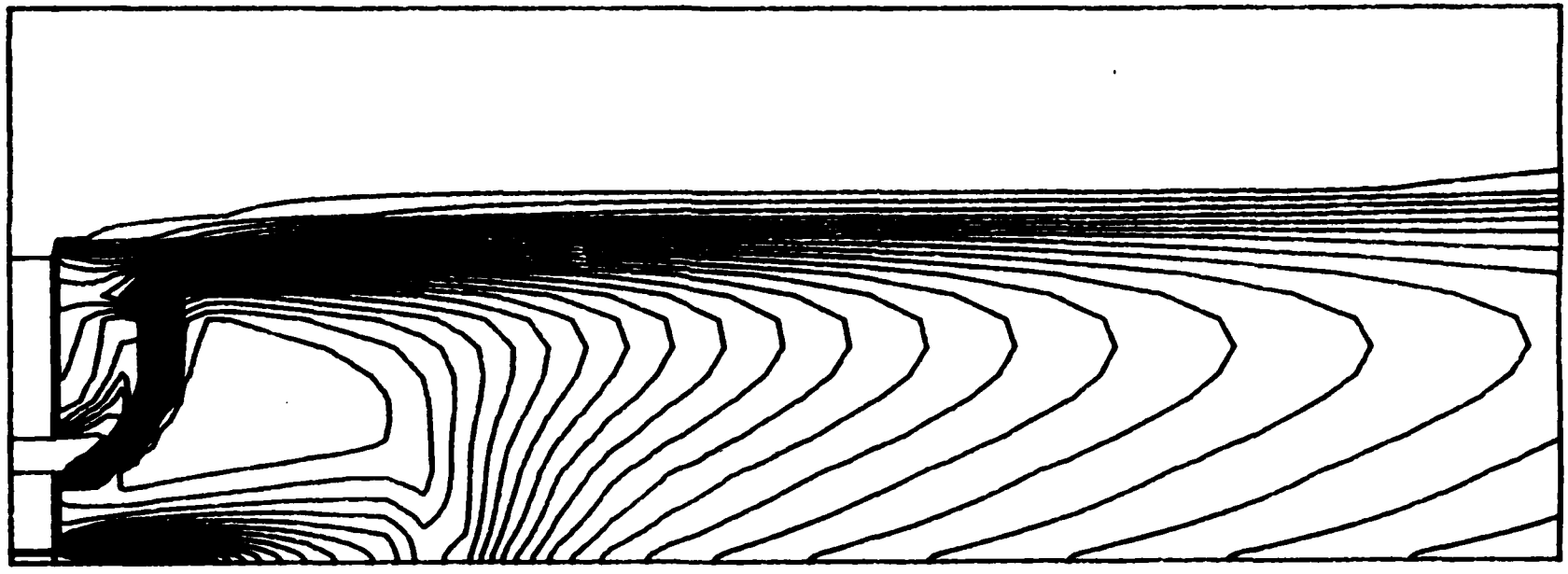

Figure 14(c). Density Contours for Reacting Flow with Swirl.

evident from the more tightly bound system of vortices in Figure 14a, in comparison with that in Figure 11a. More quantitatively, the normalized locations of the forward and rear stagnation points with swirl are 0·735 and 1·62 (the former has moved upstream and the latter downstream). The enhancement of the mixing and combustion processes resulting from the improved flowfield characteristics due to the introduction of swirl is demonstrated by the flame temperature increasing to 1,905°K (from 1850°K for case 9).

The changes in the swirling flowfield due to the introduction of combustion [seen from a comparison of Figures 14a and 4b (the top half) corresponding to case 8 and 10] are similar to the changes noted in the nonswirling flowfield due to combustion [see Paragraph III.2.b(1) for the comparison of cases 7 and 9]. Thus, we encounter all the features such as the splitting of the large clockwise outer vortex into two clockwise vortices (that are spatially separated), the greater penetration of the central jet, and the resulting increase in the normalized distances of the centerline forward and rear stagnation points (the latter to a lesser extent). A quantitative comparison can be easily established from Figures 14a and 4b (the top half).

Further insights on the reacting flowfield are available from the contours of the scalar fields in Figures 14b and c. A comparison of Figures 11b and 14b shows that the introduction of swirl serves to confine the reaction zone closer to the bluff body and that the overall effect is to enhance combustion.

(2) Centerline Variations

The centerline variations of the axial velocity components (mean and rms), the scalars (propane mass fraction and temperature), and the mean swirl velocity component are shown in Figures 15a-c respectively. The effect of swirl on the reacting flow for the axial velocity fields and the scalar fields can be

CASE 10
MASS FLOW RATES: ANNULAR= 2.010KG/S, MID= 0.028KG/S, CENTRAL= 5.760KG/HR

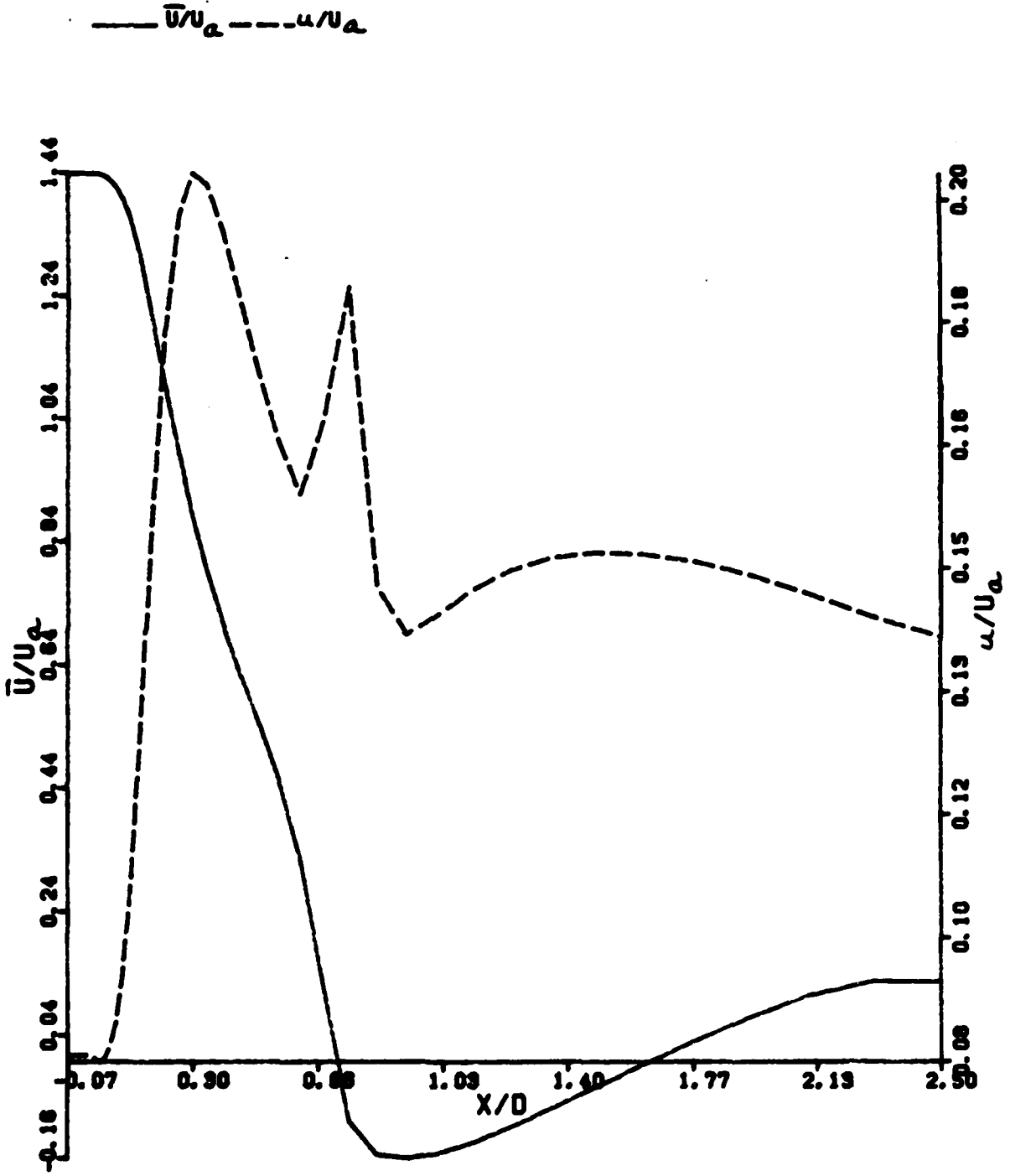

Figure 15(a). Centerline Profiles of Mean and rms Axial Velocity Components.

CASE 10
MASS FLOW RATES: ANNULAR= 2.010KG/S, MID= 0.028KG/S, CENTRAL= 5.760KG/HR

—— MASS FRACTION OF C_3H_8---TEMPERATURE

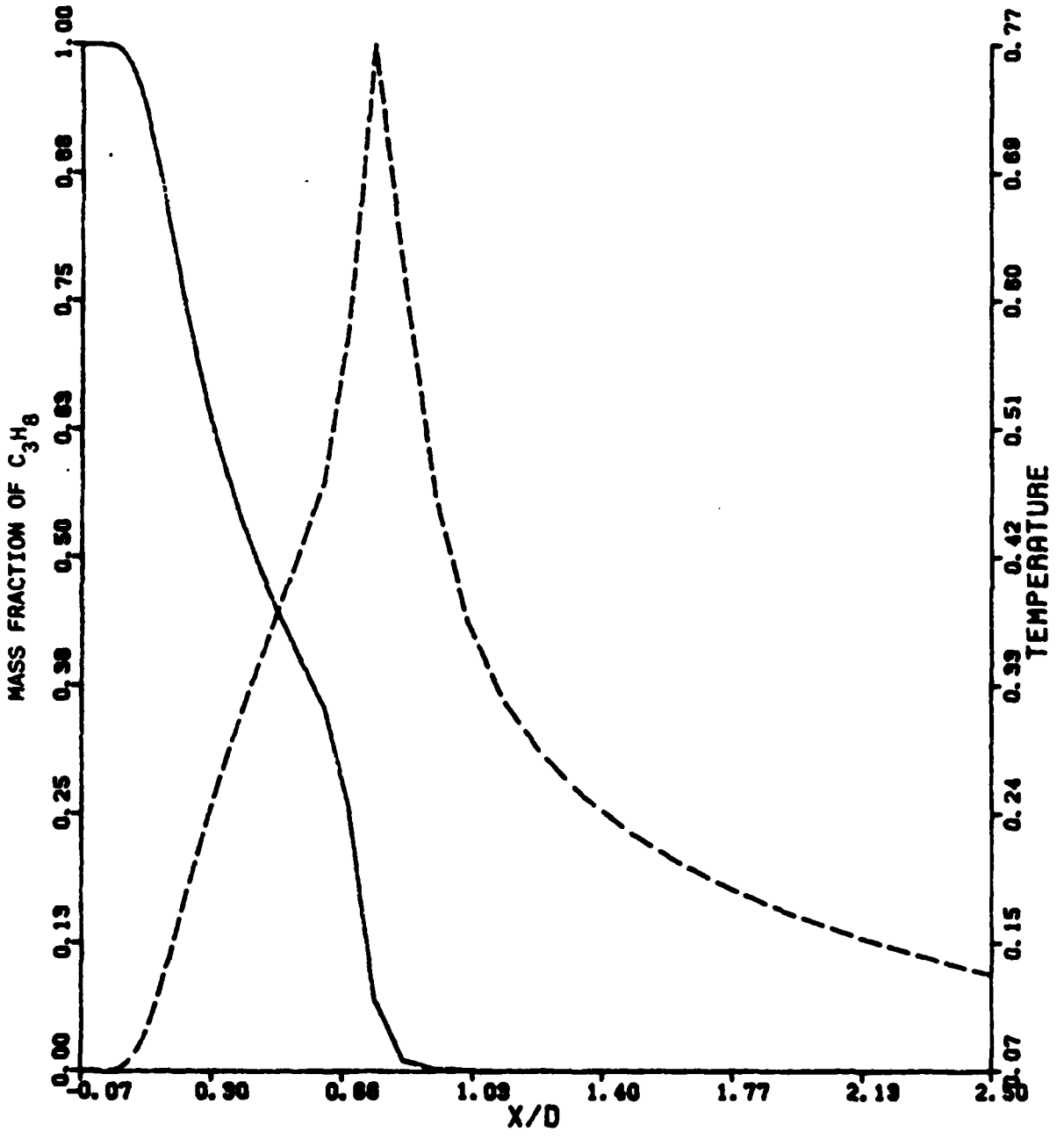

Figure 15(b). Centerline Profiles of Propane Mass Fraction and Temperature.

CASE 10

MASS FLOW RATES: ANNULAR= 2.010KG/S, MID= 0.028KG/S, CENTRAL= 5.780KG/HR

—MASS FRACTION OF C_3H_8---SWIRL VELOCITY

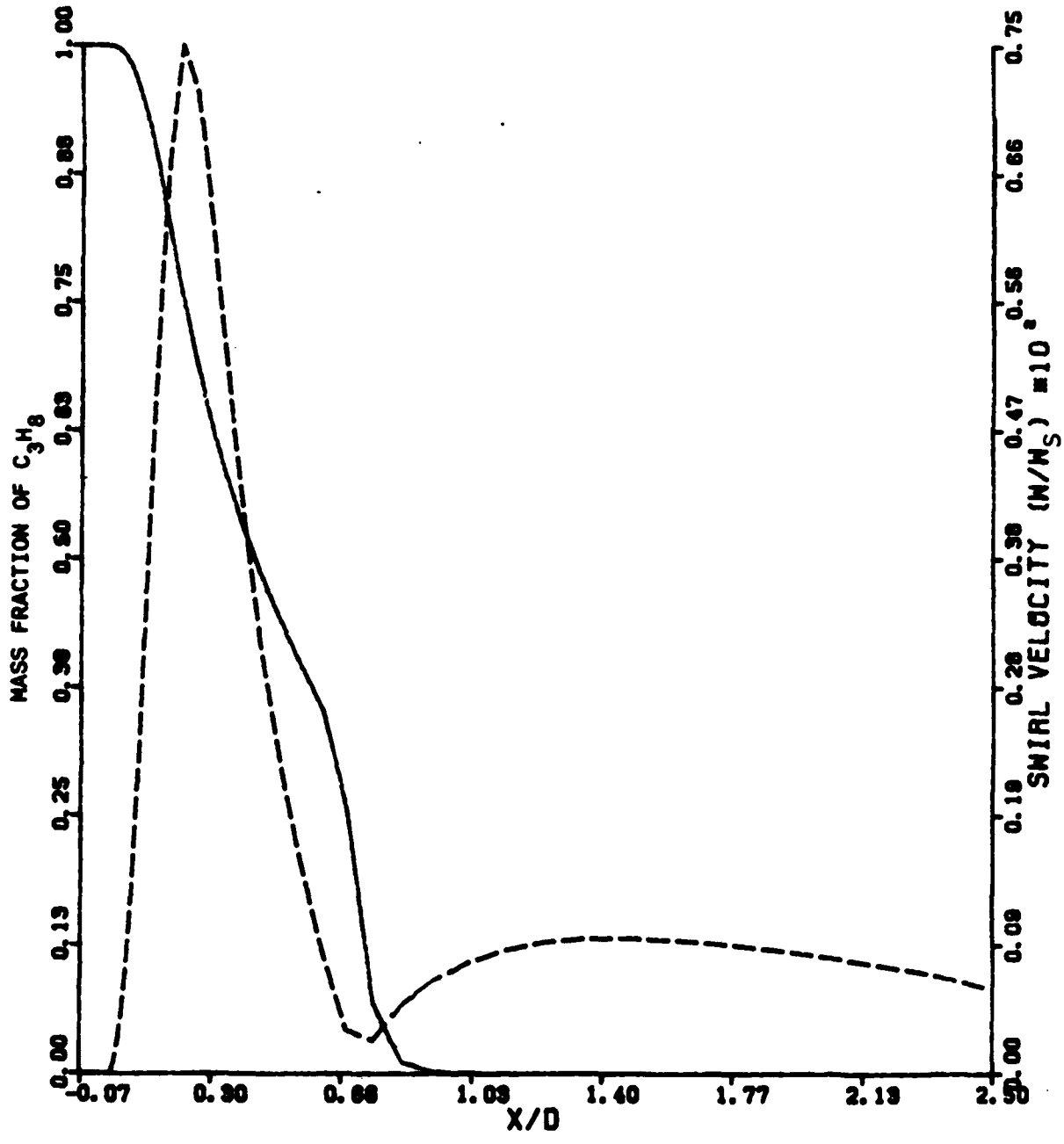

Figure 15(c). Variation of Mean Swirl Velocity.

obtained from a respective comparison of Figures 12a and 15a, and 12b and 15b. The changes in both the mean and rms components are not appreciable. There are slight increases in both stagnation point distances, as well as in the magnitude and location of the peak negative mean velocity. There is a small decrease in the first peak and a small increase in the second peak in the rms profiles.

These observations are confirmed for the scalar profiles also. There is a very little change in the propane mass fraction profiles in Figures 12b and 15b. The temperature profiles exhibit the same overall trends. However, the peak centerline value of the normalized temperature in Figure 15b is only 77%. This shows that while the flame temperature has increased by about 55° with the introduction of swirl, the peak centerline value has dropped by 51° [0·77 (1905-293) + 293 vs. 0·83 (1850-293) + 293]. This appears to be consistent with the greater confinement and intensification of mixing and combustion in the near-wake offcenterline regions caused by the introduction of swirl.

The effect of combustion on the centerline profiles of the swirling flowfield can be easily understood by a comparison of Figures 5h and 15a, 6h and 15b, and 7f and 15c for the axial velocity components, scalar fields, and the mean swirl velocity respectively.

As seen earlier for the swirl-free flowfield [in Paragraph III.2.b(2)], the effect of combustion on the mean and rms velocity components is to produce similar trends, viz., greater penetration by the central jet, increased centerline stagnation point distances, slower decay of the mean velocity, and an overall increase almost everywhere of the rms velocity. Thus, all our earlier comments in connection with the nonswirling flow apply here also. An interesting exception, however, is that while the overall rms velocity trends are preserved in cases 7

and 9 (Figures 5g and 12a), in case 10 the effect of combustion is much more pronounced on the first rms velocity peak. Thus, whereas the first peak is smaller than the second in Figure 5h (case 8), it becomes larger in Figure 15a (case 10). This behavior (which will be further clarified in our discussion of the radial profiles) provides additional evidence of the greater turbulence activity in the near field.

In the comparison of the scalar fields, very little of significance could be said, in view of the direct and strong effect of combustion on both the temperature and propane mass fraction. Note, however, that the increased penetration by the central jet in the reacting flowfield is clearly evident from the slower decay of the propane mass fraction (in Figure 15b) when compared to the decay of CO_2 mass fraction (in Figure 6h). Of course, unlike case 8 where the profiles of CO_2 mass fraction and temperature coincide, case 10 properly describes the peaking of the temperature caused by the exothermicity of combustion.

Figure 15c and 7f bring out the effect of combustion on the mean swirl velocity variation close to the centerline. Recall the earlier discussion [in Paragraph III.1.b(4)], however, regarding the negligibly small magnitudes of the swirl velocity in the vicinity of the centerline. Keeping this in mind, we see that the normalized swirl velocity profile differs negligibly initially. Although the peak value has increased by nearly 30% with combustion, the location of this peak has only slightly shifted downstream. A more significant change is noted subsequently, as the proximity to the reaction zone increases. The swirl velocity begins to decay much more slowly and when the local minimum occurs, its location is approximately twice as far (in Figure 15c) as that in the nonreacting case (Figure 7f). This behavior is consistent with the increased penetration by the central jet. Farther downstream of the minimum location, there is no appreciable effect of combustion on the swirl velocity.

(3) Radial Profiles

Finally, we examine the radial distributions of turbulence kinetic energy, temperature, propane mass fraction, and mean swirl velocity before concluding the discussion of case 10. Figures 16a through 16c present these radial profiles.

The swirl in the middle stream does not appear to have a significant effect on the turbulence kinetic energy profiles. This is readily apparent by comparing Figure 16a with Figure 13a. Only at the farthest axial station is there some redistribution of the turbulence energy. With swirl, the magnitudes of the peaks at the extremities (i.e., near the centerline and towards the outer annular stream) are slightly decreased and the magnitude in the middle (from the inner radius of the swirling stream to about eight-tenths of centerbody radius) is increased. At the two axial stations farther upstream too, the incipient tendency of swirl to increase the turbulence kinetic energy in the middle can be noticed, but the increase is not significant. Overall, it can be safely said that the introduction of swirl certainly causes an increase in the turbulence activity in the mid-radial regions, an outcome that contributes to, and is consistent with, the enhanced mixing and combustion alluded to earlier.

The effect of combustion on turbulence kinetic energy can be discerned from comparing Figure 16a with Figure 8h. Minor differences are noted between the two cases, especially at the peaks. Below the inner radius of the swirling stream, some increase in the kinetic energy is seen at the second and third axial stations. At the farthest station, an increase in the near-centerline peak and a decrease in the outer peak are also noted. These trends are similar to those discussed for non-swirling flows in Paragraph III.2.b(3) and are consistent with our anticipations.

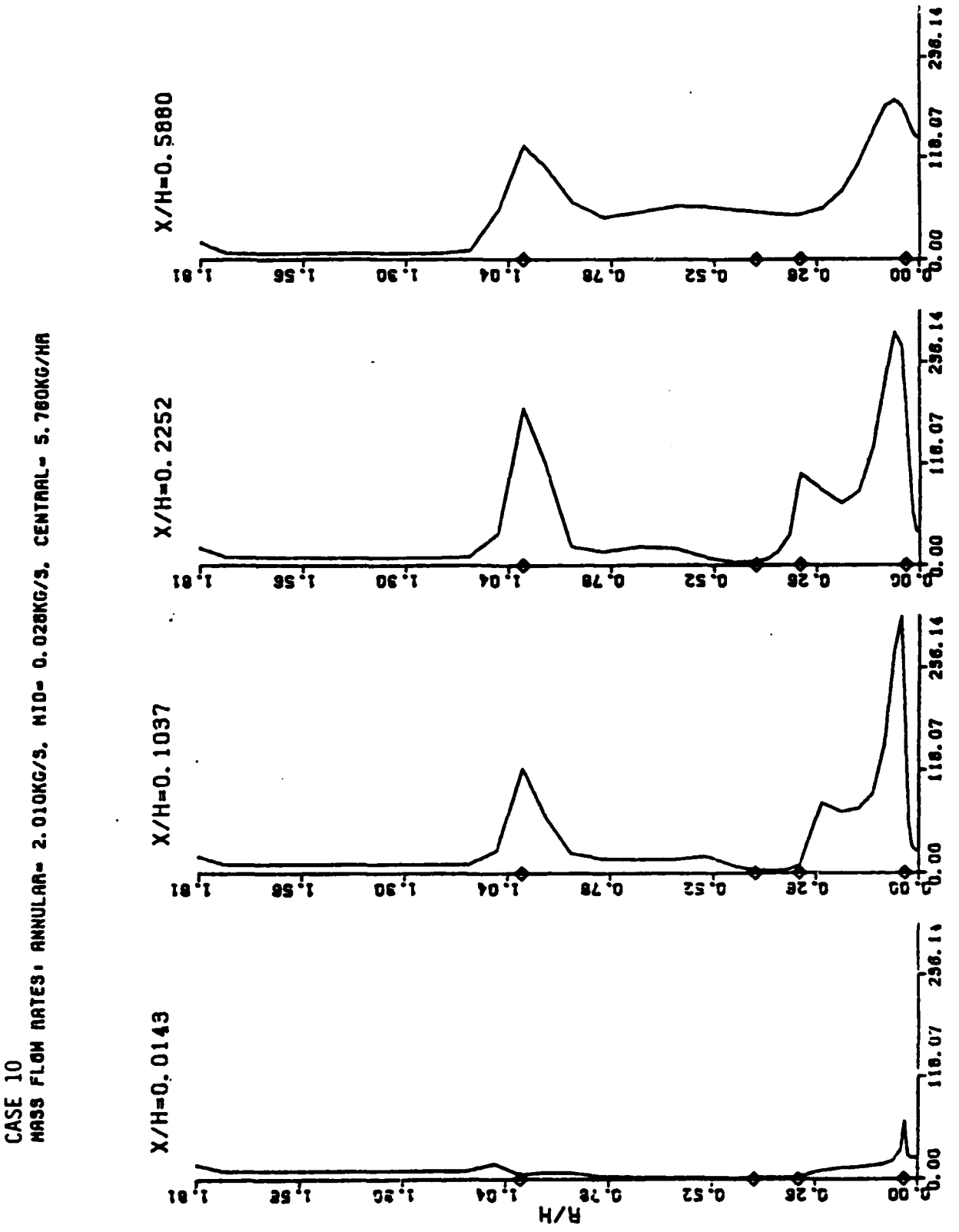
CASE 10
MASS FLOW RATES: ANNULAR= 2.010KG/S, MIO= 0.028KG/S, CENTRAL= 5.780KG/HR
TURBULENT KINETIC ENERGY
X/H=0.5880
X/H=0.2252
X/H=0.1037
X/H=0.0143
0.00
118.07
236.14
0.00
0.26
0.52
0.78
1.04
1.30
1.56
1.81
R/H

MASS FLOW RATES: ANNULAR= 2.010KG/S, MID= 0.020KG/S, CENTRAL= 5.780KG/HR
CASE 10

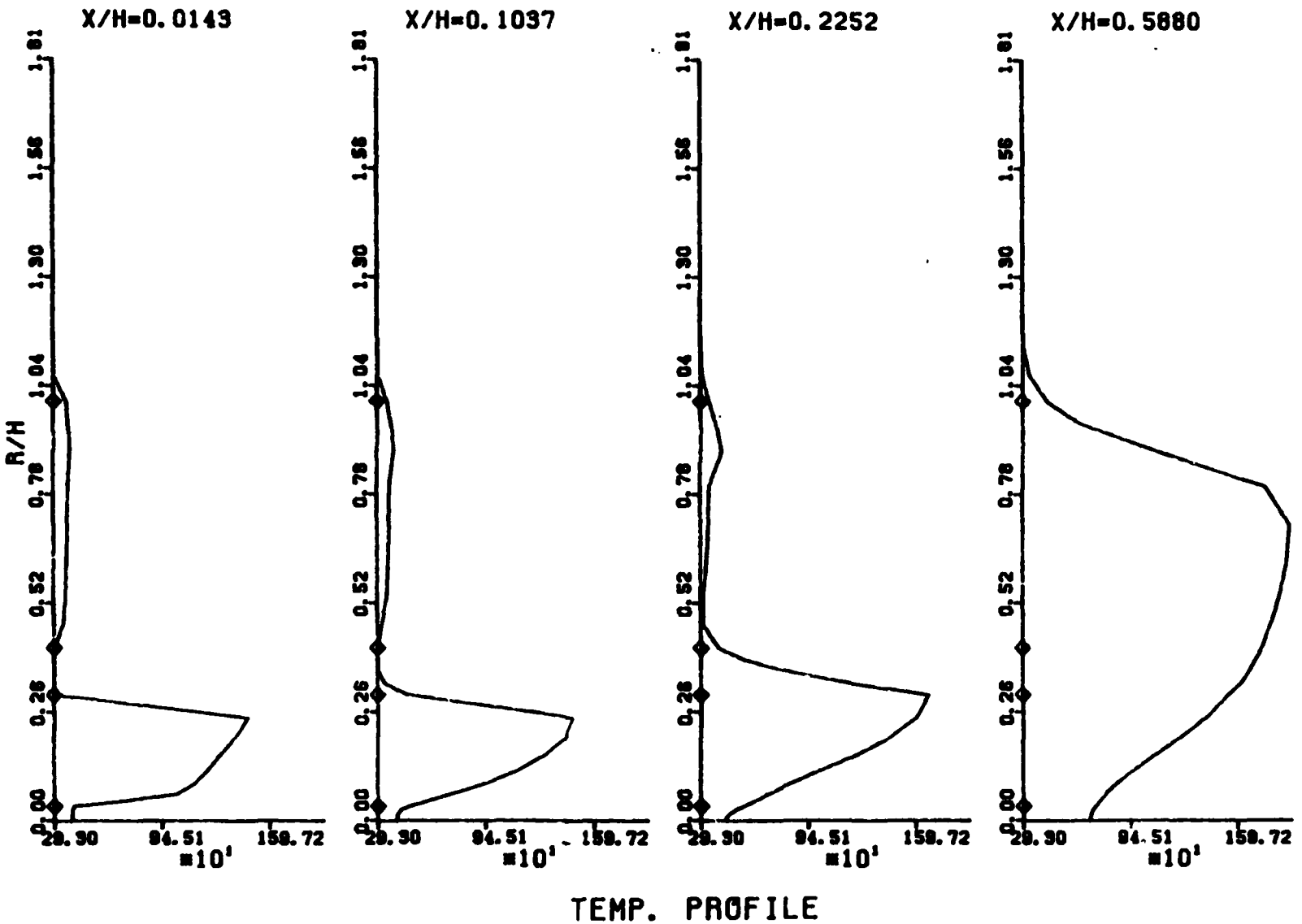

Figure 16(b). Radial Profiles of Temperature.

CASE 10
MASS FLOW RATES: ANNULAR= 2.010KG/S, MID= 0.020KG/S, CENTRAL= 5.760KG/HR

____ X/H=0.0514, . . . X/H=0.2262, ___ X/H=1.0851, ____ X/H=4.5887,

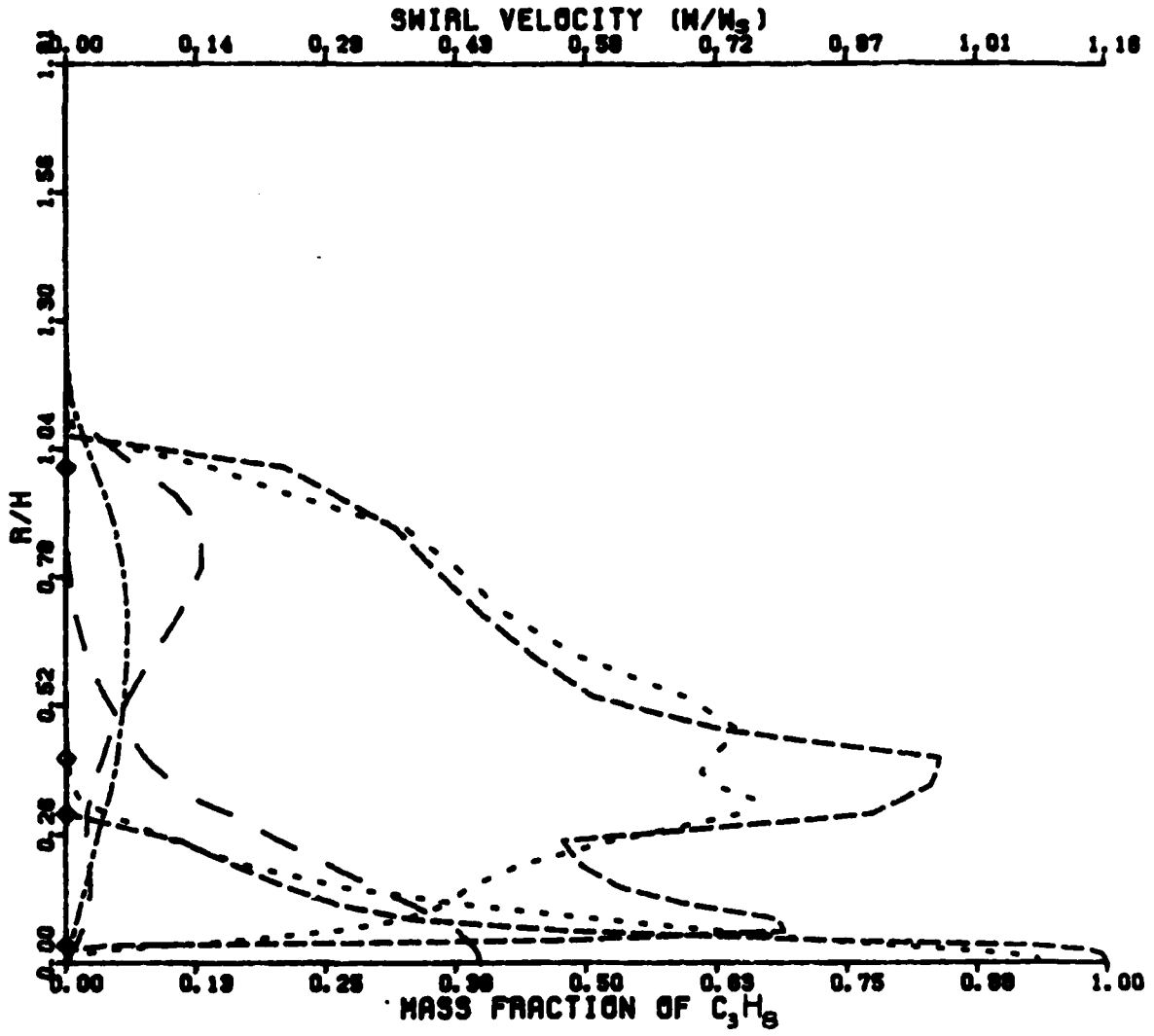

Figure 16(c). Radial Profiles of Propane Mass Fraction and Swirl Velocit

Figure 16b shows the radial profiles of the dimensional temperature at the four axial stations. As seen in Figure 13b for the swirl-free reacting flow, the profiles in Figure 16b also display the propagation of the reaction zone in a radially outward and axially downstream direction. A respective comparison of the individual plots in Figures 13b and 16b reveals the effect of swirl on the radial temperature profiles. At the two near-field locations, the profiles show that the only difference in them is a decrease in the peaks by about 20% due to the introduction of swirl. Farther downstream, this decrease begins to get smaller and there is also a radial spread of the hotter regions. This is dramatically established at the farthest station where the peak temperature is larger with swirl; the radial spread of the hotter regions is nearly doubled; and the region between the inner radius of the swirling stream and eight-tenths of centerbody radius is characterized by uniformly high temperatures (exceeding 1600°K). This particular profile clearly demonstrates that the introduction of swirl greatly enhances the combustion and heat release processes in the mid-radial regions.

The radial distributions of propane mass fraction and mean swirl velocity are shown in Figure 16c. As seen in Figure 10 (a through f) of nonreacting flowfields, the four profiles of the swirl velocity are those which exhibit the offcenterline peaks. The propane mass fraction profiles are monotonic and closer to R/H = 0. At the two near-field stations, the radial spread of propane is small and there is negligible mixing of air at these radial locations. At the third axial station, nonzero values of propane mass fraction can be seen as far as eight-tenths of centerbody radius. Note too the significant mixing with air in these radial regions (e.g., the maximum value of propane mass fraction is only 38% at R/H = 0). At the farthest axial station, of course, propane is no longer present, having been consumed farther upstream at all radial locations. An inspection of Figure 10f (for the nonreacting case 8) shows that the radial spread of CO_2 is much less. Also at the two

far-field stations, nonzero values of CO_2 mass fraction were still present. Therefore, the introduction of swirl is seen to have improved the mixing of propane and air in the near-field offcenterline locations and thus to have contributed to better and more complete combustion. This observation, of course, is consistent with the radial temperature profiles discussed previously (note the different axial locations in Figures 16b and 16c).

Finally, the swirl velocity profiles in Figure 16c show the effect of combustion when they are compared with the corresponding profiles of Figure 10f. We note that at the two near-field axial locations there are minor differences. The peak normalized values at the nearest location are almost unchanged in their magnitudes (note the difference in the scales) and radial locations. At other radial locations above and below the peaks, the swirl velocity with combustion is generally higher. This is especially true of the smaller peaks closer to the centerline. Although the radial (outward) movement of this peak is small with combustion, its magnitude is almost trebled. This behavior of enhanced swirl velocity due to combustion is consistent with the earlier observations. These features are also exhibited by the profile at the second near-field station. In addition, while the outward spread of swirl remains essentially the same, the inward spread (i.e., towards the centerline) of swirl with combustion has increased. No doubt, this has contributed to the improved combustion in these radial regions. At the two far-field locations, the magnitudes of the swirl velocity are quite small. But even in these locations, the increase due to combustion is noticeable. For instance, the swirl velocity at eight-tenths of centerbody radius is doubled with combustion.

SECTION IV
CONCLUSIONS AND RECOMMENDATIONS

This section outlines the major conclusions emerging from the CFD investigations of the present Scholarly Research Program and, in the light of these conclusions, offers some recommendations concerning further assessment of computations of gas turbine combustor-like flowfields.

1. CONCLUSIONS

Numerical predictions of the recirculating confined turbulent flowfields with and without swirl in both nonreacting and reacting situations have been made for the proposed POSF combustor configuration under the framework of time-independent, Reynolds-averaged Navier-Stokes equations. No time-dependent formulation has been considered within the scope of the present program for the prediction of the proposed configuration, either for obtaining the steady-state solutions, or for describing the dynamic flowfield features likely to be encountered. However, an assessment of the solutions of the time-dependent, Reynolds-averaged Navier-Stokes equations for the nonreacting flowfields in the existing POSF centerbody configuration through the MacCormack algorithm is documented in Volume I of this report. Some of the conclusions and recommendations reported there must be considered in conjunction with those documented here. Following are the main conclusions of this study:

- Calculations using the time-independent, Reynolds-averaged formulation with the k-ϵ turbulence model have furnished the numerical predictions of the complex turbulent flowfields in the proposed ducted bluff-body combustor configuration.

- A limited parametric examination of the various fluid dynamical aspects relating to the two annular air streams

(swirl-free outer and swirling inner flows) and the central fuel jet has addressed the effects of mass flow rates, swirl, and combustion on the computed flowfields.

- The CFD examination of the steady-state flowfields has considered the features of the global flowfield from the velocity-vector plots (and also from the contours of the temperature and density fields in reacting flows), the variations of the centerline profiles of selected variables, and the radial distributions of these variables at a few axial locations; and thereby obtained descriptions of the complex flowfield interactions inherent in the proposed configuration.

- The success of the present CFD predictions remains to be verified by experimental measurements in the POSF combustor. Thus, the present testing of CFD methods against hitherto nonexistent and nonmeasured flowfields represents true predictions whose validity is ascertainable by experimental means.

- Although the present predictions remain to be validated, the internal consistency exhibited by these predictions and their conformity with some of the predicted behavior verified in the existing centerbody configuration encourage the belief that the numerical predictions will show reasonable agreement with the actual flowfield behavior.

- The success anticipated for the predictions in conforming to the realistic behavior, however, appears to be restricted to the mean-field description. The quantitative agreement of the predictions of the rms fields with the experimental data is likely to remain poor. Again, even in the mean field, the anticipated success in the reacting-flow predictions is unlikely to match that for nonreacting-flow predictions.

- Nevertheless, the present predictions are expected to offer significant insights into the development and testing of the proposed POSF combustor to simulate some essential aspects of the primary zones of turbojet combustors.

2. RECOMMENDATIONS

The present study offers the following recommendations for further activity. These complement the recommendations offered in Volume I of this report and in References 2 and 3.

- The Reynolds-averaged computational procedure employed in the present study must be evaluated in a number of aspects. These include grid sensitivity of the computed solutions, effect of geometrical and fluid mechanical parametric variation on the numerical convergence (especially in reacting flows), and the influence of variation of the temperature lower bound on the predictions of reacting flows.

- Some of the interesting implications of the present predictions and their flowfield ramifications must be investigated through an integrated experimental and predictive research. Of particular significance are the CFD examination and the experimental verification of (a) the influence of bluff-body blockage ratio variation; (b) the effect of the variation in the inner and outer radii of the swirler; and (c) the effect of variation in the swirl angle.

- The Reynolds-averaged formulation for the swirling flows must be examined in terms of full three-dimensional equations. In other words, the validity of assumption of axisymmetry in the mean used in the present predictions remains to be verified.

- It is likely that even the mean-field predictions are expected to suffer from the anisotropic effects of the near wake which are not taken into account in the k-ε model. A first step to consider with the full three-dimensional formulation is the incorporation of the algebraic stress model (ASM). With the validated experience of ASM, future efforts must explore the consideration of the full Reynolds-stress equations. There is reason to believe, unfortunately, that there is no guarantee of thermodynamic realizability connected with the stress-equation model. Nonetheless, this question remains to be addressed by a CFD investigation.

- Computational aspects relating to the reacting flowfields in the existing procedure (Reference 5) remain to be fully explored. Thus, even with the k-ε model, further research is needed in the proper implementation of (a) the Magnussen-Hjertager combustion model, (b) the hydrodynamics-chemistry coupling, and (c) more realistic chemical kinetics.

- Finally, the proposed intrusive and nonintrusive diagnostic measurements in the new POSF configuration must carefully examine the flowfield implications of the present predictions to help arrive at the modus operandi of experimental verification and code validation. Although this recommendation is addressed to the experimentalist, it has a significant future impact on the choice of, and refinements in, the several CFD avenues outlined in the earlier recommendations.

REFERENCES

1. W. M. Roquemore, et al., "Utilization of Laser Diagnostics to Evaluate Combustor Models," AGARD Propulsion and Energetics Panel on Combustion Problems in Turbine Engines, CPP-353, Cesme, Turkey, October 1983.

2. L. Krishnamurthy, S. O. Park, D. J. Wahrer, and H. S. Cochran, "Laser Diagnostic Development and Measurement and Modeling of Turbulent Flowfields of Jets and Wakes, Part II: Numerical Predictions of Isothermal Flowfields in a Ducted Centerbody Combustor," AFWAL-TR-83-2044, June 1983.

3. L. Krishnamurthy, M. S. Raju, M. J. Creed, and J. N. Memering, "Time-Averaged and Time-Dependent Computations of Isothermal Flowfields in a Centerbody Combustor," AFWAL-TR-84-2081, December 1984.

4. G. J. Surgess, "Stationary State Computational Fluid Dynamics for Aero-Propulsion Devices," JANNAF Propulsion, Meeting, New Orleans, LA, March 1984.

5. L. M. Chiapetta, "User's Manual for a TEACH Computer Program for the Analysis of Turbulent, Swirling, Reacting Flow in a Research Combustor," NASA Contract NAS3-22771, United Technologies Research Center Report R83-015540-27, September 1983.

6. B. E. Launder and O. B. Spalding, "Mathematical Models of Turbulence," Academic Press, London, 1972.

7. B. F. Magnussen and B. H. Hjertager, "On Mathematical Modelling of Turbulent Combustion with Special Emphasis on Soot Formation and Combustion," Sixteenth Symposium (International) on Combustion, The Combustion Institute, 1978, pp. 719-729.

8. G. D. Raithby, "Skew Upward Differencing for Problems Involving Fluid Flow," Computational Methods in Applied Mechanics and Engineering, Vol. 9, 1976, pp. 153-164.

9. J. M. Beer ad N. A. Chigier,"Combustion Aerodymanics," Applied Science, London, 1972.

10. A. J. Lightman, P. D. Magill, and R. J. Andrews, "Laser Diagnostic Development and Measurement and Modeling of Turbulent Flowfields of Jets and Wakes, Part I: Two-Dimensional Laser Doppler Anemometer Measurements of Isothermal Flowfields in a Ducted Centerbody Combustor," Aero Propulsion Laboratory, Air Force Wright Aeronautical Laboratories, Wright-Patterson Air Force Base, OH, AFWAL-TR-83-2044, June 1983.

11. L. Krishnamurthy, "Isothermal Flowfield Predictions of Confined Coflowing Turbulent Jets in an Axisymmetric Bluff-Body Near Wake," AFWAL-TR-81-2036, May 1981.

12. G. J. Sturgess and S. A. Syed, "Multi-Specie Isothermal Flow Calculations of Widely-Spaced Co-Axial Jets in a Confined Sudden Expansion with the Central Jet Dominant," AIAA-82-1156, 1982.

13. J. N. Memering, "Computational Studies of a Bluff-Body Combustor Flowfield," University of Dayton Honors Thesis, April 1985.

14. R. P Bradley, W. M. Roquemore, J. S. Stutrud, C. M. Reeves, and C. A. Obringer, "Second Data Set for APL Research Combustor," Air Force Wright Aeronautical Laboratories, Aero Propulsion Laboratory, 1982.

15. G. J. Sturgess and S. A. Syed, "Widely Spaced Co-Axial Jet, Diffusion-Flame Combustor: Isothermal Flow Calculations Using the Two-Equation Turbulence Model," AIAA-82-0133, 1982.

16. B. E. Launder, "Turbulence Transport Models for Numerical Computations of Complex Turbulent Flows," Unpublished notes, Manchester University, England, 1976-1977.

17. J. L. Lumley, "Computational Modeling of Turbulent Flows," Advances in Applied Mechanics, Vol. 18, Academic Press Inc., New York, 1978.

18. U. Schumann, "Realizability of Reynolds Stress Turbulence Models," Phys. Fluids 20, 1977, pp. 721-725.

19. A. J. Lightman and P. D. Magill, "Velocity Measurements in Confined Dual Coaxial Jets Behind an Axisymmetric Bluff Body: Isothermal and Combusting Flows," Aero Propulsion Laboratory, Air Force Wright Aeronautical Laboratories, Wright-Patterson Air Force Base, OH, AFWAL-TR-81-2018, 1981.

☆U.S.Government Printing Office: 1986 — 646-067/40912

END

DTIC

10-86